Study of Several Factors Affecting Crew Escape Trajectories From the Space Shuttle Orbiter at Low-Subsonic Speeds

William I. Scallion, Bernard Spencer, Jr.,
George M. Ware, W. Pelham Phillips,
Richard W. Powell, James C. Young,
Garl L. Gentry, Jr., and Zachary T. Applin
Langley Research Center
Hampton, Virginia

Summary

Studies of several factors affecting the bailout characteristics from the Space Shuttle orbiter at low-subsonic speeds were conducted in the Langley 12-Foot Low-Speed Tunnel and the Langley 4- by 7-Meter Tunnel with 0.03-scale models. The escape trajectories of the crew models exiting from the side hatch were most affected by body configuration (standing, seated, or tucked). The tucked, low-drag position produced the highest percentage of successful escape trajectories. Also, the heavier crew models had a higher success rate than the lighter models. In general, the higher exit velocities produced a higher number of successful drops for all crew-model configurations. The 250-lb scaled model was successfully dropped in the seated and tucked positions at full-scale exit velocities equal to or greater than 8 ft/sec, but the lightest model (scaled to 150 lb) was successful only at full-scale exit velocities of 20 ft/sec or greater. With the orbiter model inverted, all crew-model exits from the upper hatch were successful.

Model force tests indicated that high-angle-of-attack trim points existed at an angle of attack of approximately 60°. A simulation of the maneuver to trim to these high angles of attack showed that the maneuver was not feasible. A large-amplitude pitch oscillation persisted until ground contact occurred.

Introduction

The National Aeronautics and Space Administration (NASA) is continuing to refine the flight and operational characteristics of the Space Shuttle. One area currently under study addresses the determination of the proper mode of exit for the crew during a contingency abort situation in which the vehicle can neither attain orbit nor reach a suitable landing site. In this case, the vehicle would glide to lower altitudes of approximately 15 000 to 20 000 ft and decrease velocity to subsonic speeds, and the crew would bail out.

At the request of the NASA Associate Administrator, the Langley Research Center conducted a study to investigate several factors affecting the escape trajectories of crew models for several exit conditions. Exits from the main side hatch were investigated in the wind tunnel for a range of angles of attack and sideslip with the orbiter model upright, and from the upper cabin hatch with the orbiter model inverted. The effects of model weight (scaled values of 150, 200, and 250 lb), model configuration (standing, seated, and tucked), and model exit velocity were studied. The exit trajectories were recorded on high-speed motion-picture film. The motion-picture films were read to determine bailout conditions. Force and moment tests were also conducted to determine the orbiter high-angle-of-attack trim characteristics that might produce a lower vehicle speed for bailout. A computer simulation analysis of the maneuver necessary to fly the orbiter to high angles of attack was performed in support of the wind-tunnel investigation.

To support analytical studies of crew exit trajectories by the Johnson Space Center, an analysis of the drag characteristics of one of the crew-model configurations was conducted. Limited flow-field measurements were also made to determine the exit environment around the model.

The wind-tunnel tests were conducted in the Langley 12-Foot Low-Speed Tunnel and the Langley 4- by 7-Meter Tunnel. A 0.03-scale orbiter model was used, and the tunnel conditions were scaled for full-scale values of 15 000-ft altitude, velocities of 316 to 365 ft/sec depending on vehicle angle of attack, dynamic pressures of 75 to 120 lb/ft², and an angle-of-attack range from 17.5° to 25° at sideslip angles of 0° and 6°. Force tests were made over an angle-of-attack range from −24° to 90° at sideslip angles of 0° and 6°.

A motion-picture film supplement showing selected bailouts under various conditions is available on loan. A request form and a description of the film (L-1291) are found in the back of this report on page 67.

Symbols

The longitudinal data are referred to the stability system of axes, and the lateral-directional data are referred to the body system of axes. The moment center was located at 65 percent of the body length.

C_D	drag coefficient
C_L	lift coefficient
C_l	rolling-moment coefficient
C_{l_β}	$\partial C_l/\partial\beta$, per degree
$C_{l_{\delta_a}}$	$\partial C_l/\partial\delta_a$, per degree
C_m	pitching-moment coefficient
C_n	yawing-moment coefficient
C_{n_β}	$\partial C_n/\partial\beta$, per degree
$C_{n_{\beta,dyn}}$	$C_{n_\beta}\cos\alpha - (I_Z/I_X)(C_{l_\beta}\sin\alpha)$, per degree
C_R	resultant force coefficient
c.g.	center of gravity
D/q	equivalent drag area, Drag/Dynamic pressure, ft²

F	failed
h	altitude, ft
I_X	moment of inertia about longitudinal body axis, slug-ft^2
I_Z	moment of inertia about normal body axis, slug-ft^2
l	reference body length, ft
M	Mach number
P	passed
V	velocity, ft/sec
V_{exit}	crew-model exit velocity, ft/sec
W	weight, lb
X_o, Y_o, Z_o	orbiter body coordinates, in.
x, z	position of scaled crew model referenced to center of side hatch (X_o = 510 in.; Z_o = 367 in.), ft
$\dot{x}, \dot{z}$	velocities of scaled crew model, ft/sec
x_{cg}/l	center-of-gravity location from orbiter nose in terms of reference body length
α	angle of attack, deg
β	angle of sideslip, deg
γ	flight-path angle, deg
δ_a	aileron deflection angle, (Left elevon deflection − Right elevon deflection)/2, deg
δ_{BF}	body-flap deflection angle, positive trailing edge down, deg
δ_e	elevon deflection angle, positive trailing edge down, deg
δ_{SB}	speed-brake deflection angle, deg

Subscripts:

L	local conditions at location surveyed
max	maximum
trim	trim conditions, zero moment
∞	free-stream conditions

Apparatus, Models, and Tests

The tests were conducted in two low-speed tunnels at the Langley Research Center. The initial tests were conducted in the 12-Foot Low-Speed Tunnel to develop the techniques for release of the crew-model figures from the orbiter model. The majority of the investigation was then conducted in the 4- by 7-Meter Tunnel, where drop tests, force tests, and flow-field studies were performed.

The Space Shuttle orbiter model used in the investigation was a Langley-built 0.03-scale orbiter (figs. 1 and 2). All the test parameters were scaled to this model size by the relationships given in reference 1. The scaling parameters are presented below.

$$\text{Scale factor} = \frac{\text{Model length}}{\text{Full-scale length}} = 0.03$$

$$\text{Model area} = (\text{Full-scale area})(\text{Scale factor})^2$$

$$\text{Test velocity} = (\text{Full-scale velocity})(\text{Scale factor})^{1/2}$$

$$\text{Model weight} = \frac{(\text{Tunnel air density})\,(\text{Full-scale weight})}{(\text{Air density at altitude})} \times (\text{Scale factor})^3$$

It was not possible, however, to scale or control all the test parameters and conditions. For example, the Reynolds number of the test, which was much lower than flight values, no doubt had some effect on the boundary layer and flow field around the orbiter. The crew models were inflexible and not dynamically scaled, and because the test was conducted in a horizontal wind tunnel, the gravity vector was misaligned from that of the flight (gliding) condition. In addition, crew-model exit attitude and velocity were difficult to control precisely.

Three body configurations were tested: standing, seated, and tucked (see fig. 3), with three scaled weights for each configuration—150, 200, and 250 lb. The drop-test conditions are given in the table below.

Full-scale velocity, ft/sec	Test velocity, ft/sec	Full-scale crew weight, lb	Crew-model weight, lb
316.0	54.73	150.0	0.00670
345.0	59.76	200.0	.00893
365.0	63.22	250.0	.01116

The drop tests were conducted by setting the tunnel free-stream conditions, positioning the orbiter model at the desired angles of attack and sideslip, and then releasing the models. The orbiter main side hatch was used for most of the test program. As the hatch door was opened, light spring pressure pushed the crew model to the opening where it fell free into the

airstream. Various side-hatch arrangements were investigated to enhance the exit conditions. (See fig. 4.) The first modification was an inclined chute. With this modification, crew-model exit velocity was controlled by releasing the crew model at different heights along the chute. Other modifications consisted of the addition of a deflector to shield the emerging crew model from the stream and hatch extensions of 1 and 2 ft (full-scale). For the model-inverted tests, an existing hatch above the crew cabin was utilized.

During a test, the trajectory of the crew model was recorded by high-speed motion-picture cameras (400 frames per second) positioned around the tunnel test section. The camera locations in the 12-Foot and 4- by 7-Meter Tunnels are shown in figures 5(a) and 5(b), respectively. The 12-Foot Tunnel arrangement consisted of an overhead camera located slightly to the rear and to the left of the model, a side-view camera, and for some tests, a three-quarter rear-view camera below the orbiter model. The arrangement in the 4- by 7-Meter Tunnel had an overhead camera located ahead and to the left of the model and two sideview cameras, one equipped with a wide-angle lens and one with a zoom lens to provide a close-up view of the crew model as it left the orbiter model. The motion-picture film was used to determine the exit velocities for each of the drop tests by measuring the horizontal and vertical positions at the exit from several frames of film by using a known dimension as a reference and the frame speed for timing. Because of the small scale of the models, errors in the measurement of position resulted in relatively large errors in calculated exit velocities when scaled to full-scale values. The film was imprinted with timing marks which enabled the frame rate to be determined accurately. Depending upon the number of frames read, the crew-model velocity, and the particular camera location, the errors in full-scale exit velocities ranged from ±0.9 ft/sec to ±3.2 ft/sec. Generally, the larger errors are associated with the higher exit velocities.

The force tests were conducted in the 4- by 7-Meter Tunnel through an angle-of-attack range of −24° to 90° for elevon deflections of −5° to 15° and sideslip angles of 0° and 6°. The flow-field tests utilized an existing calibrated seven-tube rake (fig. 6). The positions surveyed, in terms of full-scale orbiter stations X_o, Y_o, Z_o, are presented in figure 7.

Results and Discussion

Success-Failure Criteria

A bailout was considered successful when the crew model cleared the orbiter model without contact. When the orbiter was inverted, the crew model was required to clear the vertical tail, the only obstacle in its path.

In normal upright flight attitudes, the crew model could pass over or under the wing. There was no certainty, however, that if the figure passed over the wing it would not contact the fuselage, upper wing surface, orbital maneuvering system (OMS) pod, or vertical tail. Even if the crew model cleared the vehicle after passing over the wing, the low-Reynolds-number flow over the vehicle surfaces above the wing made the results subject to doubt. On the other hand, the free-stream-dominated flow field below the wing should be relatively free from Reynolds number effects except for those on the crew model itself. For this reason, only the exits in which the crew model passed under the wing were considered successful bailouts.

Presented in figure 8 are typical model trajectories from the side hatch of the upright orbiter model that illustrate the success-failure criteria used in this study. Note the difference between the inclination of the flight and wind-tunnel gravity vectors relative to the model. The rearward inclination of the wind-tunnel gravity vector made the drop-test results somewhat conservative.

Exit Test Results

Upper hatch egress. The drop tests conducted by releasing the crew models from the upper hatch with the orbiter model inverted resulted in successful escape trajectories in every case. Crew-model body position and weight had an effect, but all configurations cleared the orbiter easily. A typical escape trajectory from the upper hatch is shown in figure 9. No consideration was given in this study to the problems associated with establishing a stable trimmed flight attitude or the crew reaching the hatch for escape.

Side hatch egress. The results of the tests conducted with the orbiter model upright and the crew models exiting from the main side hatch are presented in table I. No distinction is made in the table between a horizontal exit and an exit from the 50° inclined chute. The results are presented in order of increasing full-scale exit velocity for each crew-model exit configuration. In general, velocities of 12 ft/sec and below are representative of horizontal exits.

A summary of the individual test results of table I is presented in table II. The exit velocities have been categorized into low, medium, and high ranges. The low-exit-velocity range (0 to 12 ft/sec) represents unassisted exits or exits with some small assistance from a device such as an inclined chute mounted in the orbiter cabin and extending from the upper deck to the lower deck hatch. The medium (13 to 19 ft/sec) and high (20 ft/sec and greater) exit-velocity ranges shown would require more positive and complicated acceleration devices.

Generally, within a single exit-velocity range, the

escape trajectories were affected most by body config- uration (standing, seated, or tucked) and to a lesser extent by model weight. These effects are illustrated in figures 10 and 11. As shown in figure 10, the egress of the crew model (scaled to 200 lb) was successful in the tucked position and unsuccessful in the seated position, even though the exit velocity for the seated configura- tion was somewhat higher.

Tests of the seated configuration at two different weights (fig. 11) indicate that the heavier model clears the orbiter by a greater distance than the lighter model, even though the exit velocity of the heavier model was lower. Both models egress successfully, and success rate increases as exit velocity increases regardless of weight or configuration. The use of hatch extensions (fig. 4) had little observable effect on the exit trajectories of the crew models. All models (150 lb, 200 lb, and 250 lb) in a tucked position were dropped successfully at exit velocities equal to or greater than 13 ft/sec. The 250-lb scaled model was successfully dropped in the seated and tucked configurations at exit velocities equal or greater than 8 ft/sec. Tests of the 250-lb scaled model in the standing exit configuration were limited to exit veloc- ities of 16 ft/sec and higher. All tests were success- ful at these velocities. The 200-lb scaled model in the seated configuration was consistently successful at exit velocities equal to or greater than 14 ft/sec, and in the standing configuration, at velocities equal to or greater than 20 ft/sec. An example of the effect of exit velocity on the trajectory of the 200-lb scaled seated configura- tion is shown in figure 12. The 150-lb scaled model was successfully dropped in the seated configuration only at exit velocities greater than 20 ft/sec.

A feasibility study conducted at the Johnson Space Center with a full-scale orbiter mock-up with an exit slide indicated that exit velocities from the orbiter of 6 to 8 ft/sec were possible. Therefore, the low-velocity results are the most applicable to full-scale conditions. Of the total of 100 drop tests, only 35 were in the low-exit-velocity range. The number of samples taken in this group is not sufficient to determine statistical probabilities, but some insight was gained as to the overall trends of the data. Generally, as shown in table II, the escape trajectories were affected somewhat by weight, but they were primarily affected by body configuration (standing, seated, or tucked). Based on the small sample of data available, the tucked, low- drag configuration offers the highest probability of a successful escape trajectory.

Drag Estimation

An analysis was conducted to determine the drag characteristics of a scaled 250-lb crew model in the tucked configuration. The drag values were to be used in an analytical simulation of exit trajectories at the

Johnson Space Center to validate the computer code by comparing the output with the wind-tunnel results. This configuration was chosen because as previously discussed, it was the most promising configuration for a successful exit. The horizontal and vertical components of the model escape trajectory were read from the film as a function of time. A set of curve-fit equations, each covering 0.04-sec overlapping segments of the trajectory, were developed and differentiated for velocities and accelerations. The x- and z-positions as read from the film are shown in figure 13(a). These positions were corrected for parallax effects induced by a small velocity in the y-direction (toward the camera). No y-axis accelerations were calculated, as they were considered to be negligible. The resulting x- and z-velocities are shown in figure 13(b). The oscillatory nature of these parameters was found to be the result of crew-model rotation. Observations of the model from the film indicated oscillations about one or more axes. The calculated accelerations were used to determine the lift and drag coefficients, and these were resolved into a total resultant coefficient, C_R (fig. 13(c)). These stability axis coefficients are given without regard to the body attitude relative to the wind. The average drag coefficient for this case was 0.620, the average lift coefficient was 0.232, and the average resultant coefficient was 0.662. The equivalent full-scale crew- body drag area, D/q, is presented as a function of time in figure 13(d). These values are in good agreement with the values for a similar configuration taken from reference 2. The values of D/q obtained herein range from 1.26 to 3.02 ft^2, as compared with values of 2 to 3 ft^2 from reference 2. The wider range of values from this investigation results from the wide range of attitudes of the crew models relative to the stream. Only two attitudes were presented in reference 2.

Force-Test Results

In an attempt to define the low-speed aerodynam- ics of the orbiter at very high angles of attack, force and moment tests were performed at angles of attack from $-24°$ to $90°$. These tests were conducted to de- fine the trim characteristics of the orbiter when inverted (negative angles of attack) and to identify the existence of stable longitudinal-trim points at large angles of at- tack, which could provide lower flight speeds for bailout. The Reynolds number of these tests was low, about 1.2 $\times$ 10^6; however, the test results do indicate expected trends in longitudinal characteristics. The longitudi- nal aerodynamic characteristics from these tests in the 4- by 7-Meter Tunnel are presented in figure 14. The plot of C_m versus α in figure 14(c) indicates the occur- rence of stable trimmed pitching moments at angles of attack near $60°$ for an orbiter center-of-gravity location at 65 percent of the fuselage reference length. Figure 15

4

shows a summarization of elevon and aileron control characteristics and the directional-stability parameter derived from the high-angle-of-attack force tests. The upper portion of the figure summarizes the effect of orbiter center-of-gravity travel on the longitudinal-trim capability of the elevons. The design flight centers of gravity for the orbiter during entry vary from a forward c.g. location of $0.65l$ to a rearward location of $0.675l$. For the most forward c.g., the orbiter has trim capability up to an angle of attack of about 68°. The aft c.g. condition, however, requires pitching moments for trim which exceed the maximum static-trim capability of the elevon (at $\delta_{e,\max} = 20°$) for angles of attack between 35° and 77°. The center plot of figure 15 shows that the variation of the directional-stability parameter, $C_{n_{\beta_{dyn}}}$, is positive (stable) over the angle-of-attack range. The lower portion of figure 15 shows aileron effectiveness, $C_{l_{\delta_a}}$, over the angle-of-attack range. The aileron effectiveness declines sharply at angles of attack above 20° until a control reversal is produced at $\alpha = 30°$. Above 50° the ailerons become ineffective.

Simulation Results

Since the static-force tests had shown the existence of a high-angle-of-attack trim point, a simulation analysis was used to determine if the Shuttle control system, as designed, would allow a pilot to perform a maneuver to reach this condition. The Reentry Flight Dynamics Simulator (RFDS), reference 3, which had been developed to aid in the certification of the guidance and control algorithms for the Shuttle entry, was selected for this study. The simulator allows six-degree-of-freedom analyses; but for this preliminary study, only the longitudinal (pitch) plane dynamics were examined. The aerodynamic characteristics generated in the current study were used in this simulation. Since no damping values were available for these high angles of attack, C_{m_q} (pitch damping due to pitch rate) was set to the value at the highest angle of attack (20°) at $M = 0.25$ available from the Space Shuttle Aerodynamic Design Data Book (ref. 4).

The results of the simulation are presented in figure 16 for the orbiter with center-of-gravity positions of $0.650l$ and $0.675l$. The maneuver was initiated at an altitude of approximately 20 000 ft at a speed of 640 ft/sec. The simulation indicated that the flight time from that altitude while performing this maneuver was a little over 2 minutes with the resultant velocity dropping and becoming relatively constant between 250 and 200 ft/sec. The major concern disclosed by the simulation is presented in figure 16(a), where the variation of the vehicle angle of attack as a function of time is shown. The orbiter rotated to the high angles, passed beyond the trim point, and then oscillated about the trim condition. The large-amplitude oscillations are convergent

but persist until ground impact. (Independent studies at the Johnson Space Center also confirmed these findings.) Even though the elevator is driven between its upper and lower limits (fig. 16(c)), it is unable to damp the angle-of-attack oscillations. The simulation, therefore, indicates that although there is a stable trim at high angles of attack and the airspeed is greatly reduced, the dynamics of the maneuver make it impossible for the crew to exit from the vehicle unassisted.

Flow-Field Surveys

Some preliminary flow-field surveys were conducted to support the exit trajectory simulations conducted at the Johnson Space Center. More detailed flow-field measurements were subsequently made at the Texas A. & M. University wind tunnel with the orbiter model of the present tests. The flow-field surveys reported herein measured the ratio of local flow velocity V_L to free-stream velocity V_∞ at discrete X_o, Y_o, Z_o locations and the local angles of attack α_L and local sideslip angles β_L at these same locations.

The results of the flow-field surveys are presented in figures 17 to 25. Velocity ratio (V_L/V_∞) and local angles of attack (α_L) and sideslip (β_L) are presented as functions of longitudinal and spanwise locations $(X_o$ and Y_o, respectively) for several vertical positions. These positions are illustrated in figure 7. The most important positions surveyed were those near the main side hatch where the exiting crew would first encounter the external flow field. The nearest position to the hatch surveyed was at $X_o = 510$ in., $Z_o = 367$ in., $Y_o = 125$ in., a position about 24 in. from the hatch in the Y-direction and nearly centered on the hatch opening in the X-Z plane. This position is represented by the circular symbol in figures 17, 18, and 19. As can be seen in figures 17(a) and 17(b), 18(a) and 18(b), and 19(a) and 19(b), the ratio of local velocity to free-stream velocity ranges from 1.05 to 1.14, depending upon the range of angle of attack and free-stream test velocity. This suggests that the flow around the orbiter forebody is sensitive to Reynolds number, and for this reason, the values of the flow-field parameters presented herein may not represent the full-scale flight values. Generally, this ratio tended to increase with increasing angle of attack. The velocity ratio decreased for positions further outboard from the hatch in the Y-direction and tended to increase in the longitudinal (downstream) direction. The increase in the velocity ratio in the longitudinal direction, especially for the inboard locations, would be expected, since the survey X-Y plane is near the wing upper surface where the local flow is accelerating. This tends to substantiate the tendency of the standing and seated crew-model configuration (high-drag-area models) to pass over the wing. The local angles of attack and sideslip near the hatch were positive (figs. 17(c) and

17(d), 18(c) and 18(d), and 19(c) and 19(d)). These local wind directions would produce forces tending to push the crew models upward and outboard relative to the fuselage. At $Y_o = 193$ in., the angles of attack and sideslip of the local wind varied widely in the longitudinal direction, and the sideslip angle reversed direction twice between $X_o = 510$ in. and $X_c = 1110$ in. These variations increase in magnitude as angle of attack is increased from 17.5° (figs. 17(c) and 17(d)) to 25° (figs. 19(c) and 19(d)). This indicates the probable existence of vortex flow over the wing in the inboard region.

At positions below the side hatch, the velocity ratio at the inboard station, $Y_o = 125$ in., was less than 1.0 and tended to decrease in the aft longitudinal direction (fig. 23(a)). The angles of attack and sideslip for these lower positions (figs. 23(b), 23(c), and 23(d)) showed wide variations for the inboard positions $Y_o = 125$ in. and $Y_o = 193$ in.; however, they do not exhibit the reversal in sideslip angle shown in figures 17, 18, and 19 for the position above the wing. These local conditions would tend to push a crew model downward and away from the fuselage at the inboard station under the hatch; and further outboard, the effect of the upwash ahead of the wing ($Y_o = 193$ in.) would be felt, but to a much lesser degree than at $Z_o = 367$ in.

Summary of Results

Some wind-tunnel and analytical studies of several factors affecting the crew escape trajectories during bailout from the Space Shuttle orbiter at low-subsonic speeds have been conducted. In general, the results of the investigation indicated that at angles of attack of 17.5° to 25°, successful egress could be made from the orbiter main hatch if the crew model had sufficient exit velocity; the higher exit velocities increased the probability of successful egress. Within a single full-scale exit-velocity range (Low = 0 to 12 ft/sec, Medium = 13 to 19 ft/sec, High = 20 ft/sec or greater), the escape trajectories of the crew models were most affected by body configuration. The tucked (low-drag) position produced the highest percentage of successful escape trajectories. The heavier crew models in any body configuration had a higher success rate or cleared the orbiter by a greater distance than the lighter models. The model with a scaled weight of 250 lb was successfully dropped in the seated and tucked positions at exit velocities equal to or greater than 8 ft/sec, whereas the lightest model (150-lb scaled weight) was only successful at exit velocities of 20 ft/sec or greater. When the orbiter model was rolled into an inverted flight attitude, all crew models made successful exits from the upper cabin hatch.

Model force tests indicated that the vehicle had a stable high-angle-of-attack trim point at approximately 60°, which could provide improved bailout conditions at reduced airspeeds. A computer simulation of the maneuver necessary to fly the orbiter to the high trim angle showed, however, that the flight characteristics were unsatisfactory because large-amplitude pitch oscillations occurred until ground contact.

References

1. Gainer, Thomas G.; and Hoffman, Sherwood: *Summary of Transformation Equations and Equations of Motion Used in Free-Flight and Wind-Tunnel Data Reduction and Analysis.* NASA SP-3070, 1972.

2. Hoerner, Sighard F.: *Fluid-Dynamic Drag.* Hoerner Fluid Dynamics (Brick Town, N.J.), c.1965.

3. Kaylor, Jack T.; Rowell, Lawrence F.; and Powell, Richard W.: *A Real-Time Digital Computer Program for the Simulation of Automatic Spacecraft Reentries.* NASA TM X-3496, 1977.

4. *Aerodynamic Design Data Book. Volume 1: Orbiter Vehicle.* NASA CR-160386, 1978.

6

TABLE I. RESULTS FROM DROP TESTS REPRESENTING EXITS FROM MAIN SIDE HATCH WITH ORBITER MODEL UPRIGHT

(a) Results for model representing 150-lb weight

Crew-model exit configuration	Full-scale exit velocity, ft/sec	α, deg	β, deg	Exit extension (full-scale), ft	Result
Standing	12.3	20.0	0	None	F
	12.8	25.0			F
	18.4	20.0			F
	18.9	17.5			F
	19.1	20.0			P
	20.1	17.5	6		P
	20.2	25.0	0		F
	20.4	20.0			F
	20.8	20.0			F
	21.0	25.0			F
	21.3	17.5			F
	21.8	25.0			F
	25.1	20.0			P
	26.4	25.0			F
	28.0	17.5			F
Seated	10.4	25.0	0	None	F
	11.4	20.0			P
	14.3	25.0			F
	14.5	20.0			F
	14.6	20.0			F
	14.8	17.5			F
	17.0	25.0			F
	17.6	17.5	6		P
	17.7	25.0	0		F
	18.7	17.5			P
	18.9	25.0			F
	22.4	25.0			P
	25.4	20.0			P
Tucked	7.3	25.0	0	2	F
	8.3	20.0		None	P
	11.2	25.0		1	F
	13.3	20.0		2	P
	14.6	20.0		1	P
	15.3	25.0		None	P
	15.6	20.0			P
	17.3	17.5			P
	19.2	17.5			P
	22.7	17.5	6		P
	23.1	20.0	0		P

TABLE I. Continued

(b) Results for model representing 200-lb weight

Crew-model exit configuration	Full-scale exit velocity, ft/sec	α, deg	β, deg	Exit extension (full-scale), ft	Result
Standing	20.6	20.0	0	None	P
	28.1	17.5	0	None	P
Seated	1.0	25.0	0	2	F
	2.0	16.0	2	None	F
	4.1	25.0	0	None	F
	5.6	16.0	6	None	F
	5.8	20.0	0	1	F
	6.0	16.0	0	None	F
	7.0	16.0	0		F
	7.5	16.0	6		F
	7.8	20.0	0		F
	8.3	20.0	0		F
	8.3	20.0	2	2	P
	10.6	16.0	0	None	P
	11.3	20.0	0	None	P
	13.7	16.0	2	None	F
	14.6	25.0	0	1	P
	16.3	20.0	0	None	P
	23.3	17.5	0	None	P
	28.1	16.0	4	None	P
Tucked	5.0	25.0	0	2	P
	6.0	20.0		None	P
	7.3	25.0		None	P
	7.3	20.0		1	P
	10.9	20.0		2	P
	17.5	17.5		None	P
	20.0	20.0		None	P
	20.5	25.0		1	P

8

TABLE I. Concluded

(c) Results for model representing 250-lb weight

Crew-model exit configuration	Full-scale exit velocity, ft/sec	α, deg	β, deg	Exit extension (full-scale), ft	Result
Standing	16.2	25.0	0	None	P
	16.7	20.0	0	↓	P
	18.6	17.5	0		P
	20.0	17.5	6		P
	20.8	20.0	0	↓	P
	24.9	17.5	0		P
Seated	5.4	25.0	0	2	P
	6.6	25.0		2	P
	7.3	20.0		None	P
	7.3	25.0		None	P
	8.2	25.0		1	F
	9.7	20.0		None	P
	11.3	20.0		None	P
	12.1	17.5		None	P
	12.3	20.0		1	P
	16.2	20.0		None	P
	16.8	17.5	↓	↓	P
	19.7	17.5	6		P
	25.4	17.5	0	↓	P
	26.7	25.0	0		P
Tucked	7.8	20.0	0	None	P
	10.9	20.0		2	P
	12.3	25.0		2	P
	13.0	25.0		None	P
	13.5	↓		1	P
	14.7			None	P
	17.5	↓		1	P
	17.8	20.0		None	P
	18.2	17.5		↓	P
	18.3	17.5			P
	20.0	20.0			P
	21.1	20.0	↓		P
	21.7	17.5	6	↓	P

TABLE II. SUMMARY OF SIDE-HATCH DROP-TEST RESULTS

Exit velocity, ft/sec	Number of drops					
	W = 150 lb		W = 200 lb		W = 250 lb	
	P	F	P	F	P	F
Standing						
Low (0 to 12)	0	1				
Medium (13 to 19)	1	3			3	0
High (≥ 20)	2	8	2	0	3	0
Seated						
Low	1	1	3	10	8	1
Medium	2	7	2	1	2	0
High	2	0	2	0	3	0
Tucked						
Low	1	2	5	0	3	0
Medium	6	0	1	0	7	0
High	2	0	2	0	3	0

Crew-model configuration	Number of drops			
	W = 150 lb	W = 200 lb	W = 250 lb	Total, all weights
Standing	15	2	6	23
Seated	13	18	14	45
Tucked	11	8	13	32
Total, all configurations	39	28	33	100

L-82-9906

Main Side Hatch

United States

NASA
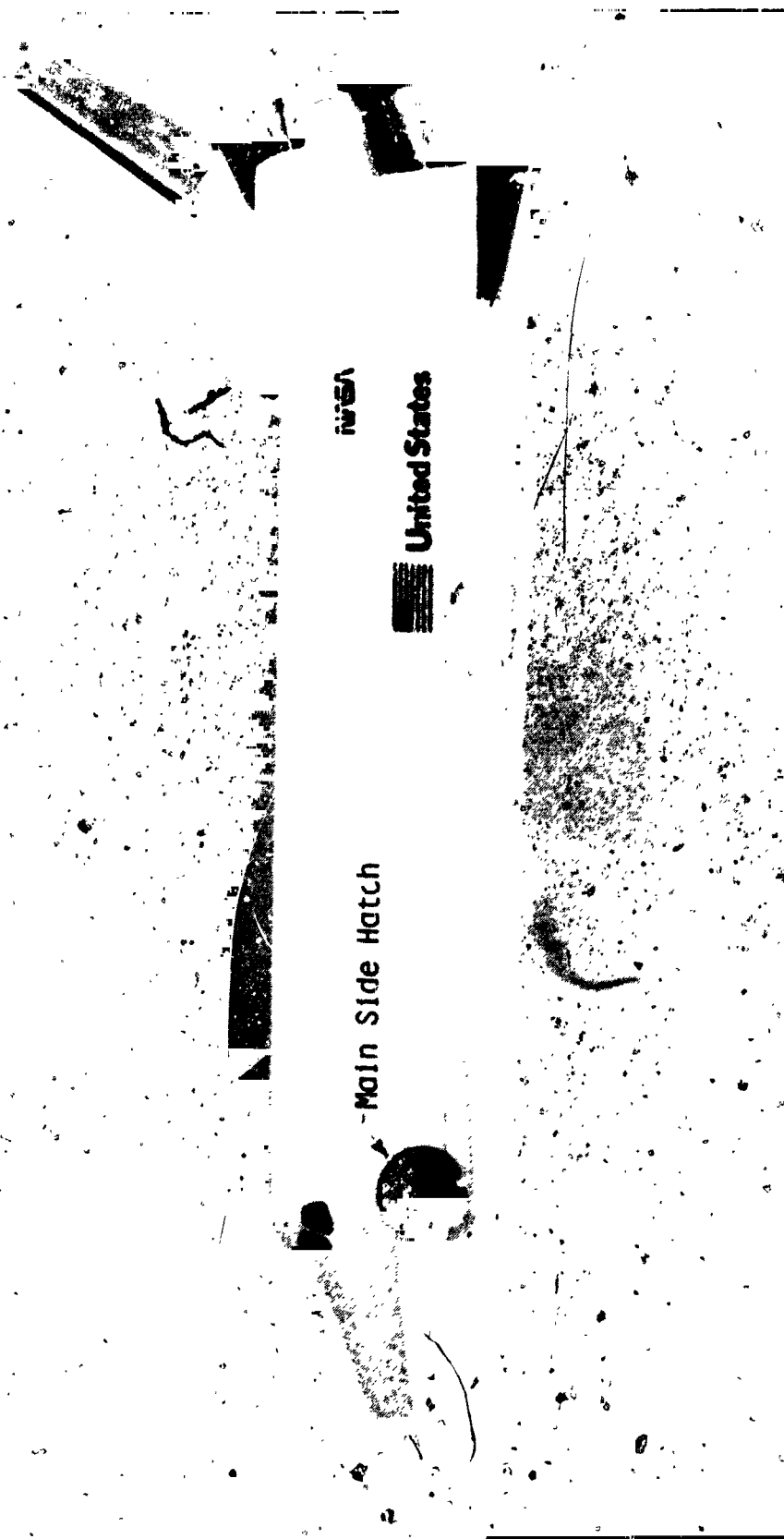
Figure 1. Photograph of 0.03-scale orbiter model used in drop tests.
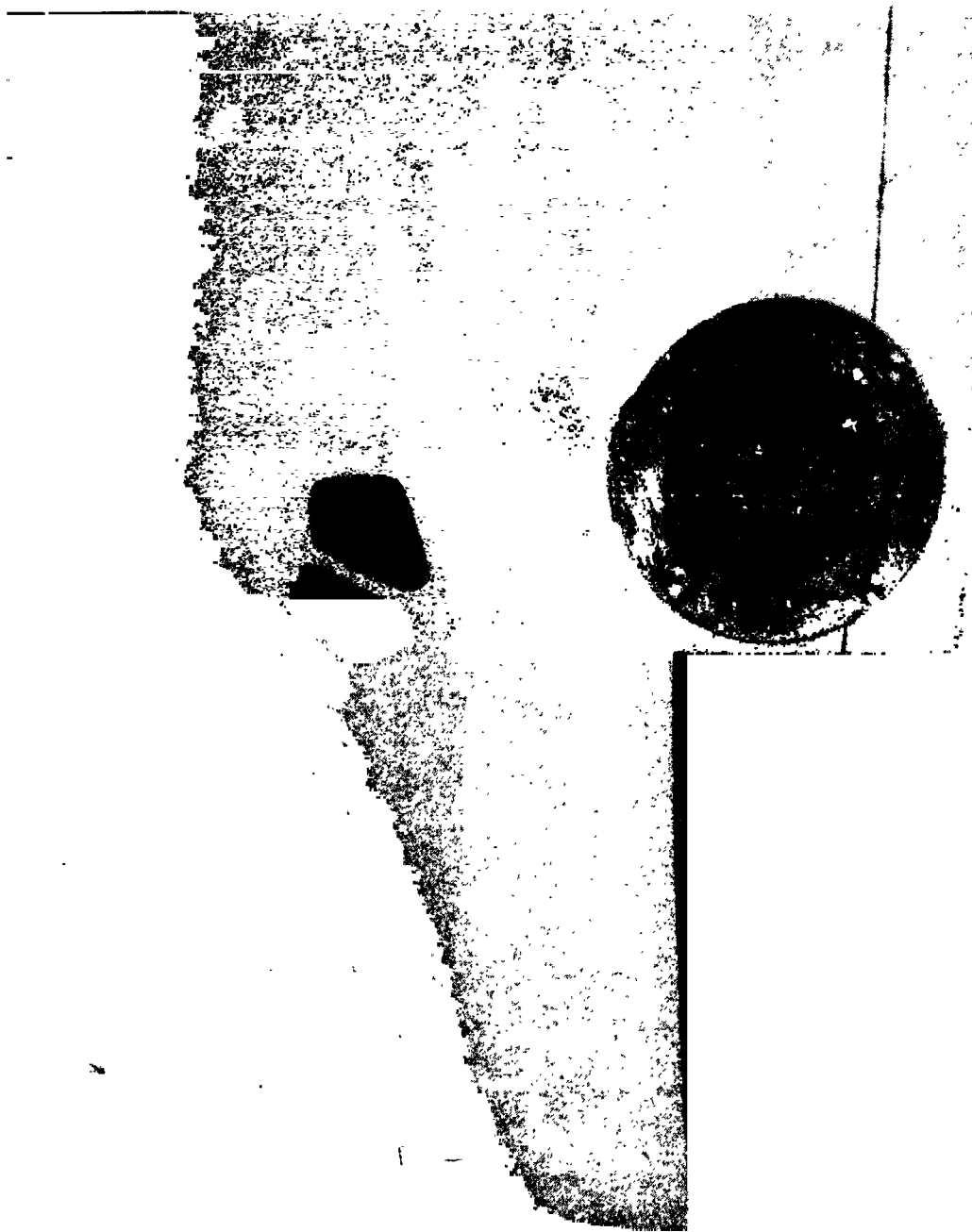
L-82-9910

Figure 2. Photograph of orbiter model with main hatch configured for 90° side exit tests.

L-83-2570

Figure 3. Crew-model configurations used in tests. Coin shown for size comparison.

Figure 4. Geometry of exit hatch on orbiter model. Dimensions are full-scale.

Inclined Chute

Deflector

Exit Hatch Extensions

Horizontal

Inclined

1 ft

2 ft

1 ft

2 ft

4 ft

2 ft

50°

$X_0 = 235$ in.

$Z_0 = 367$ in.

510 in.

14

TOP VIEW

3/4 rear camera

8.4

Side camera

6.4

8.0

FRONT VIEW

Top camera

1.4

8.0

2.0

SIDE VIEW

9.4

6.0
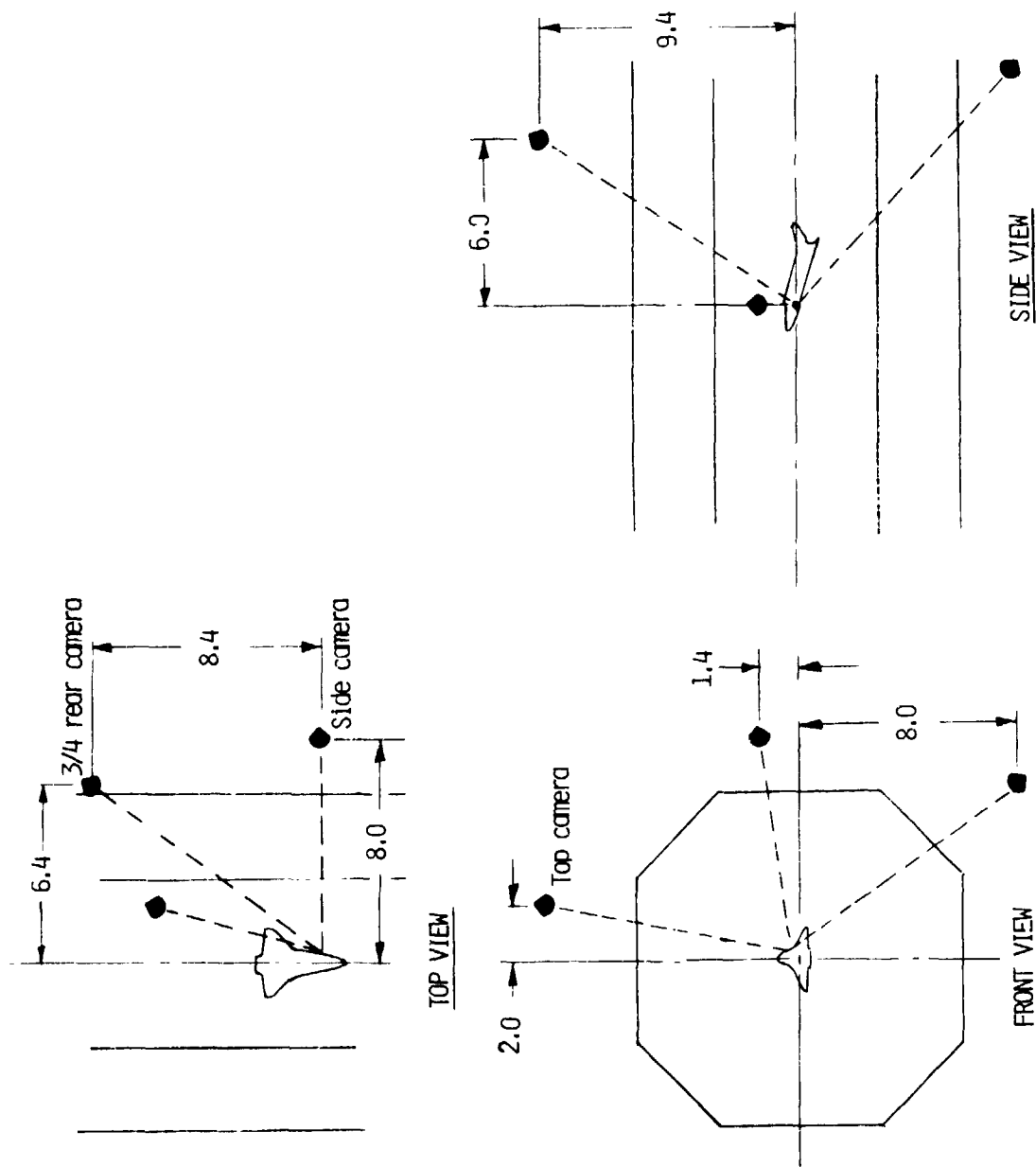
(a) 12-Foot Low-Speed Tunnel.

Figure 5. Camera arrangements used in drop tests. All dimensions (approximate) are in feet.

15

Side cameras (Wide angle and zoom)

Top camera ■

Tunnel boundary

9.4

SIDE VIEW

1.0

7.5

12.0

TOP VIEW

FRONT VIEW

1.0

1.0
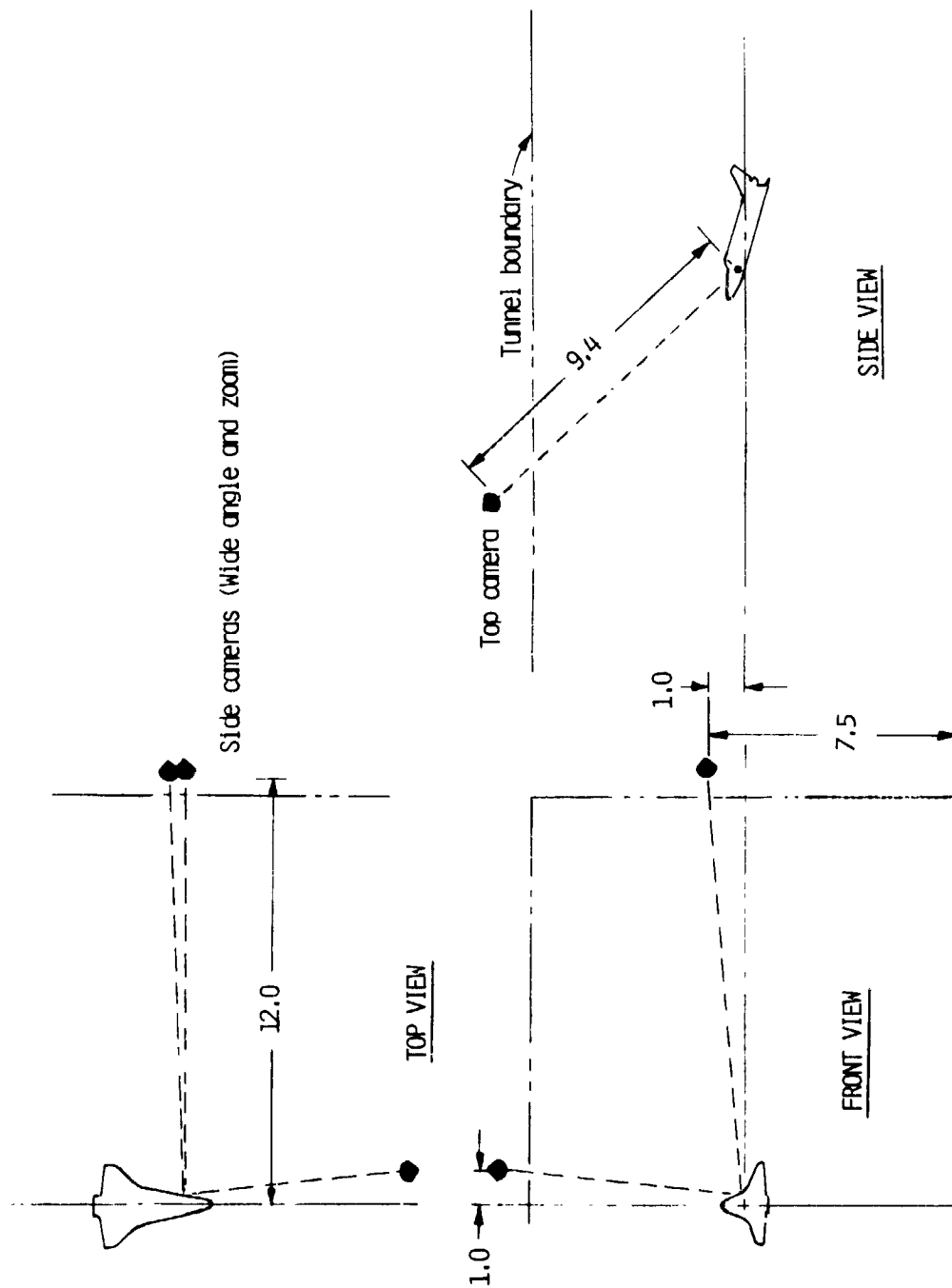
(b) 4- by 7-Meter Tunnel.

Figure 5. Concluded.
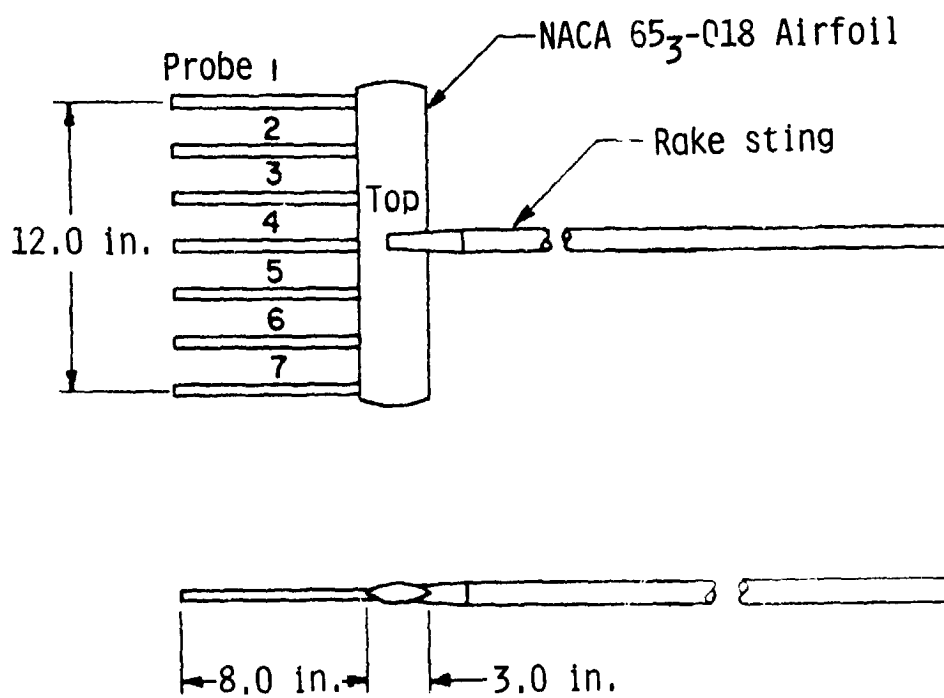
Figure 6. Survey rake used in 4- by 7-Meter Tunnel tests.
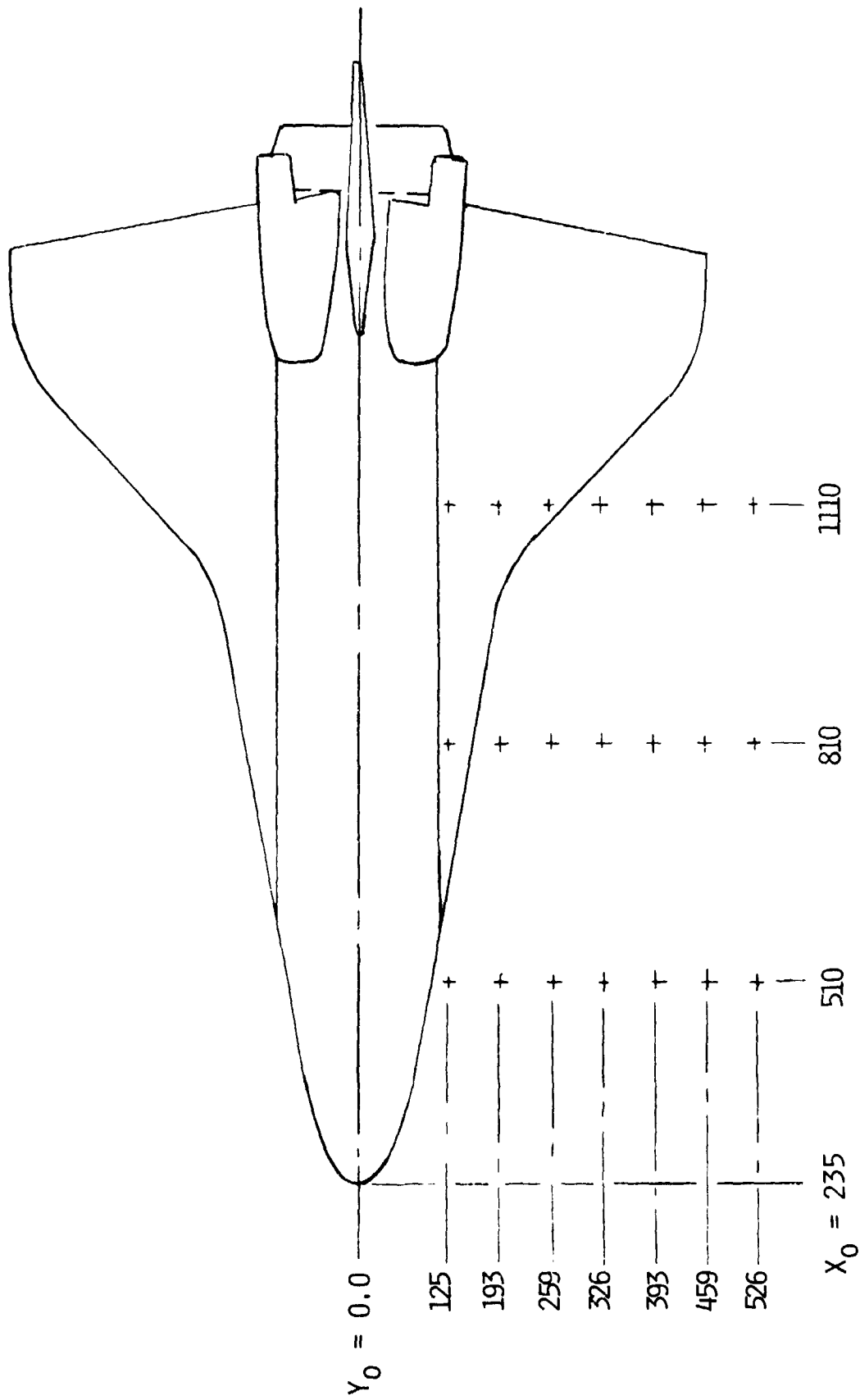
(a) Plan view.

Figure 7. Survey rake positions in 4- by 7-Meter Tunnel. Dimensions are in inches.
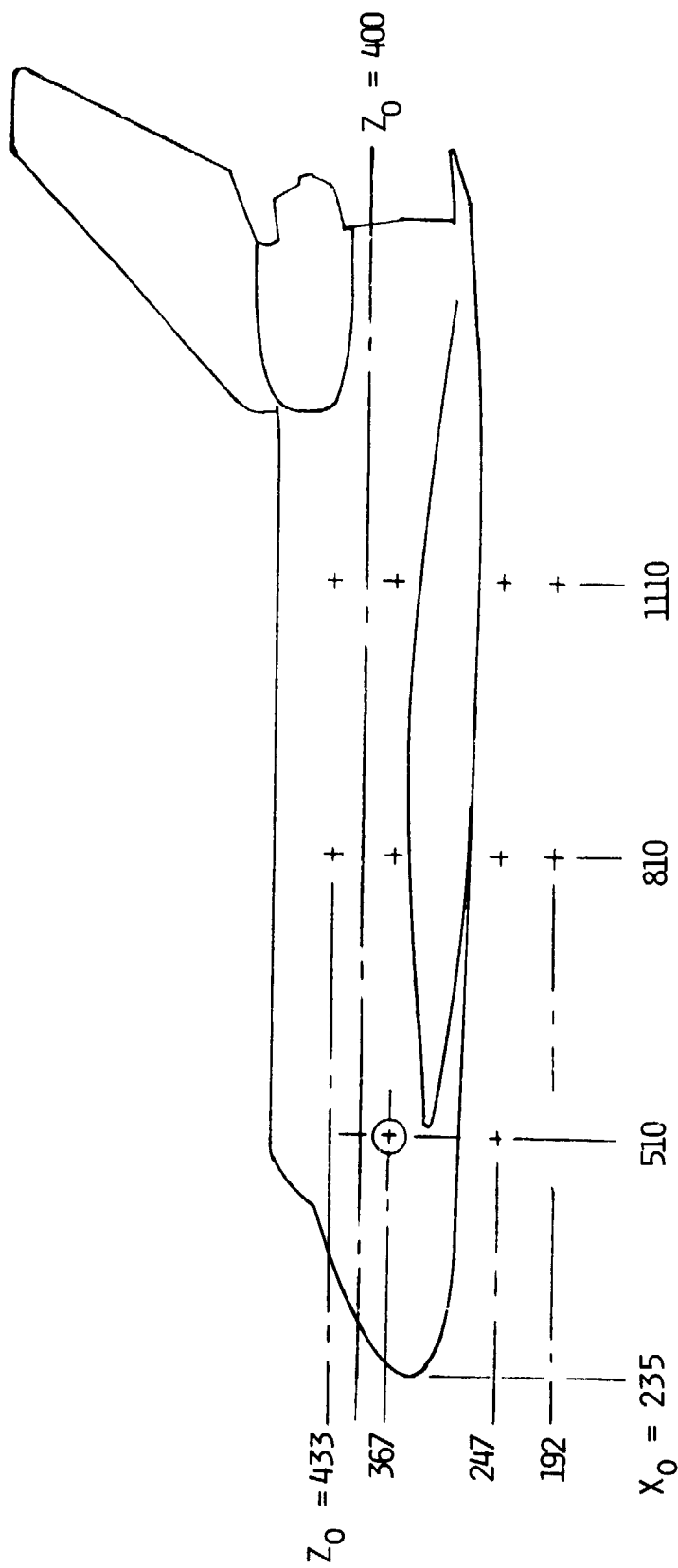
(b) Side view.

Figure 7. Concluded.
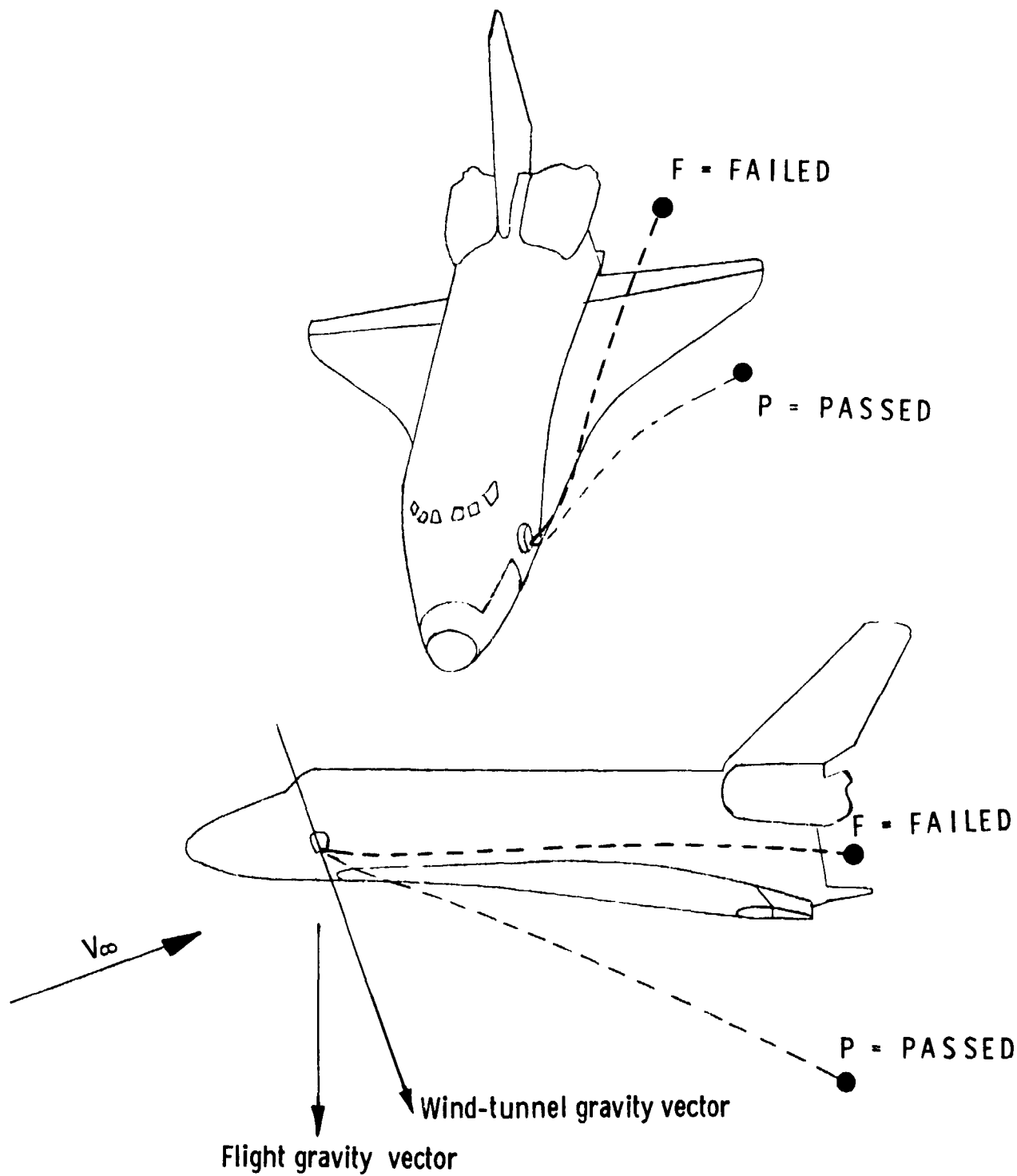
Figure 8. Pass-fail examples for typical escape trajectories from main side hatch of orbiter model.
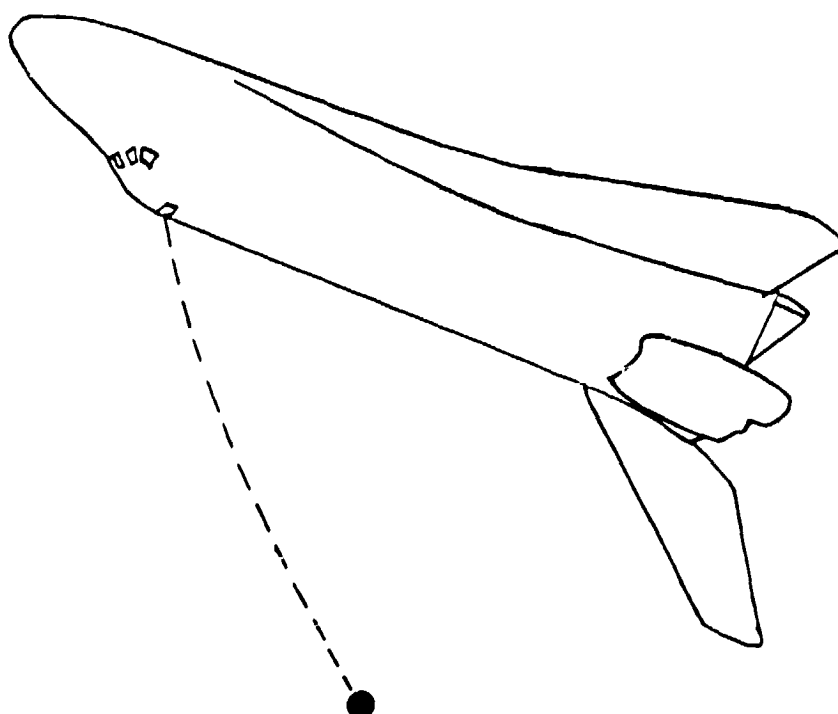
Figure 9. Typical escape trajectory from upper hatch with orbiter model inverted.
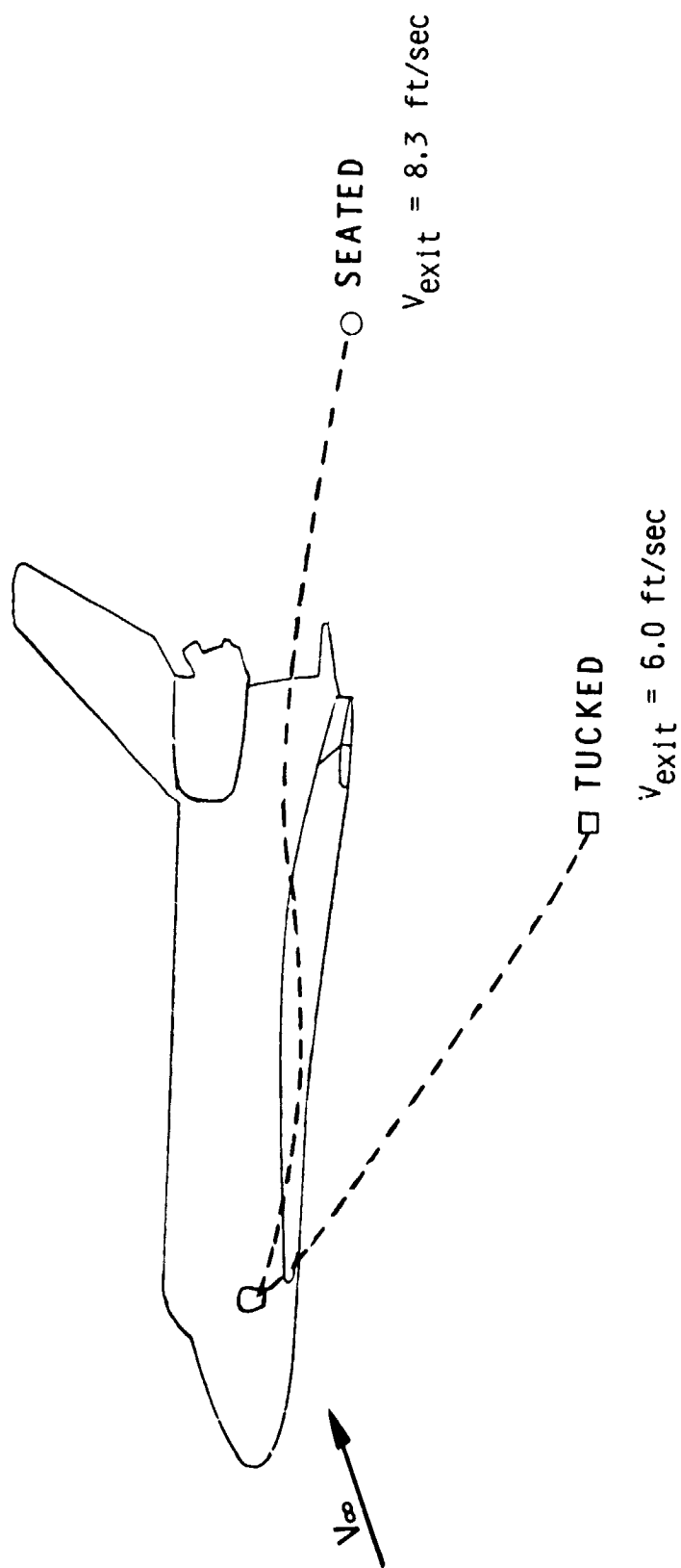
Figure 10. Effect of crew configuration on escape trajectory from side hatch. Scaled weight = 200 lb; $\alpha = 20°$.
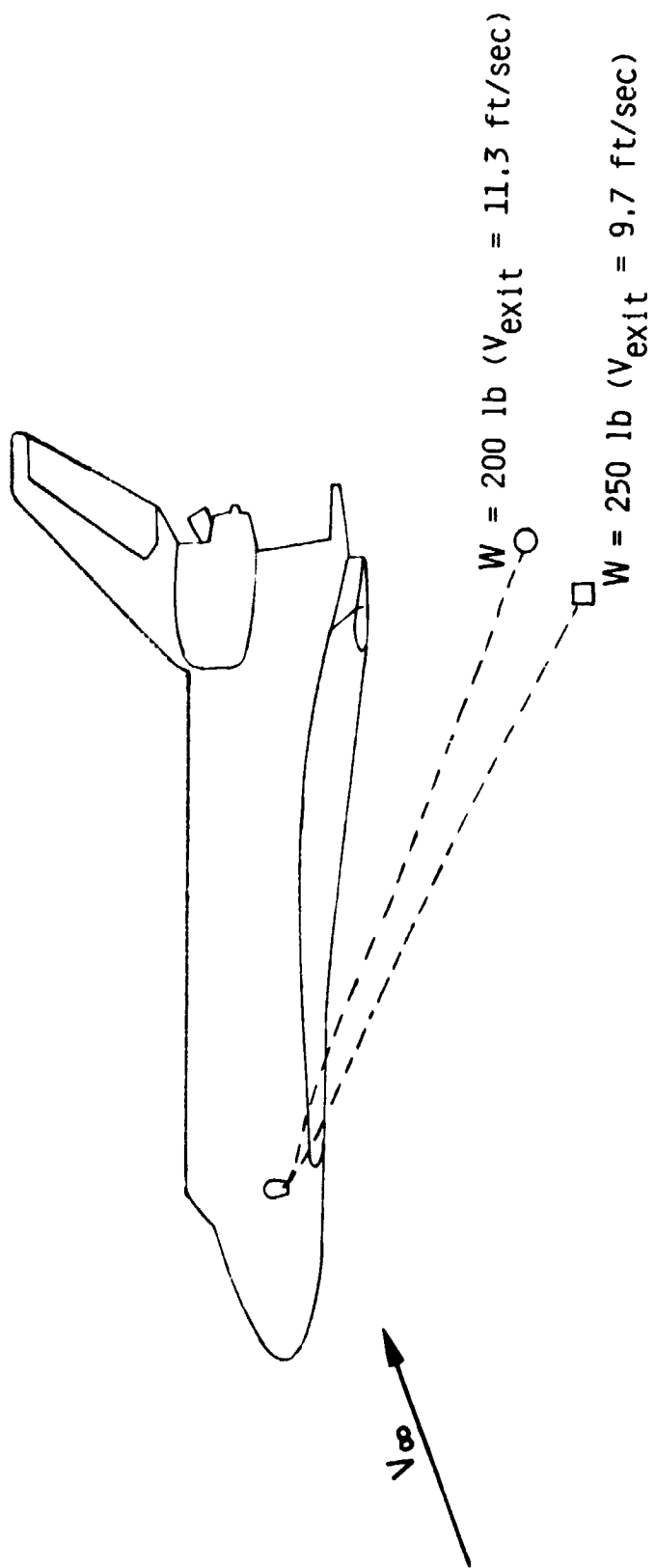
Figure 11. Effect of crew weight on escape trajectory of seated crew model from side hatch. $\alpha = 20°$.

W = 200 lb (V_{exit} = 11.3 ft/sec)

W = 250 lb (V_{exit} = 9.7 ft/sec)
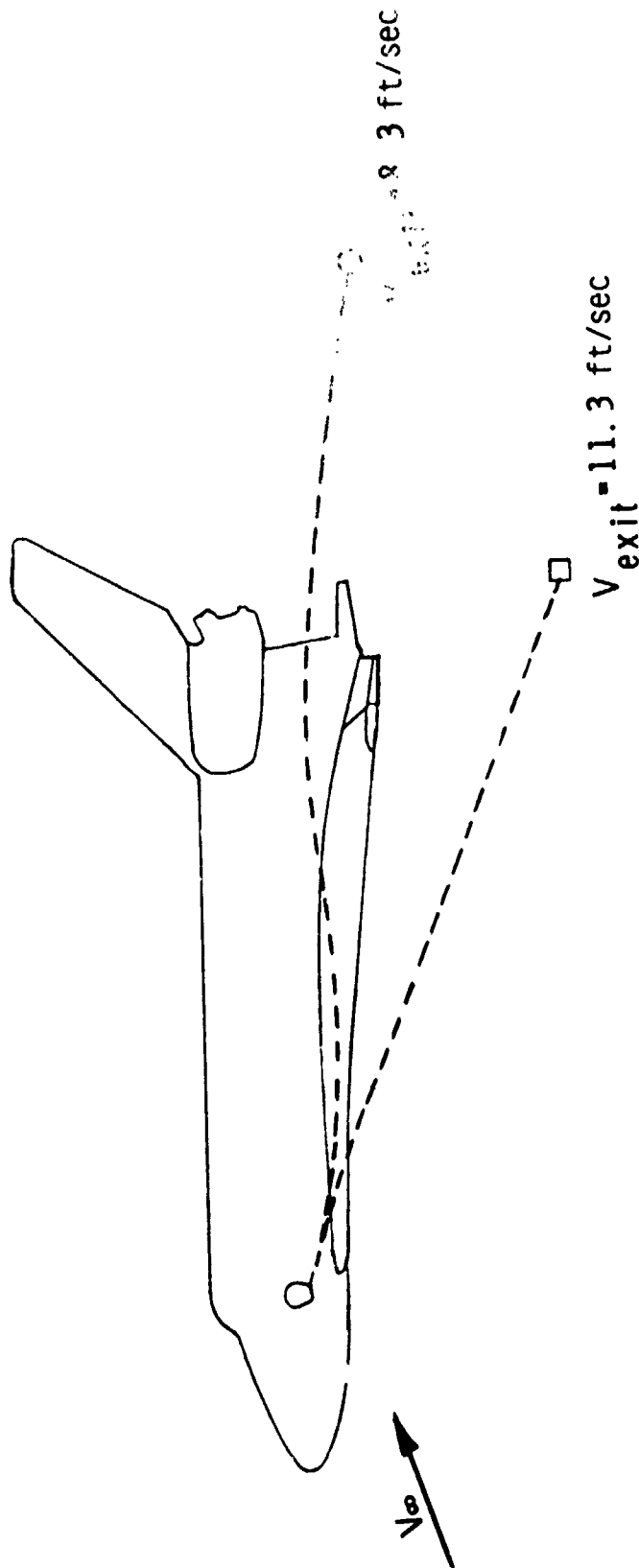
Figure 12. Effect of exit velocity on escape trajectory of scaled 200-lb seated crew model. Side hatch; $\alpha = 20°$.
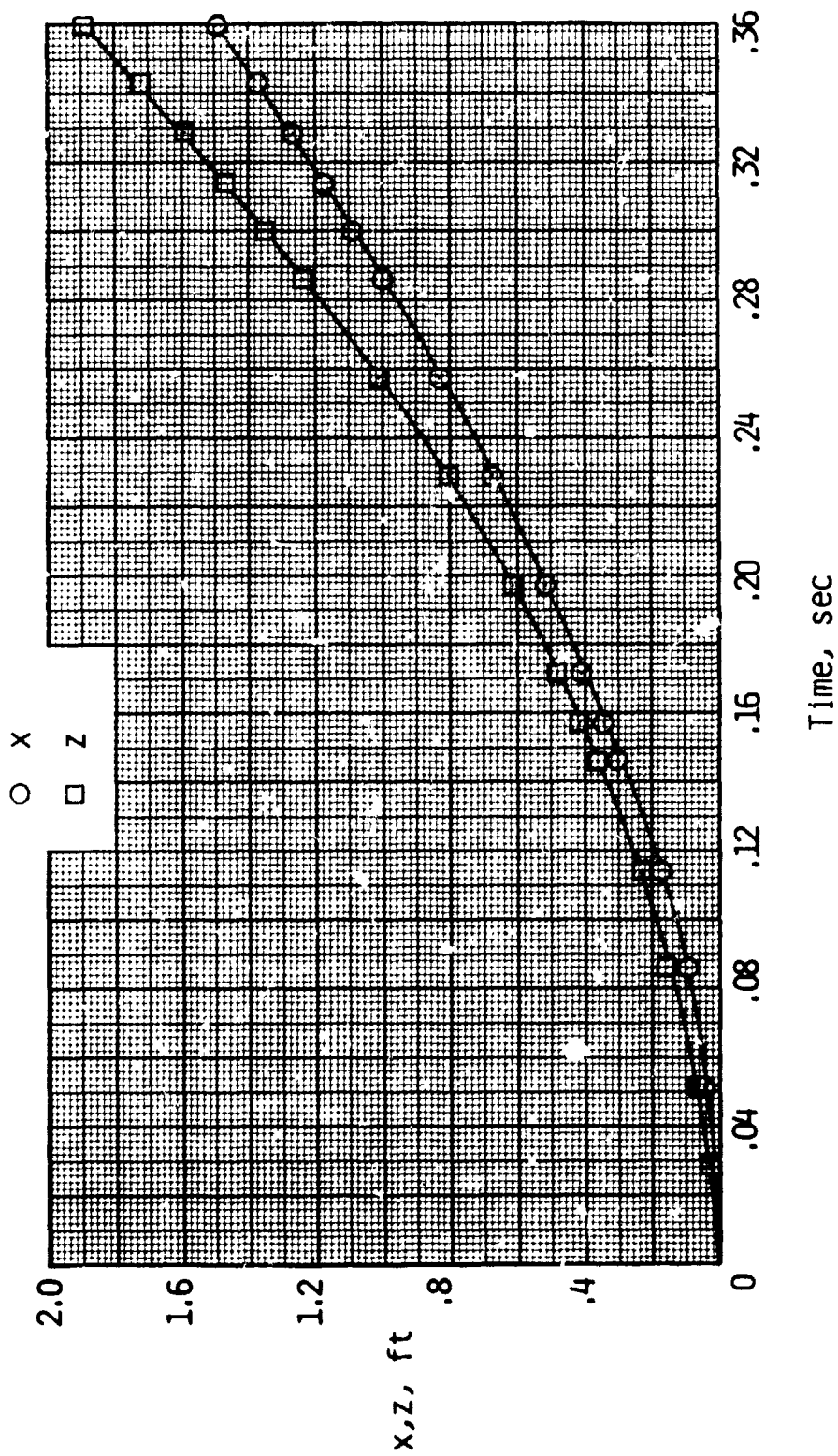
(a) Variation of x- and z-positions with time.

Figure 13. Results of analysis of drag characteristics of scaled 250-lb tucked configuration. $\alpha = 20°; V_o = 59.78$ ft/sec.
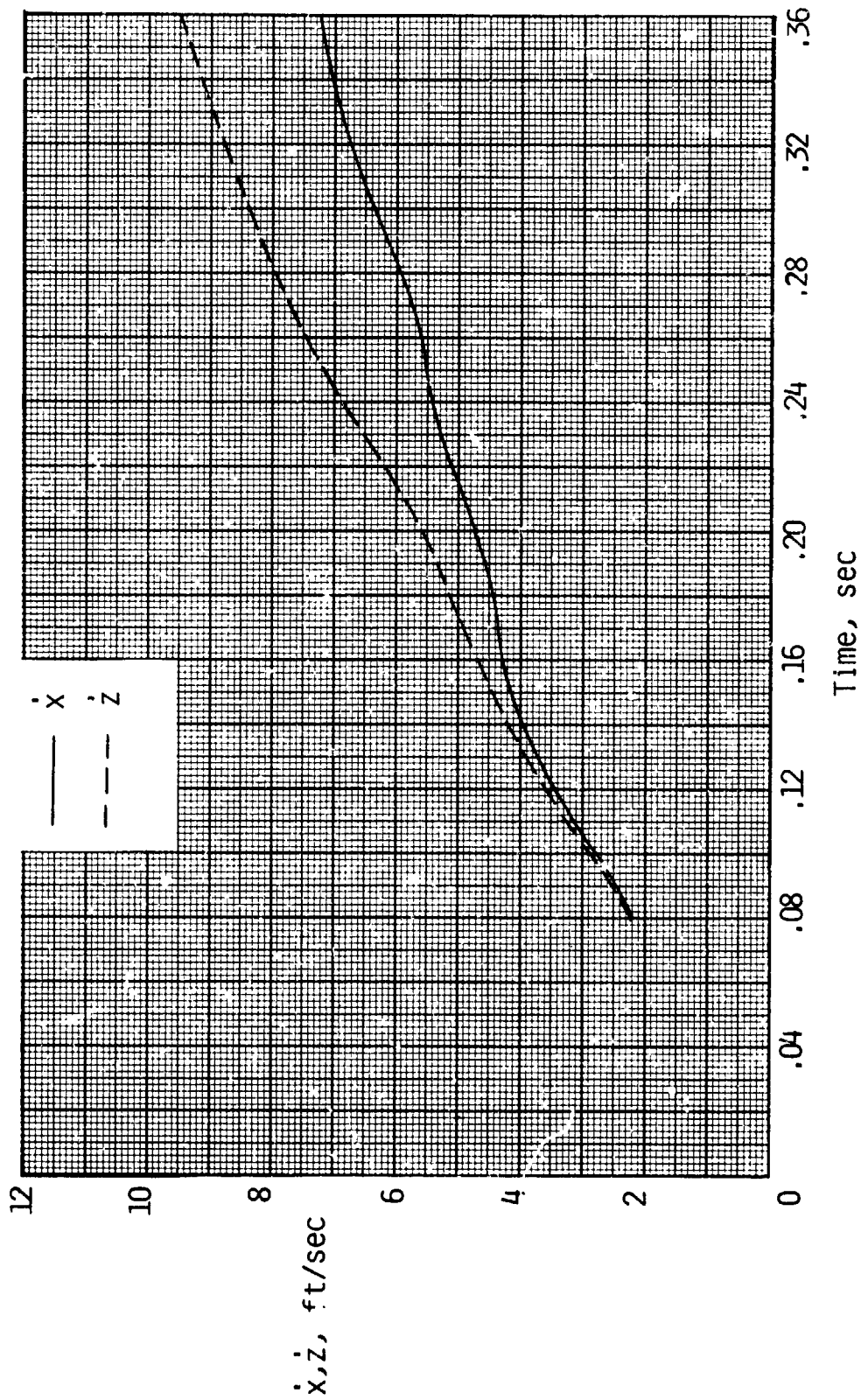
(b) Variation of calculated x- and z-velocities with time.

Figure 13 Continued.
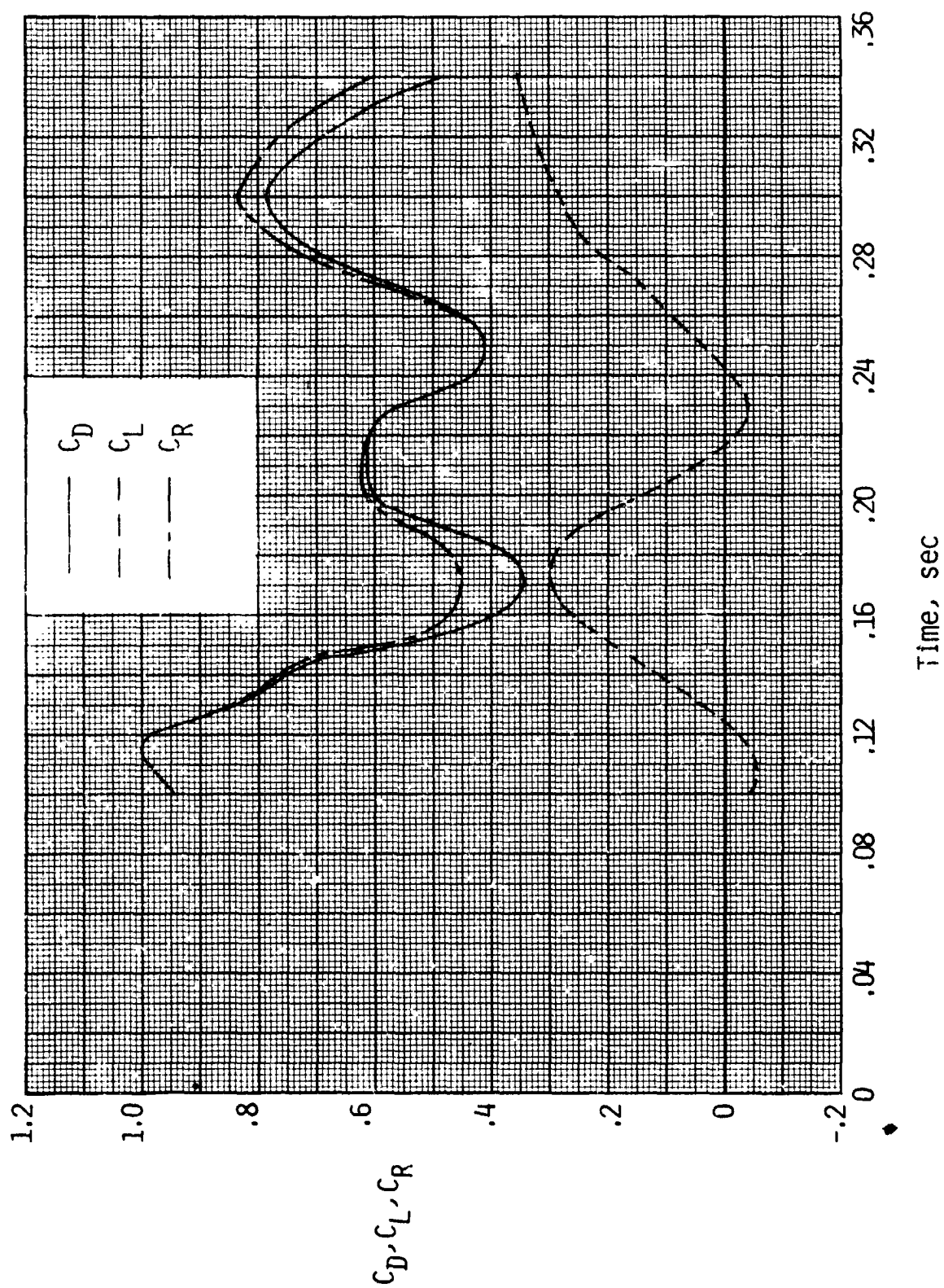
(c) Variation of lift, drag, and resultant-force coefficients with time.

Figure 13. Continued.
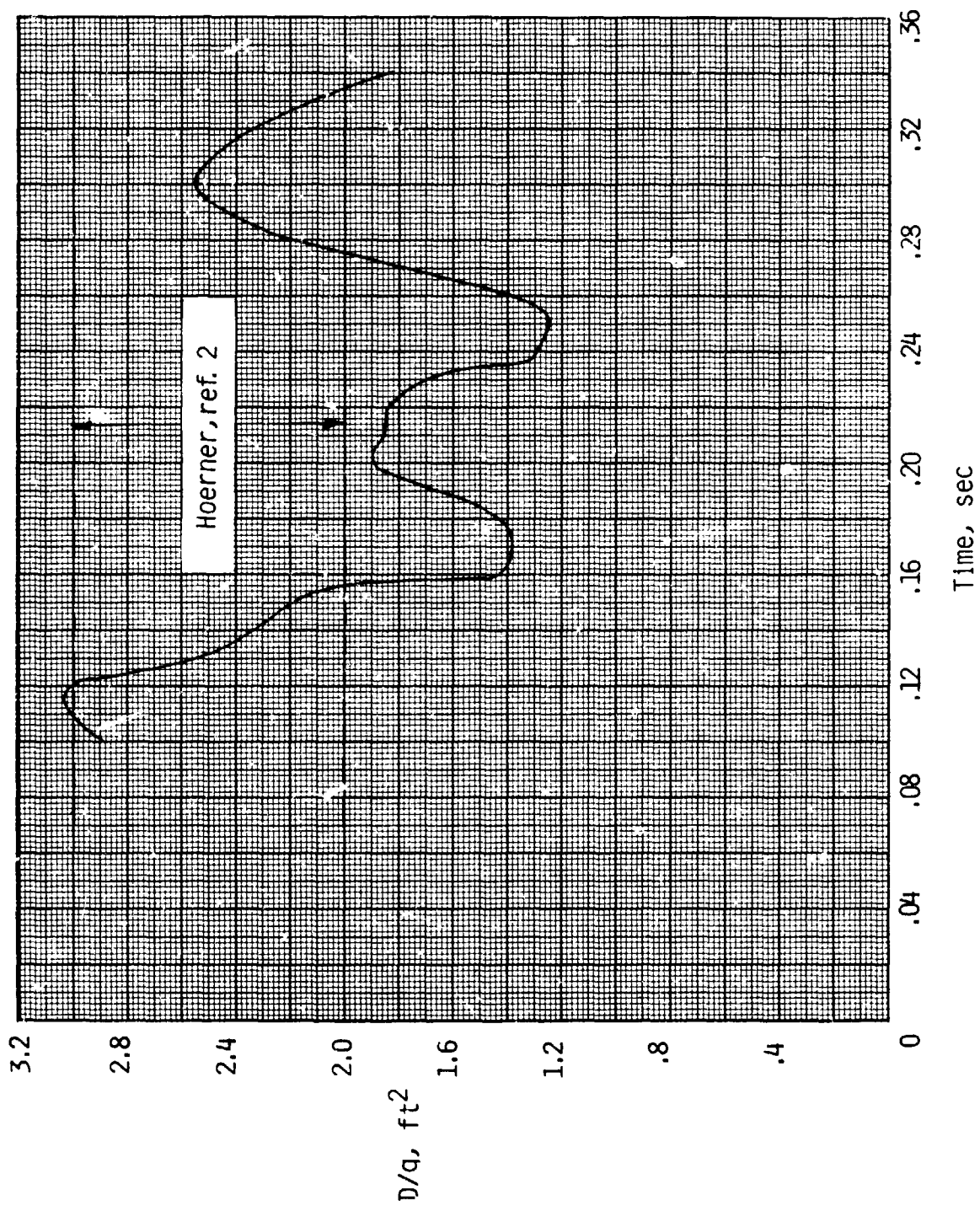
(d) Variation of equivalent full-scale body drag area, D/q, with time.

Figure 13. Concluded.
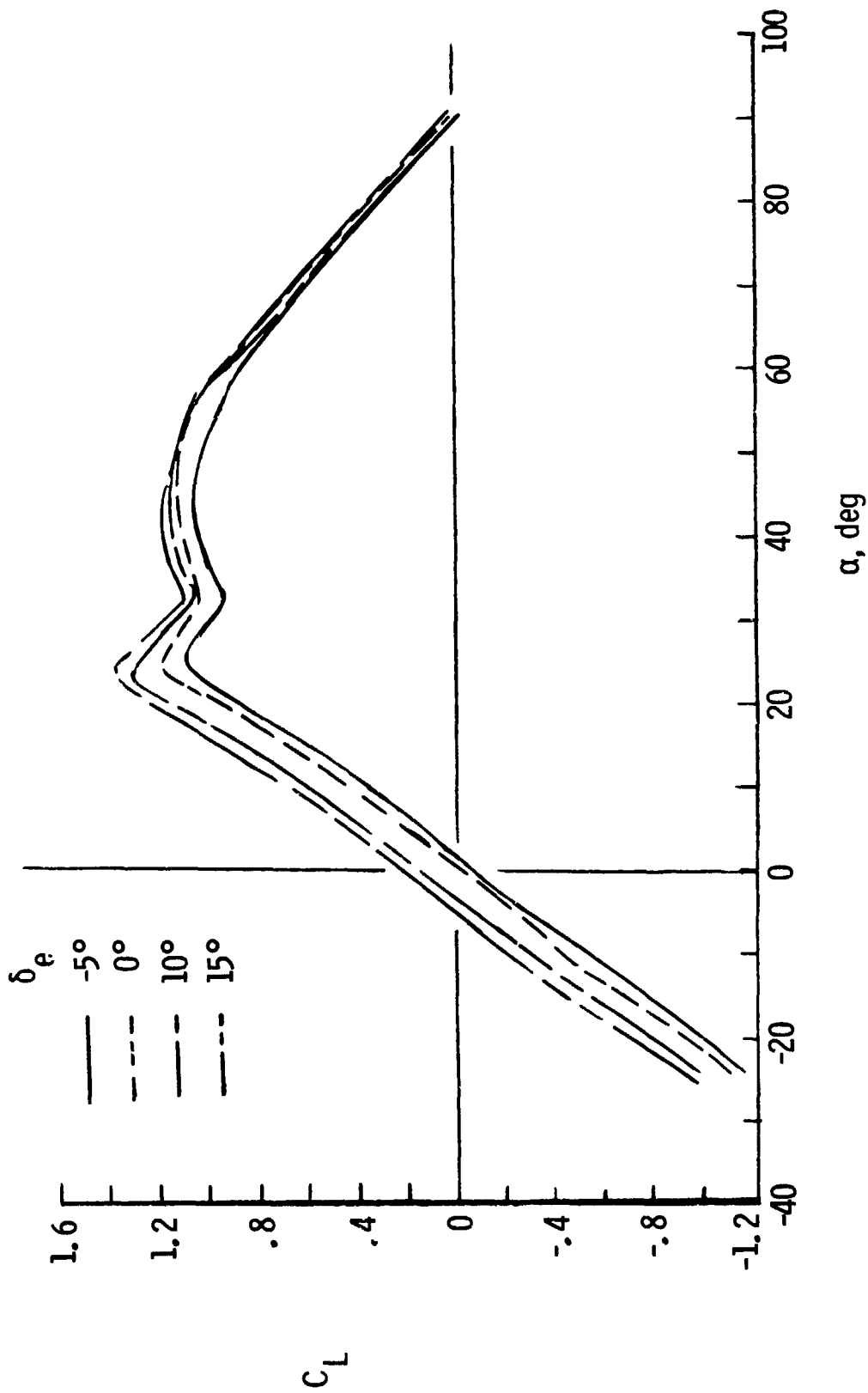
(a) Lift coefficient versus angle of attack.

Figure 14. Orbiter aerodynamics. $\delta_{BF} = 16.15°$; $\delta_{SB} = 0°$; $x_{cg}/l = 0.65$.
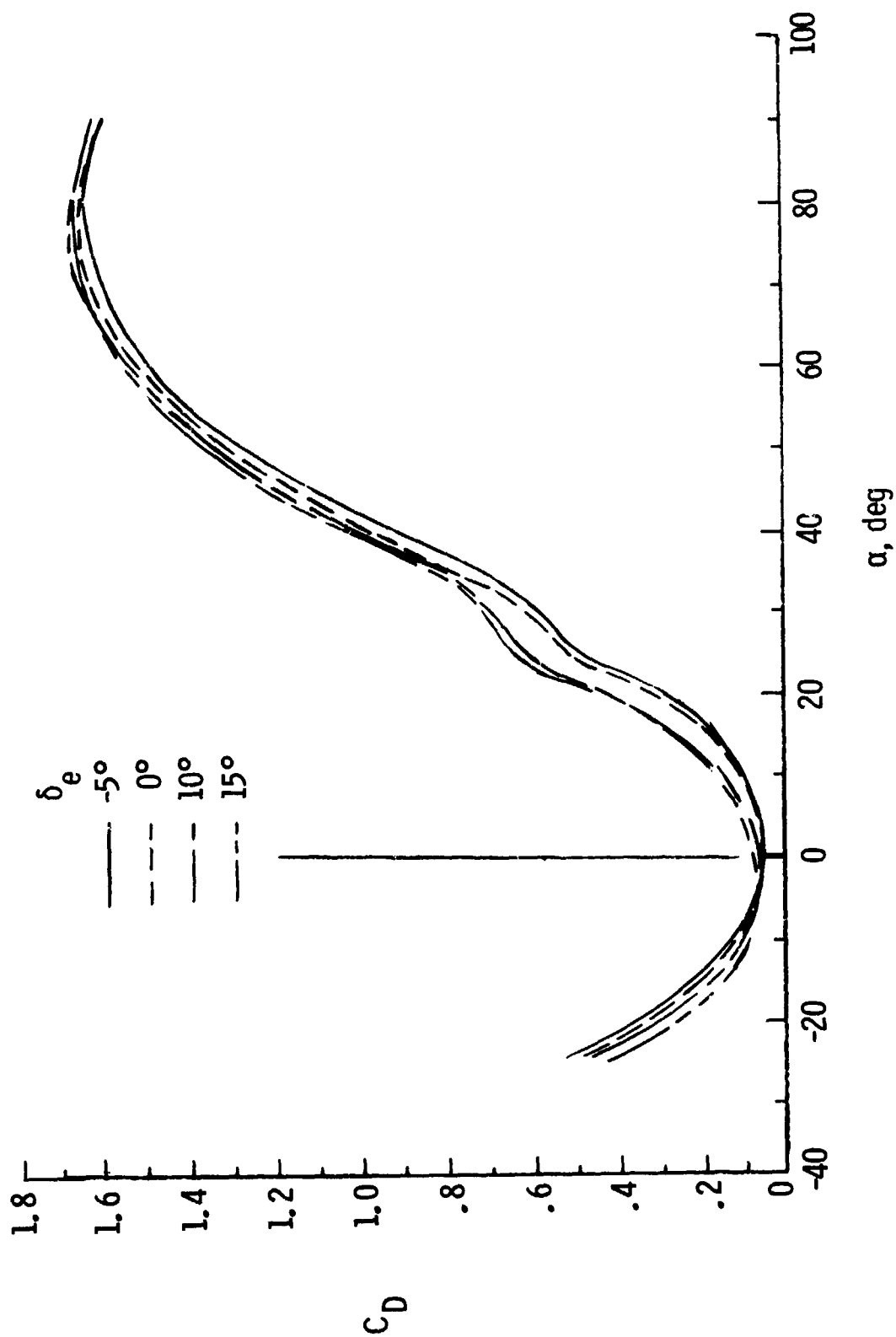
(b) Drag coefficient versus angle of attack.

Figure 14. Continued.
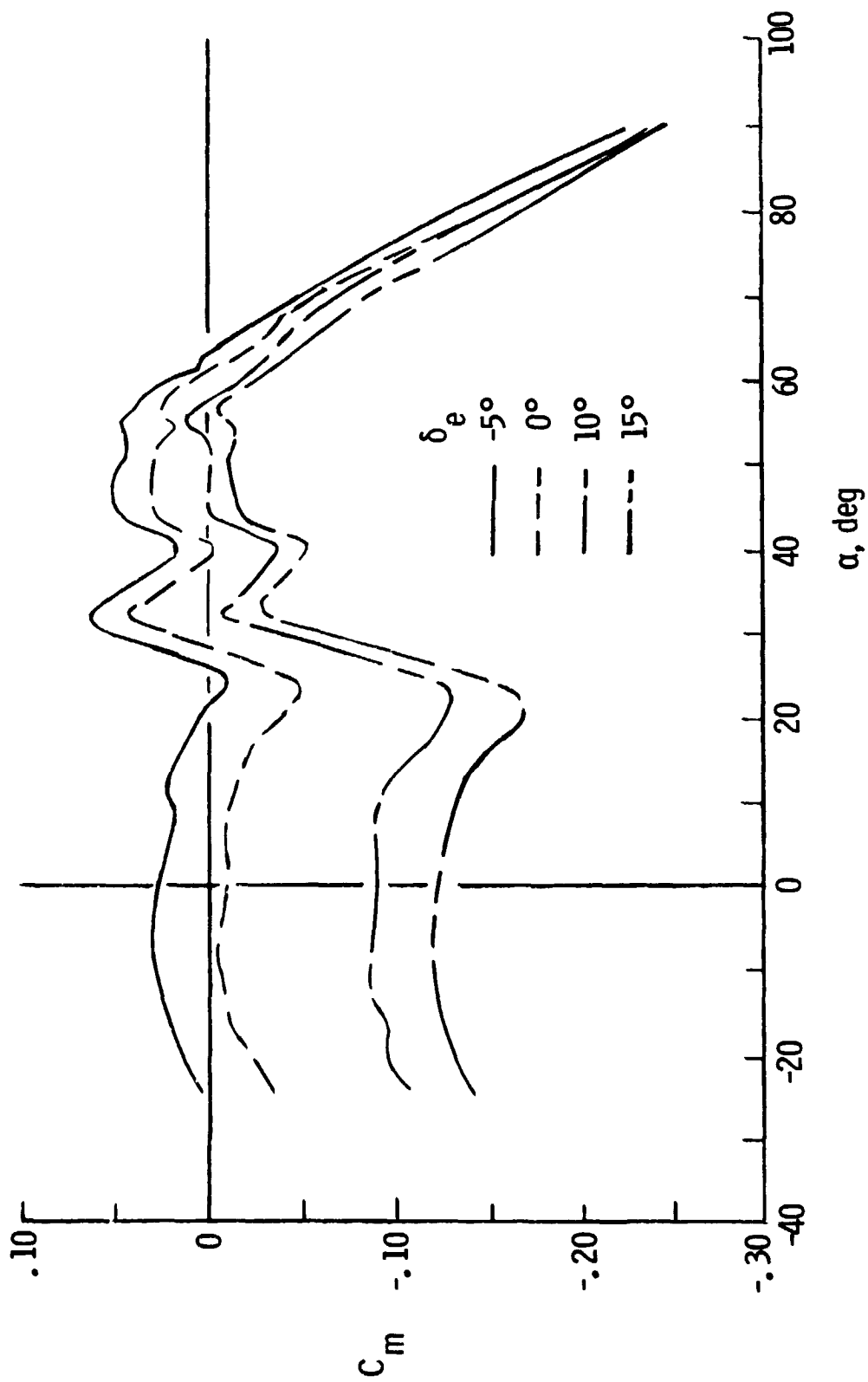
(c) Pitching-moment coefficient versus angle of attack.

Figure 14. Concluded.
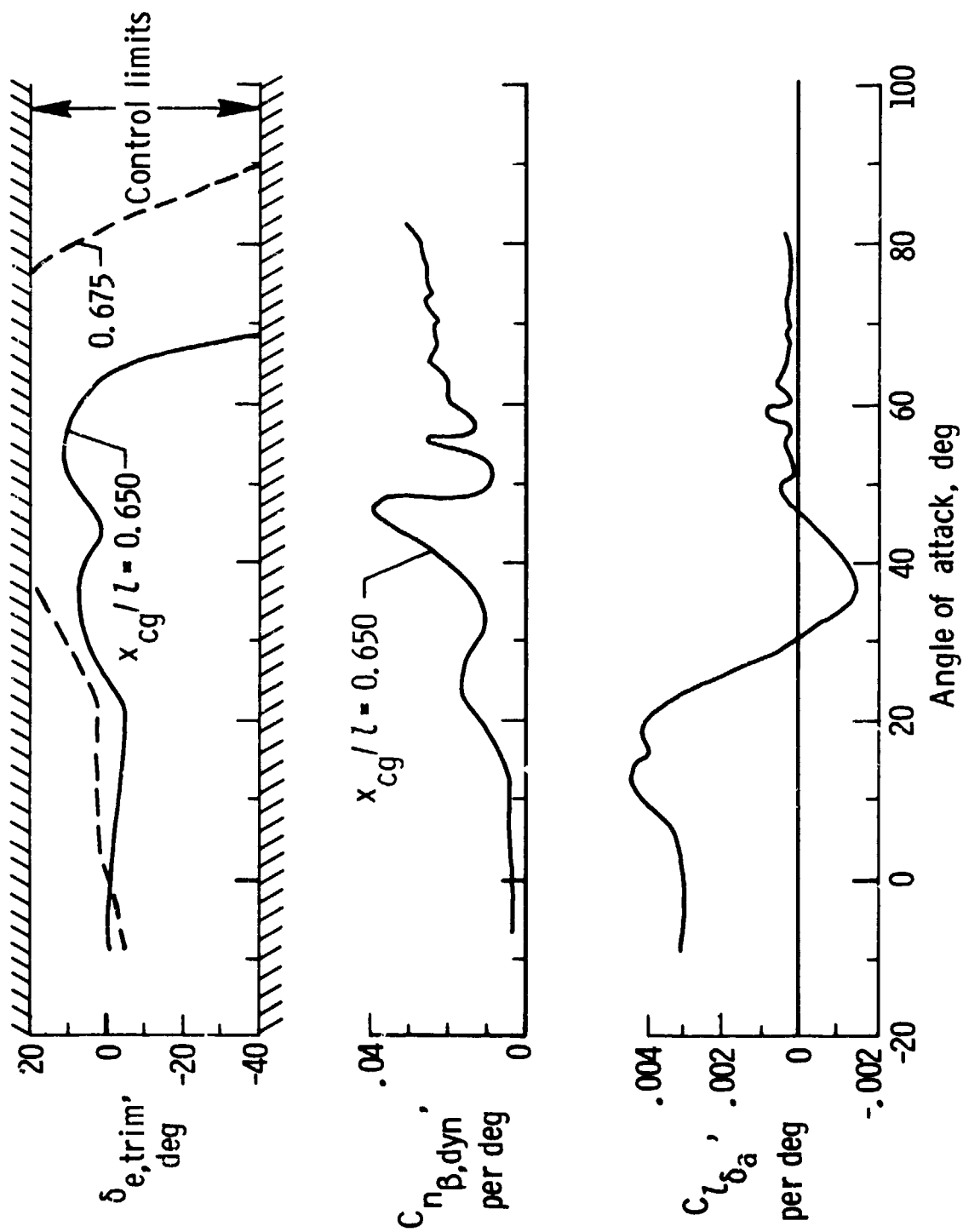
Figure 15. Longitudinal-control, lateral-stability, and lateral-control characteristics of the orbiter. δ_{BF} = 16.5°; δ_{SB} = 0°.
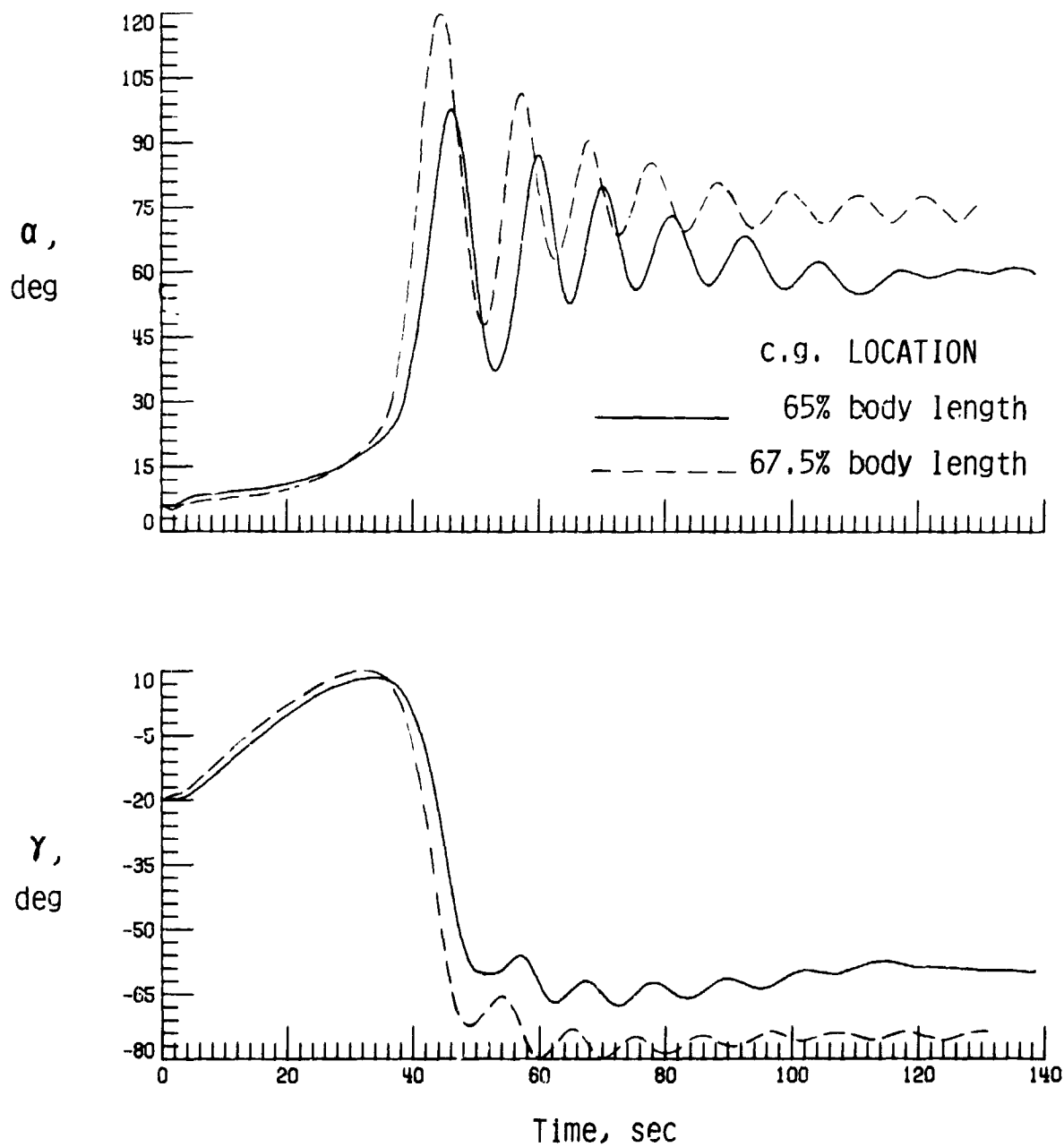
(a) Variation of angle of attack and flight-path angle with time.

Figure 16. Results from simulation of subsonic, high-angle-of-attack trim maneuver for maximum fore and aft c.g. locations. Initial conditions: $\alpha = 6°$; $h = 20\,000$ ft; $M = 0.6$; $W = 190\,000$ lb.
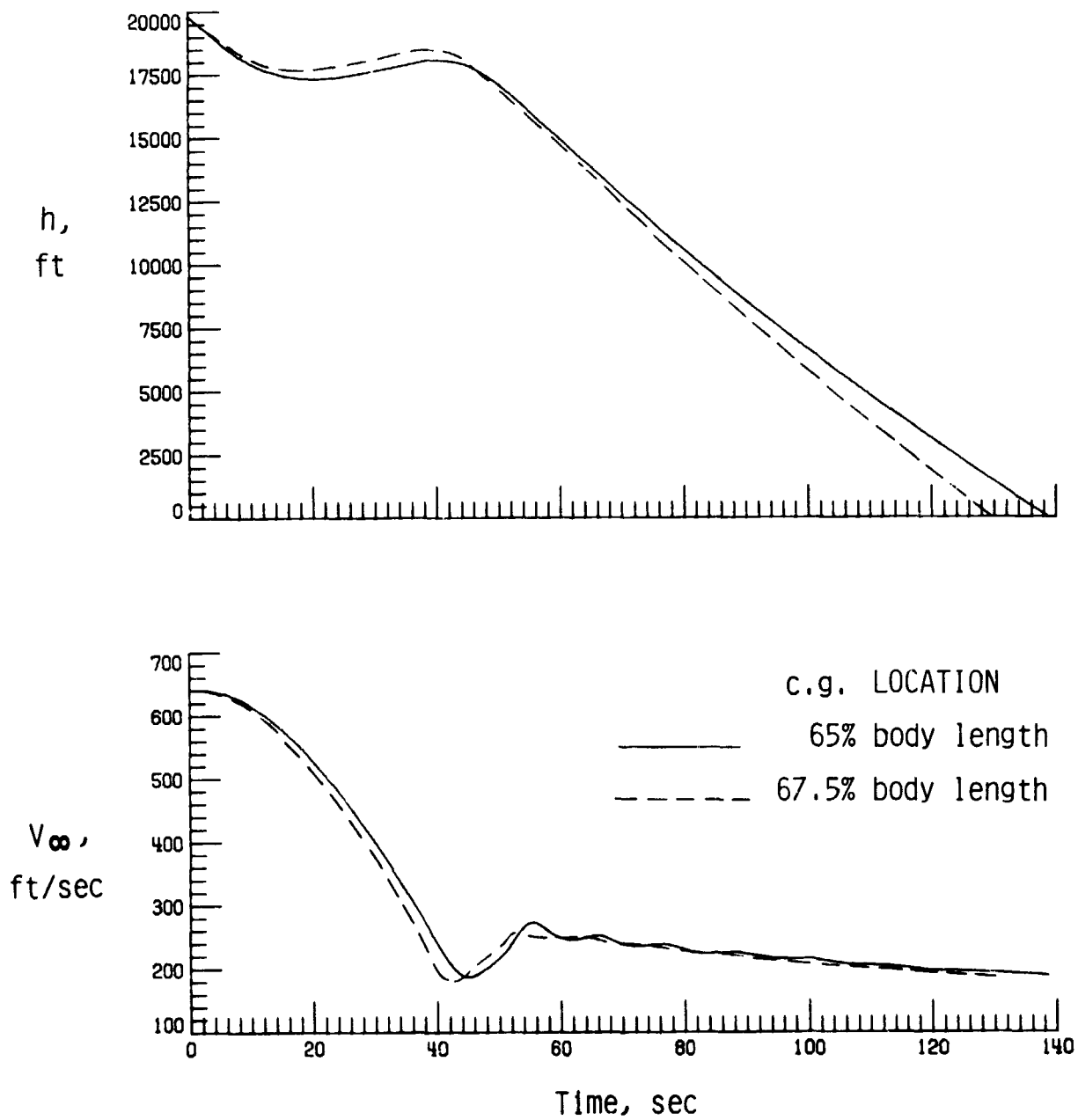
(b) Variation of altitude and velocity with time.

Figure 16. Continued.
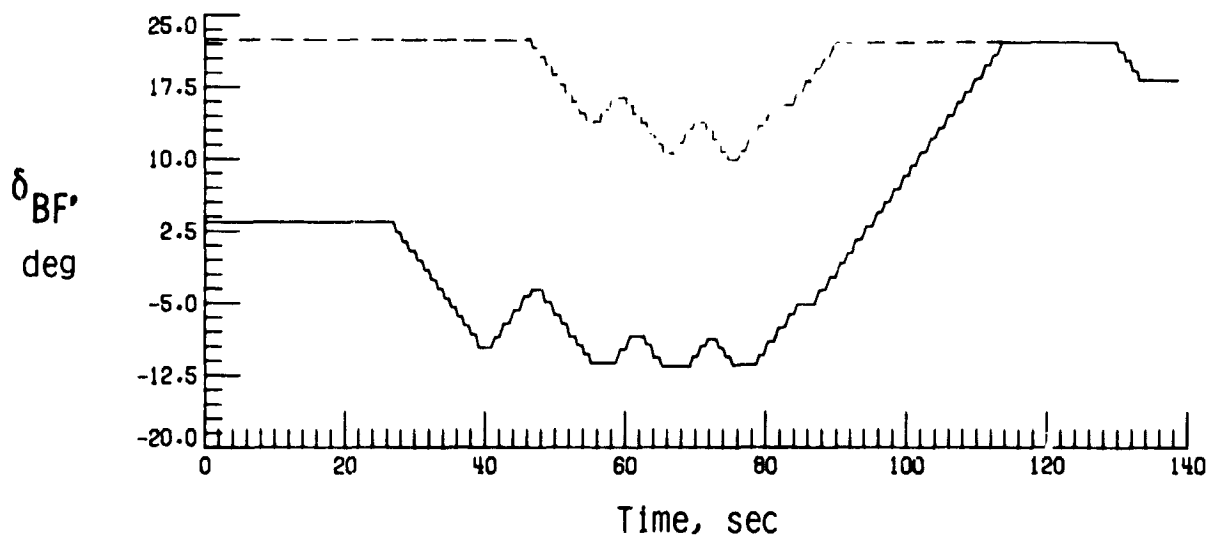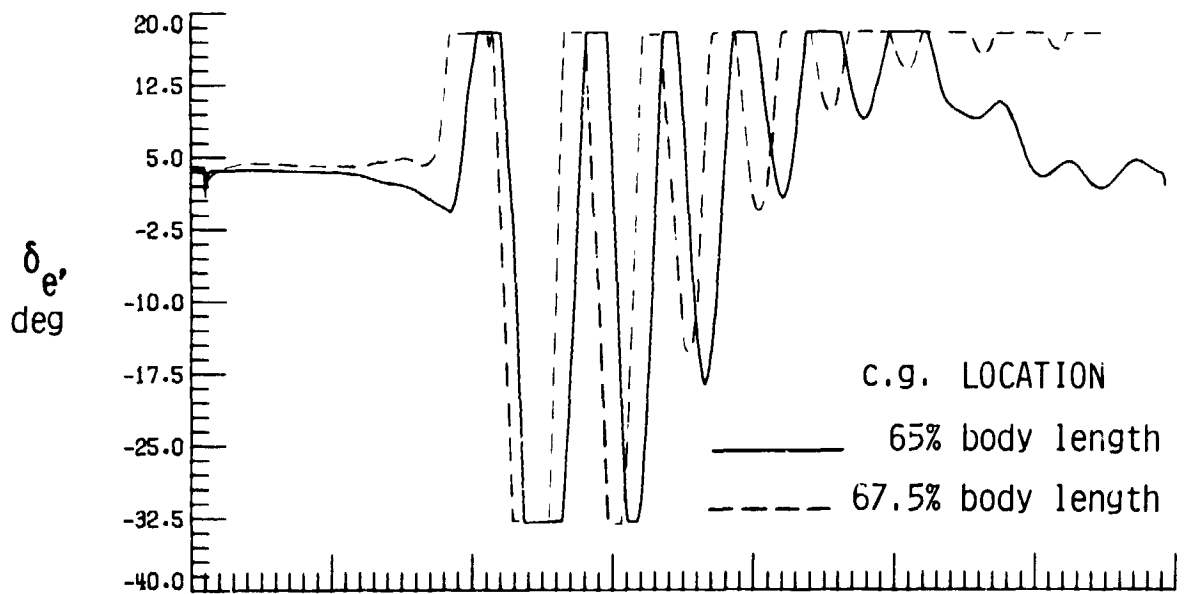
(c) Variation of elevon and speed-brake deflection with time.

Figure 16. Concluded.
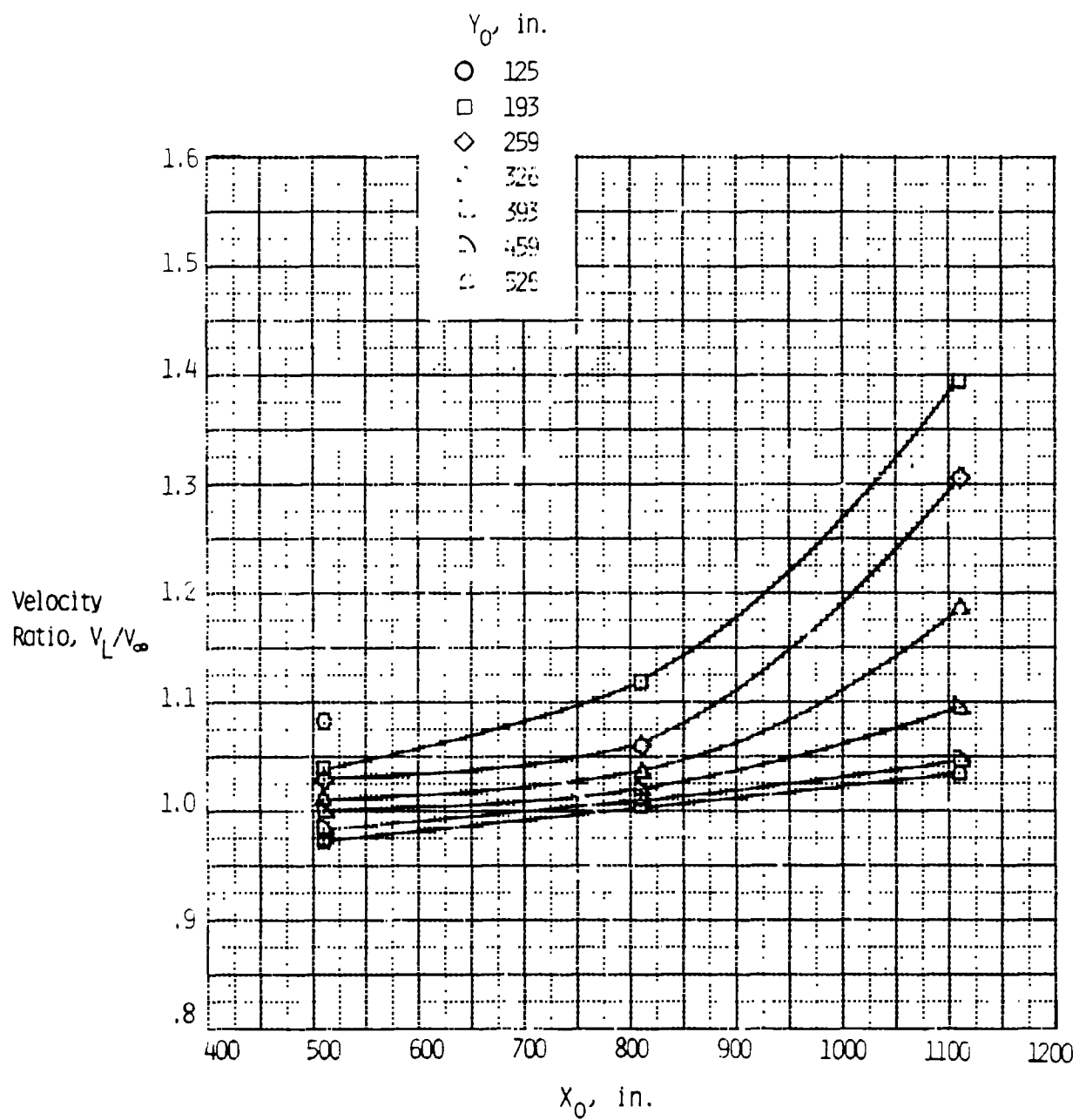
(a) Velocity ratio; $V_\infty = 63.2$ ft/sec.

Figure 17. Variation of flow-field parameters with longitudinal position of several spanwise stations. $Z_o = 367.0$ in.; $\alpha = 17.5°$; $\beta = 0°$.
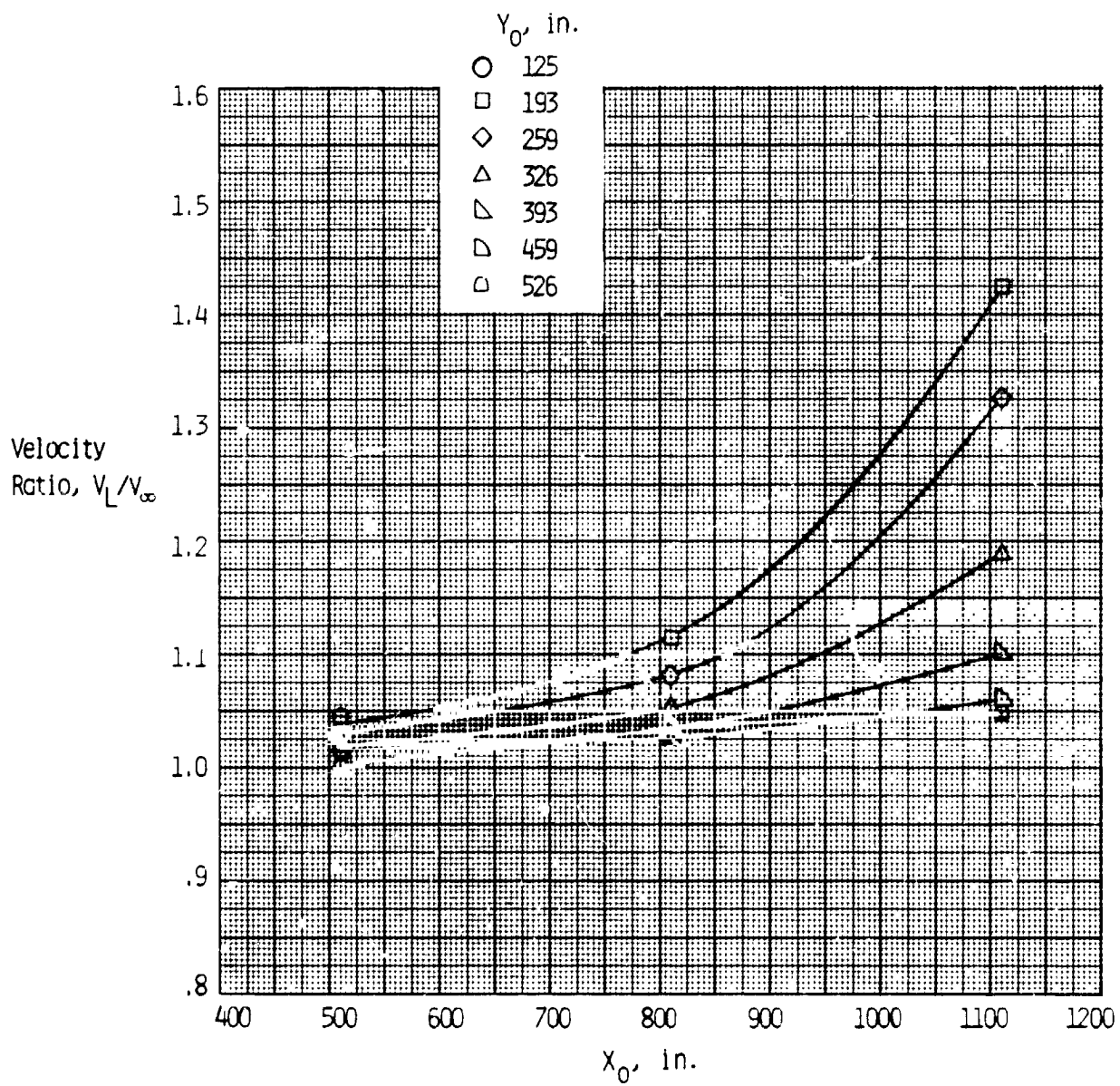
(b) Velocity ratio; $V_\infty = 157.2$ ft/sec.

Figure 17. Continued.
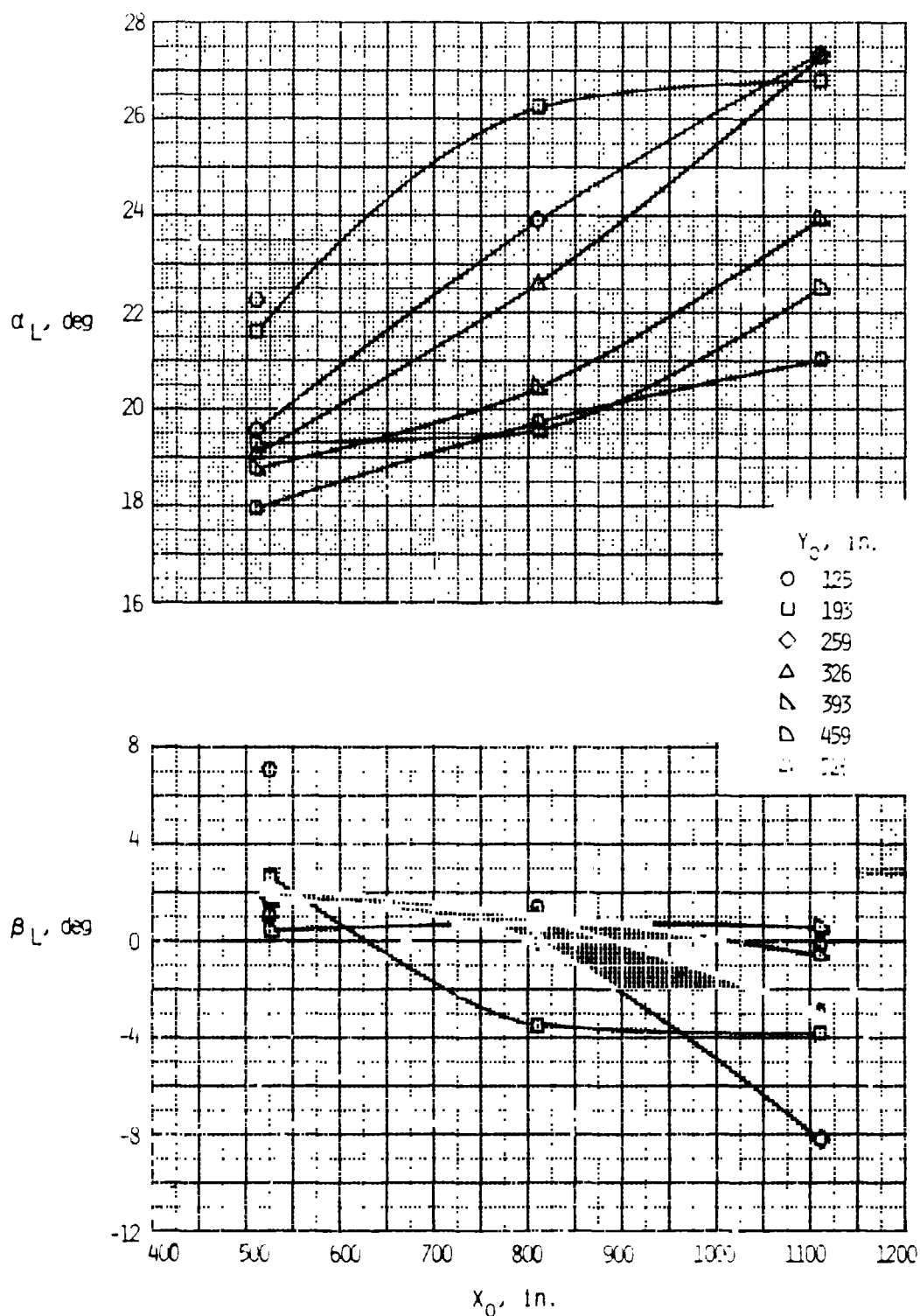
(c) Local angles of attack and sideslip; $V_\infty = 60.2$ ft/sec.

Figure 17. Continued.
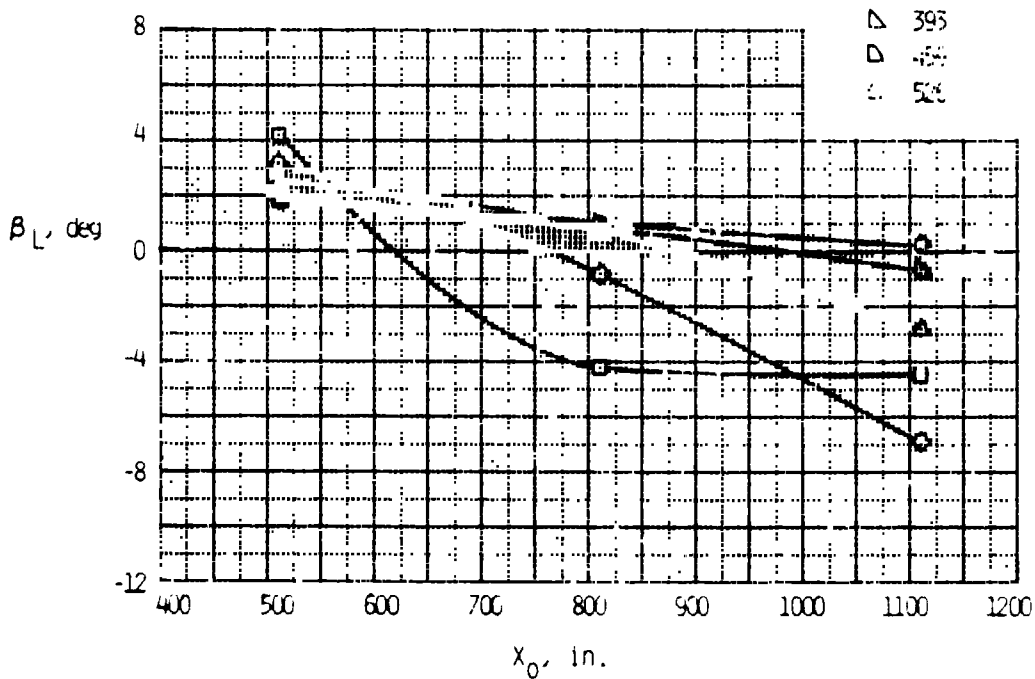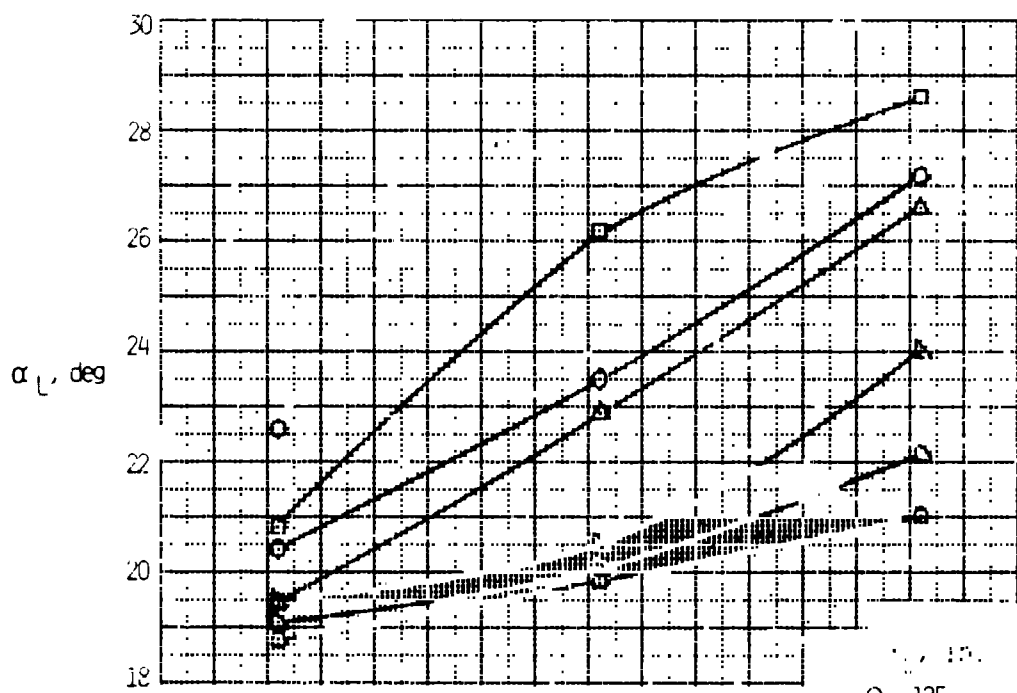
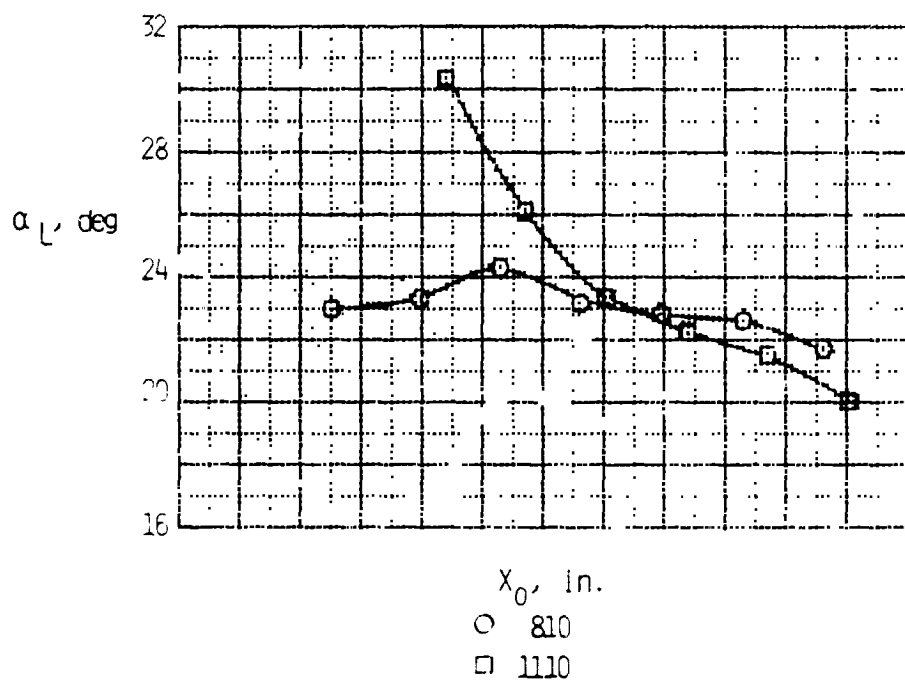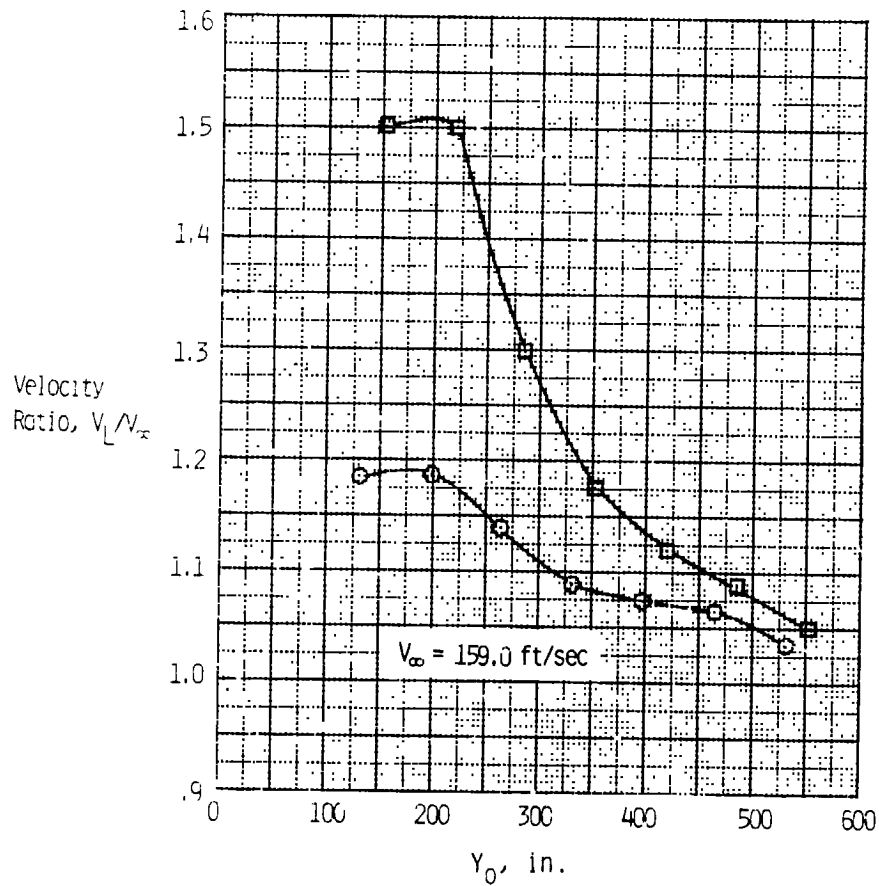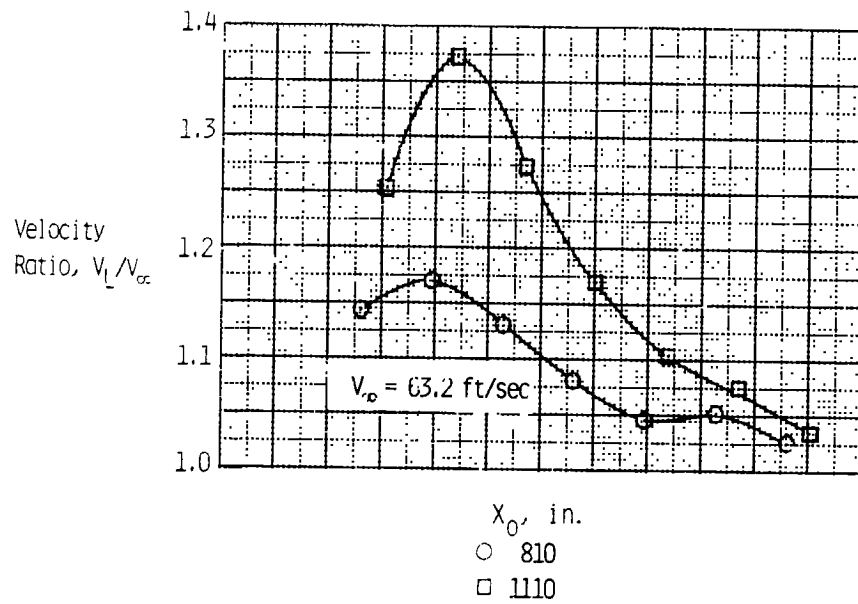(d) Local angles of attack and sideslip; $V_\infty = 157.2$ ft/sec.

Figure 17. Concluded.
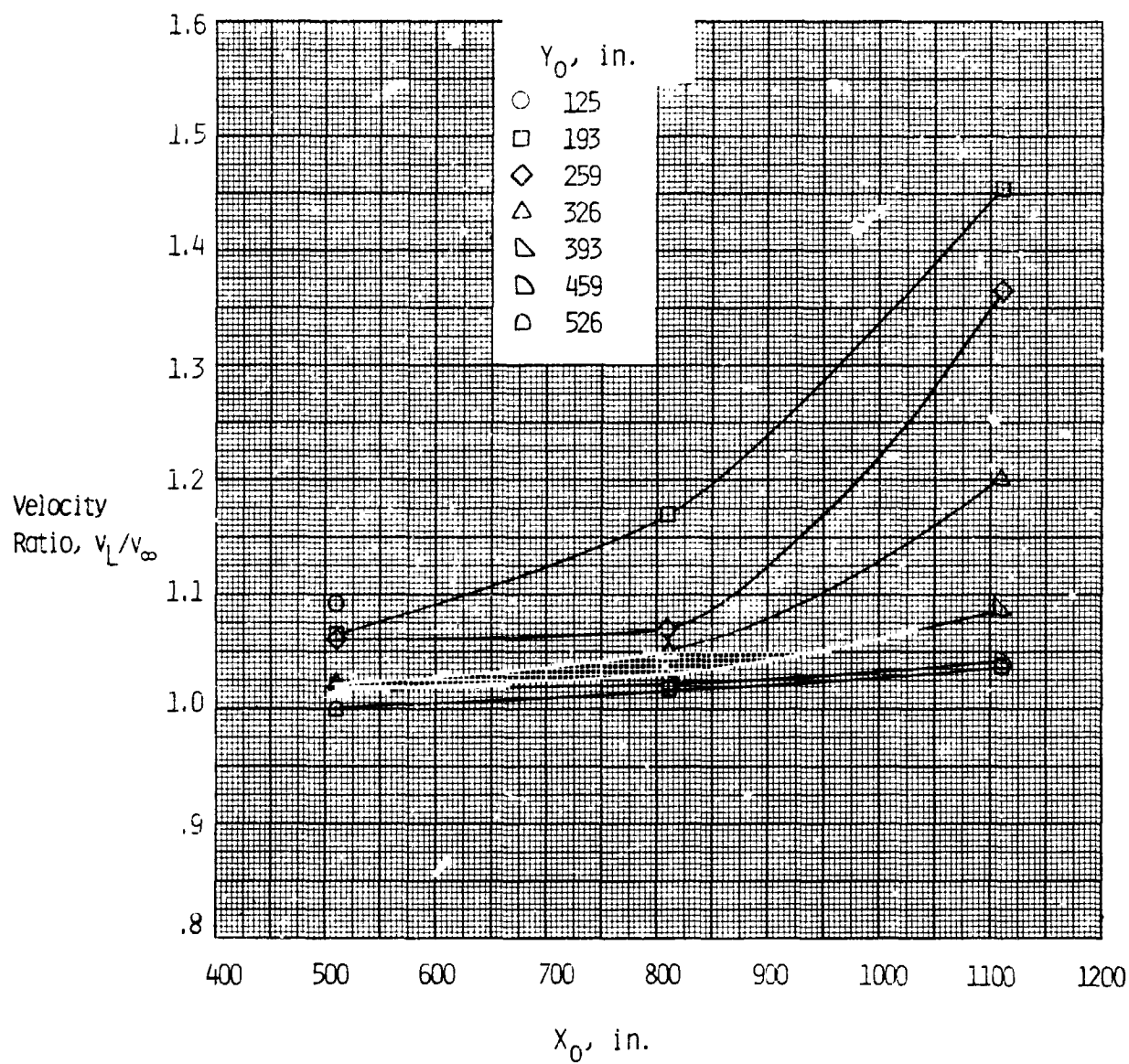
(a) Velocity ratio; $V_\infty = 62.4$ ft/sec.

Figure 18. Variation of flow-field parameters with longitudinal position at several spanwise stations. $Z_o = 367.0$ in.; $\alpha = 20°$; $\beta = 0°$.
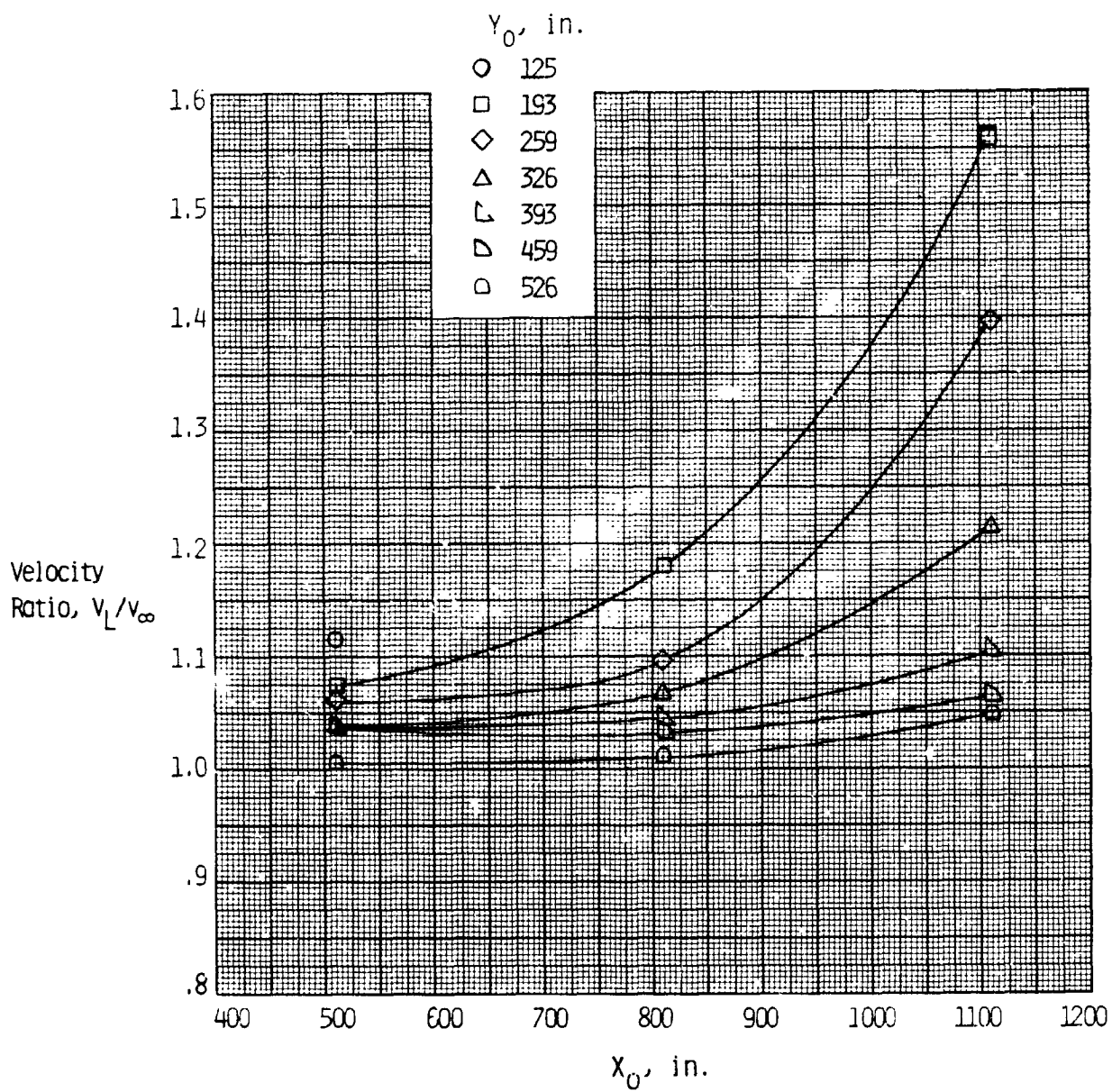
(b) Velocity ratio; $V_\infty = 157.4$ ft/sec.

Figure 18. Continued.
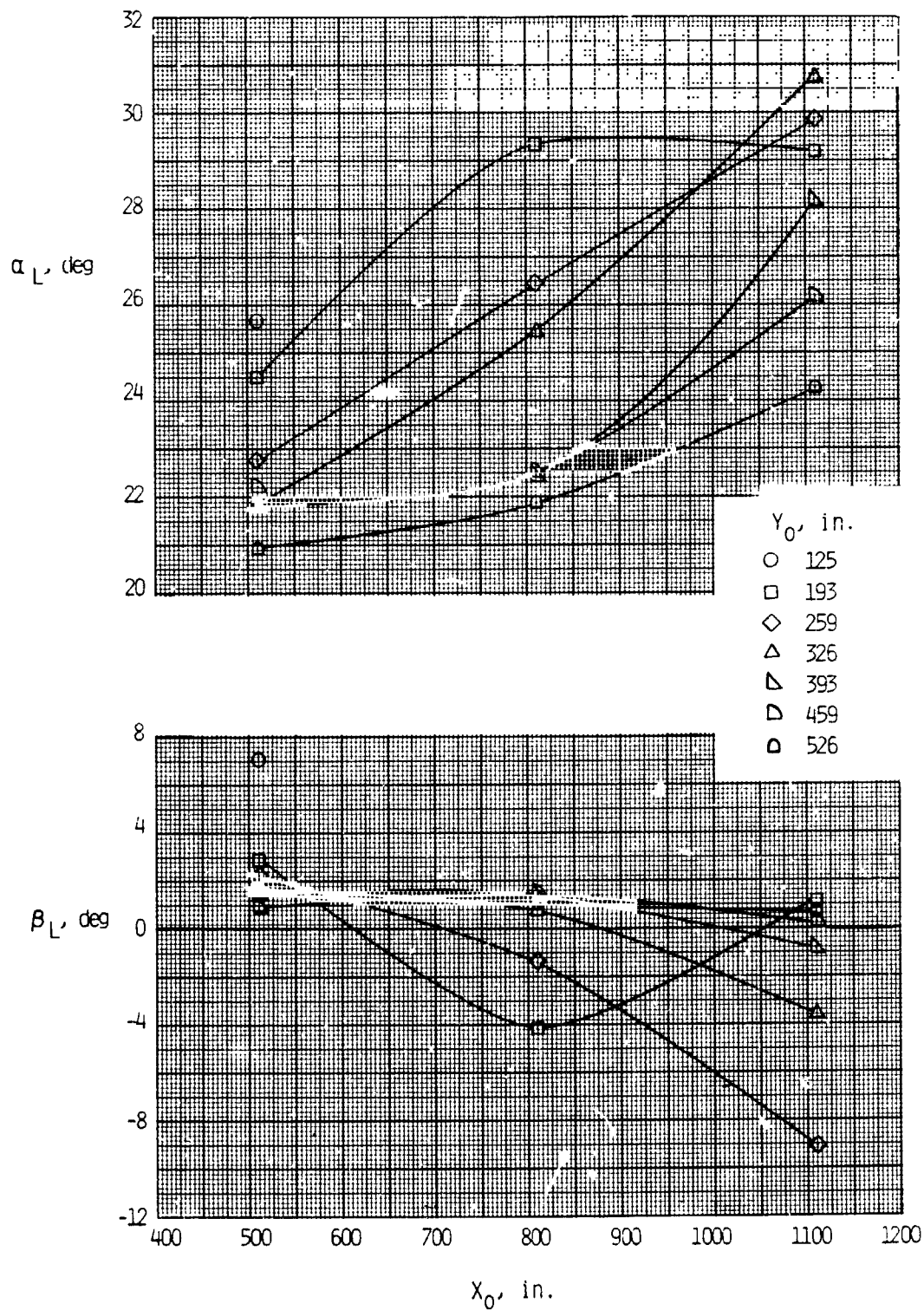
(c) Local angles of attack and sideslip; $V_\infty = 62.4$ ft/sec.

Figure 18. Continued.
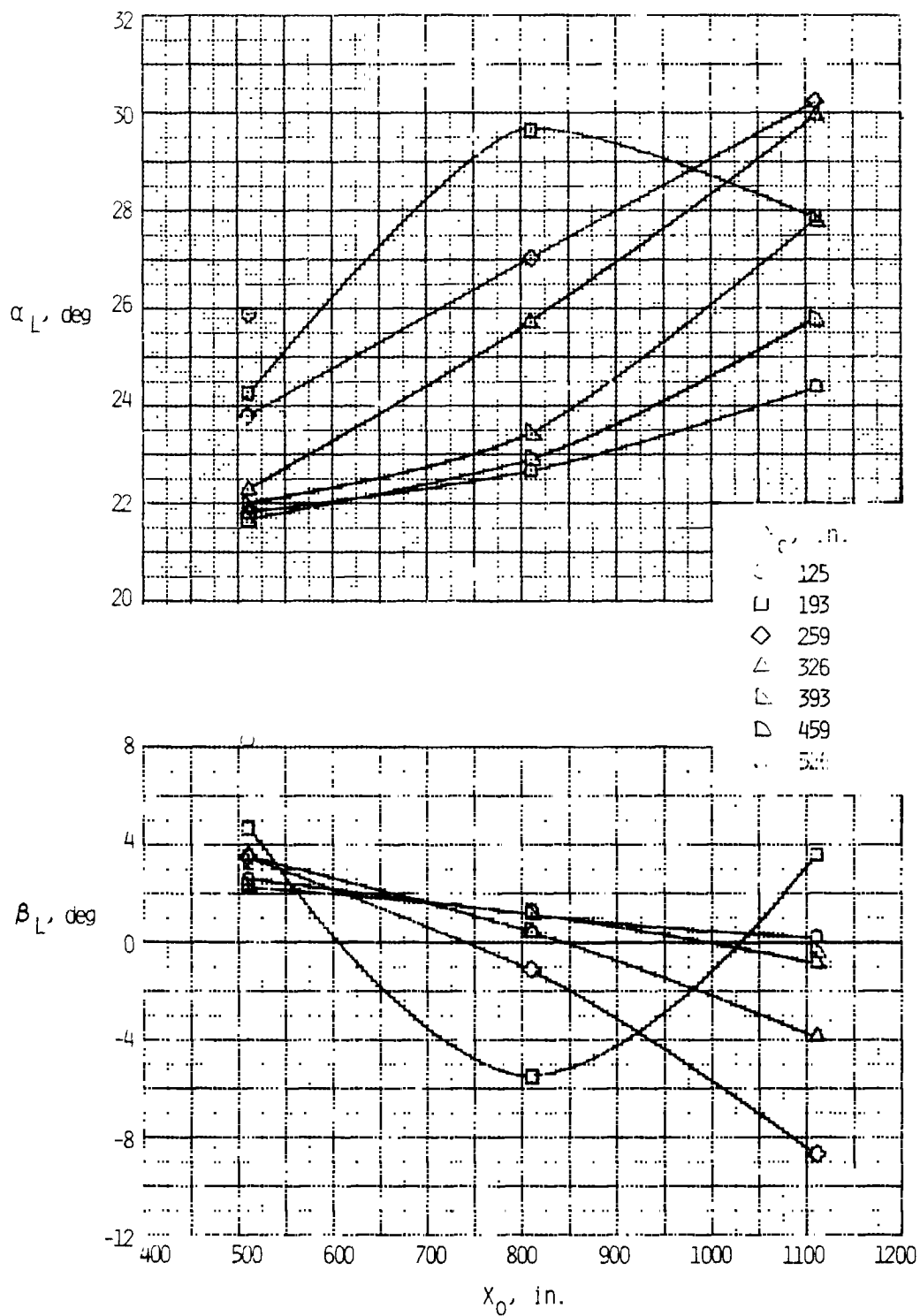
(d) Local angles of attack and sideslip; $V_\infty = 157.4$ ft/sec.
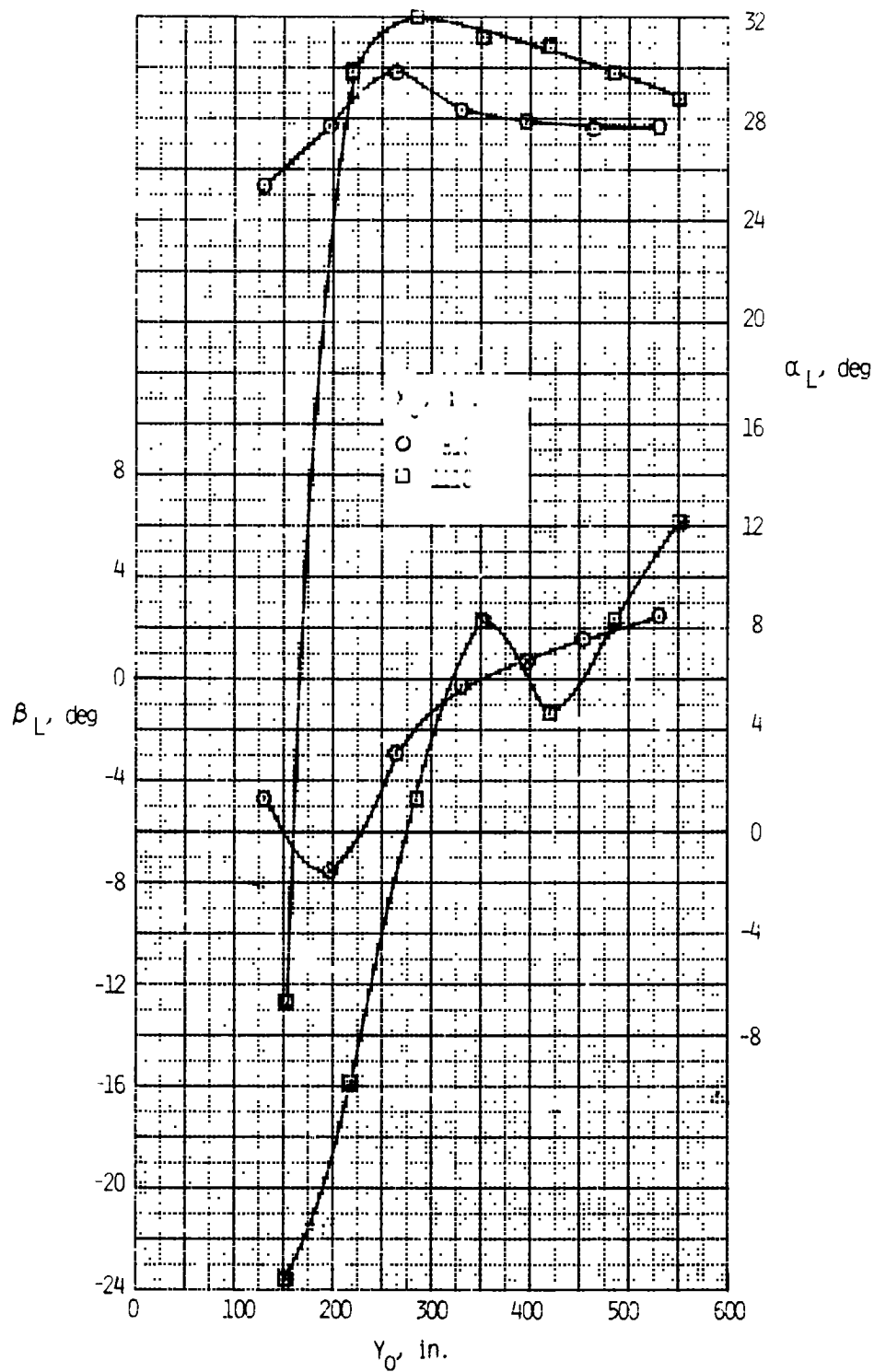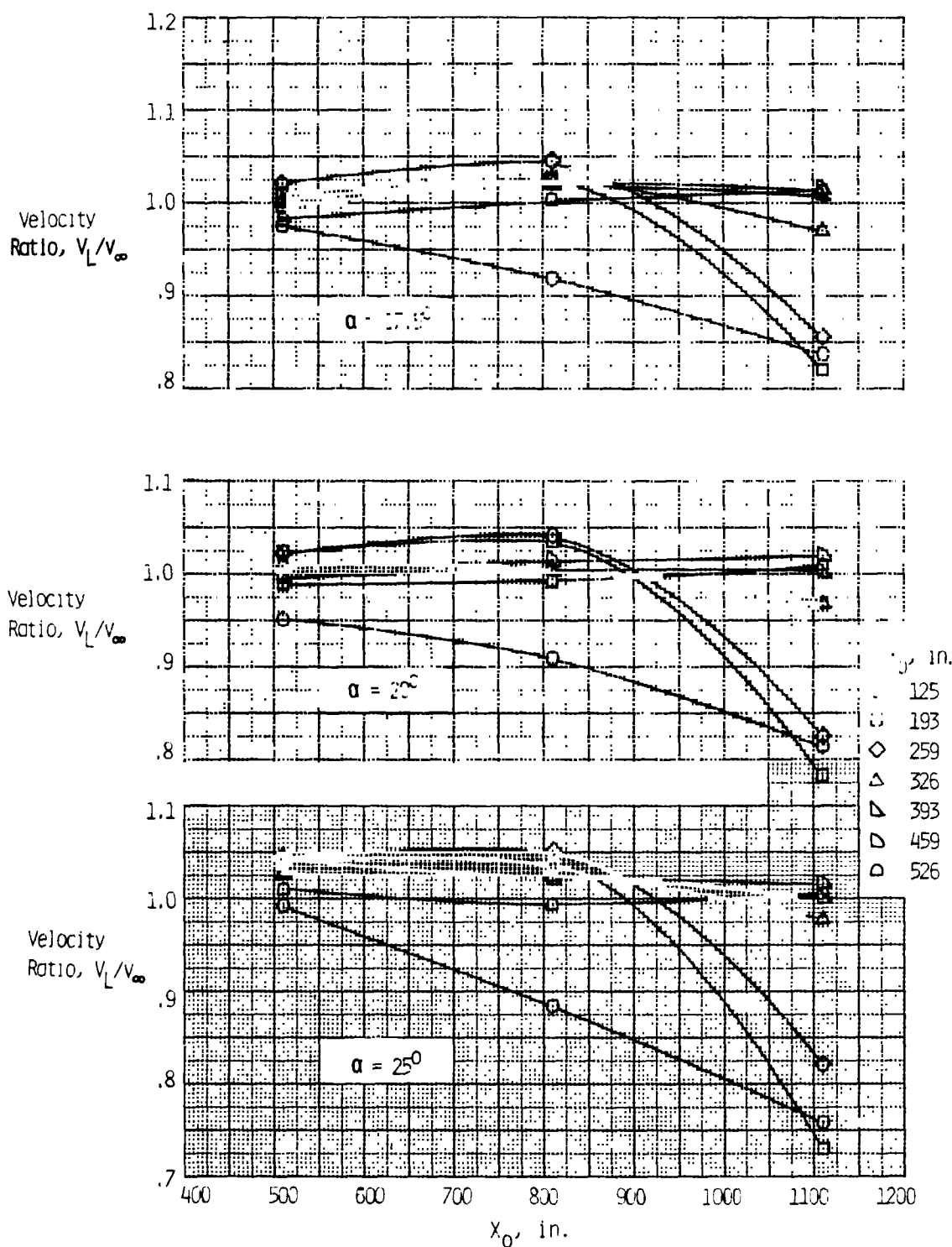
Figure 18. Concluded.
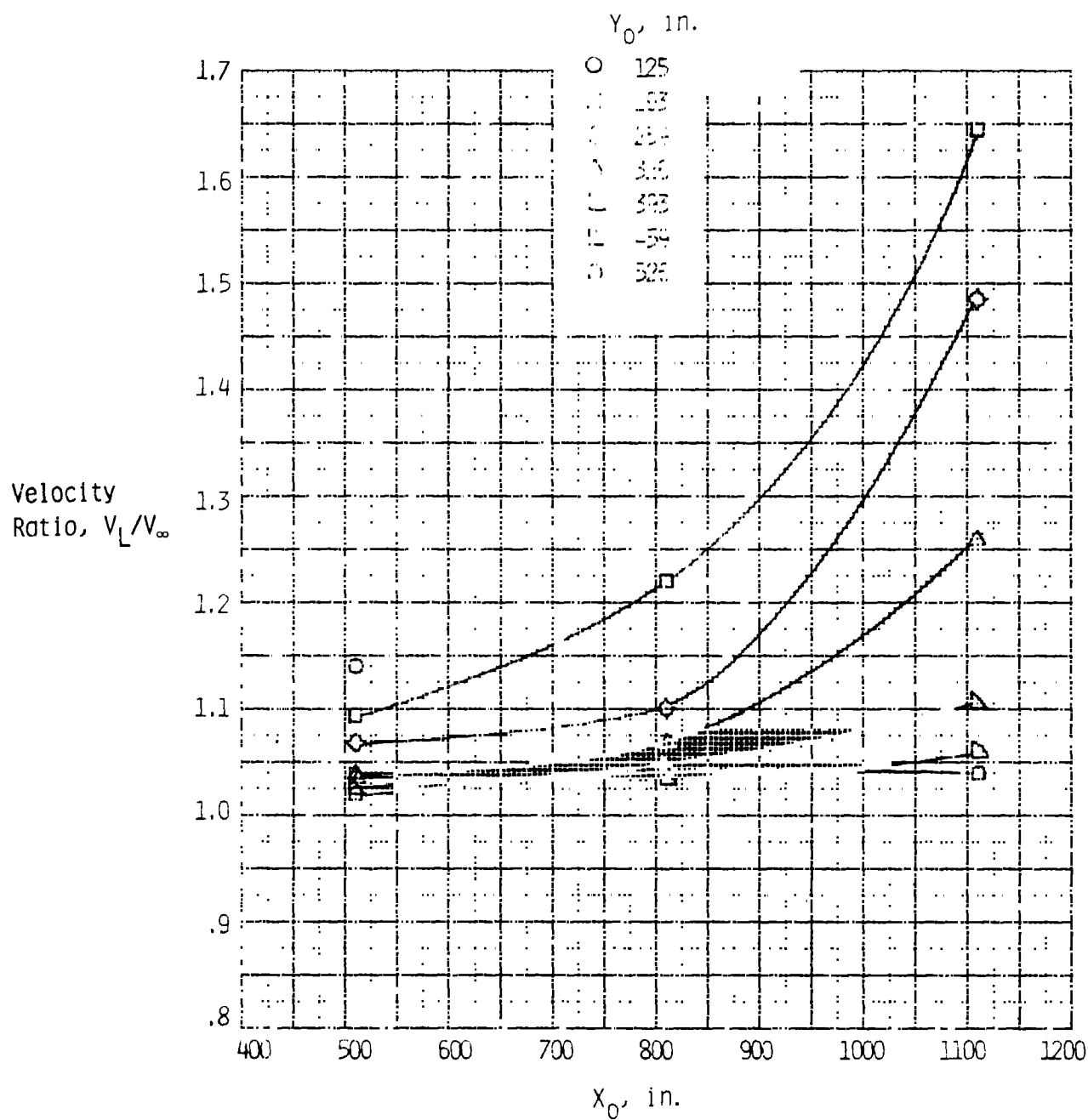
(a) Velocity ratio; $V_\infty = 62.4$ ft/sec.

Figure 19. Variation of flow-field parameters with longitudinal position at several spanwise stations. $Z_o = 367.0$ in.; $\alpha = 25°$; $\beta = 0°$.

44
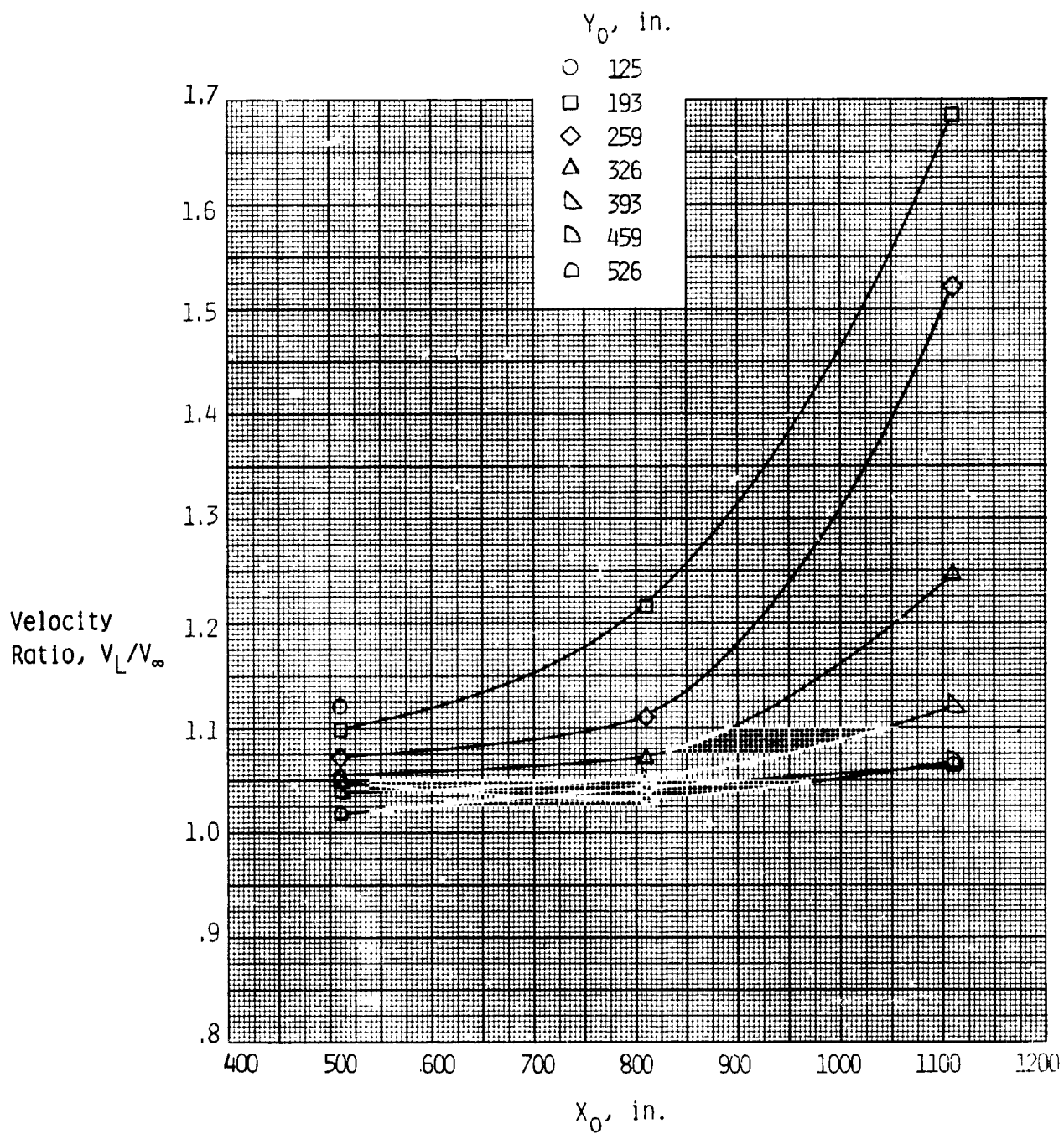
(b) Velocity ratio; $V_\infty = 156.9$ ft/sec.

Figure 19. Continued.
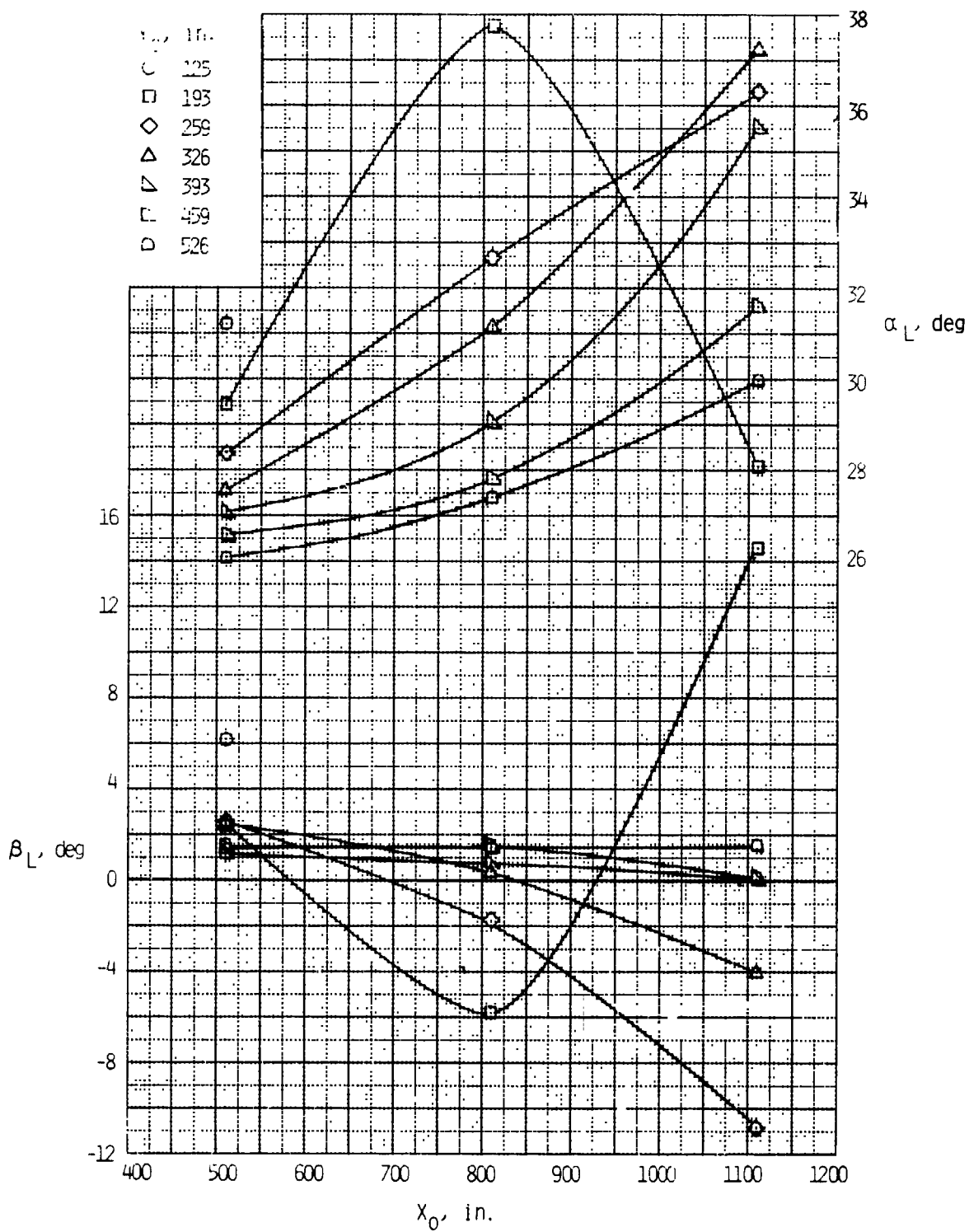
(c) Local angles of attack and sideslip; $V_{\infty} = 62.4$ ft/sec.

Figure 19. Continued.

Y_0, in.

- ○ 125
- □ 193
- ◇ 259
- △ 326
- ◁ 393
- ▽ 459
- ◻ 526

α_L, deg
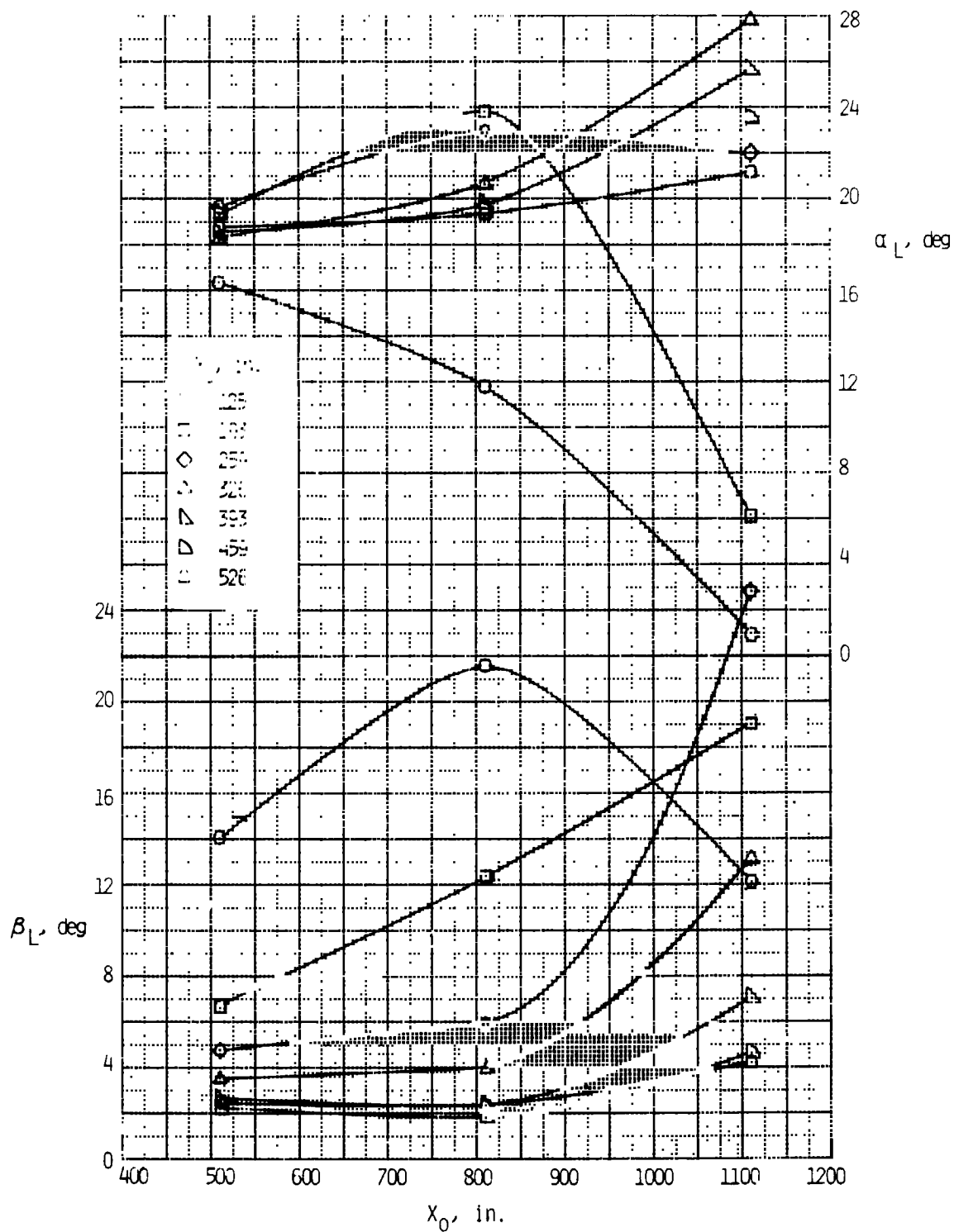
β_L, deg

X_0, in.
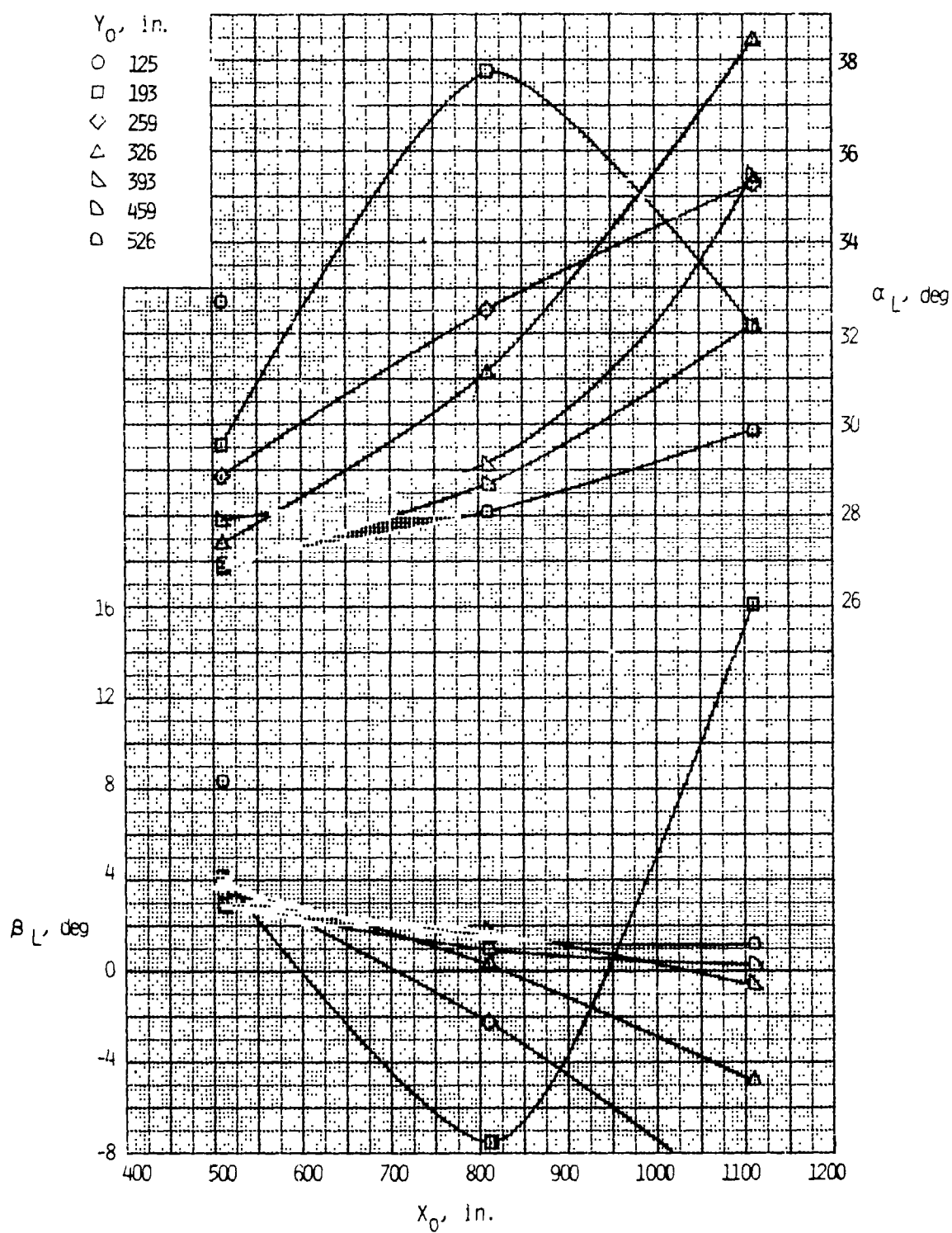
(d) Local angles of attack and sideslip; $V_\infty = 156.9$ ft/sec.

Figure 19. Concluded.
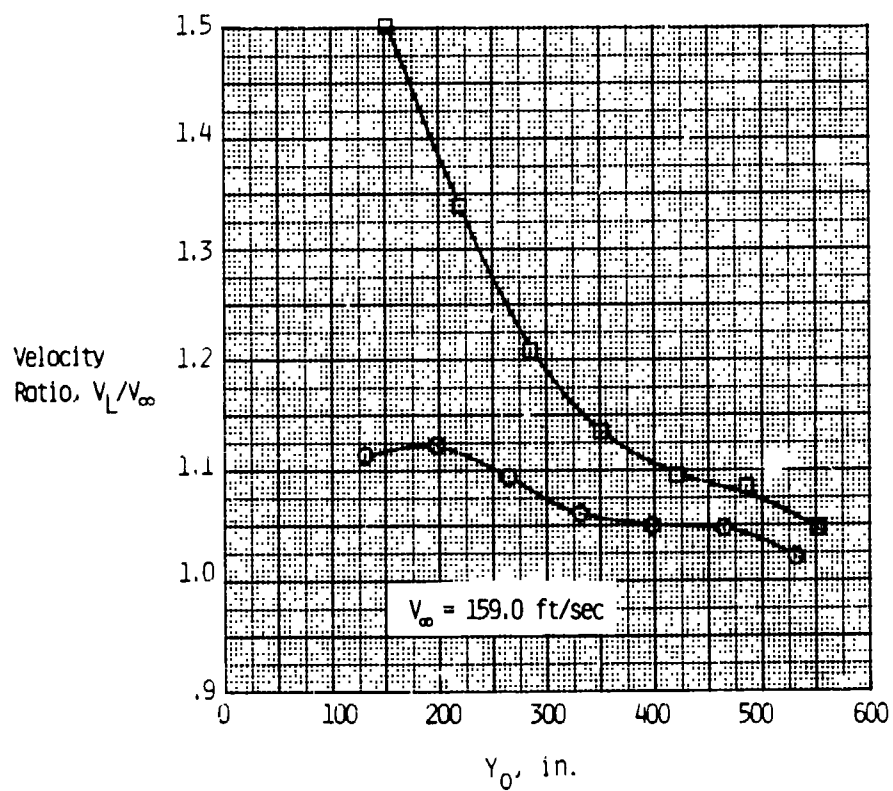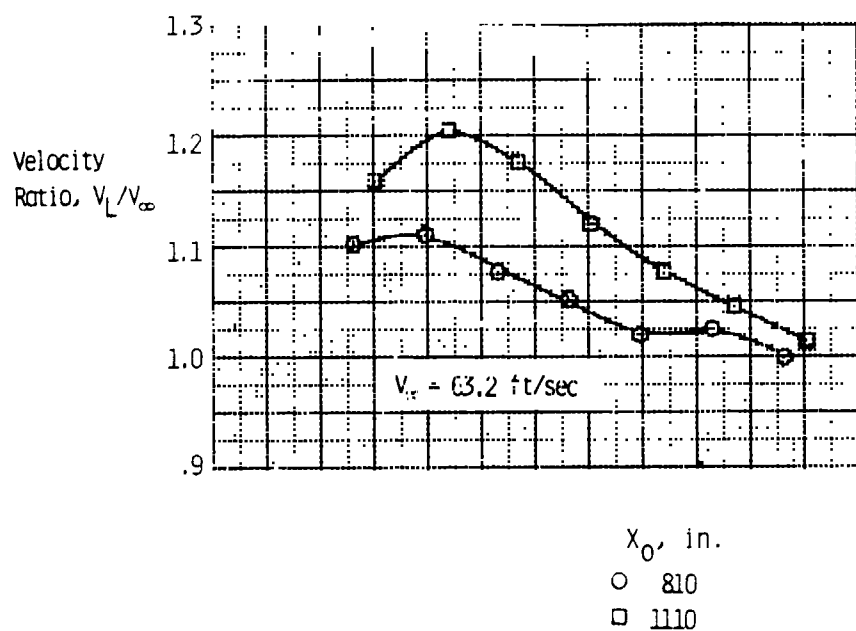
(a) Velocity ratio.

Figure 20. Spanwise variation of flow-field parameters at two longitudinal stations.
$Z_o = 433.0$ in.; $\alpha = 17.5°$; $\beta = 0°$.
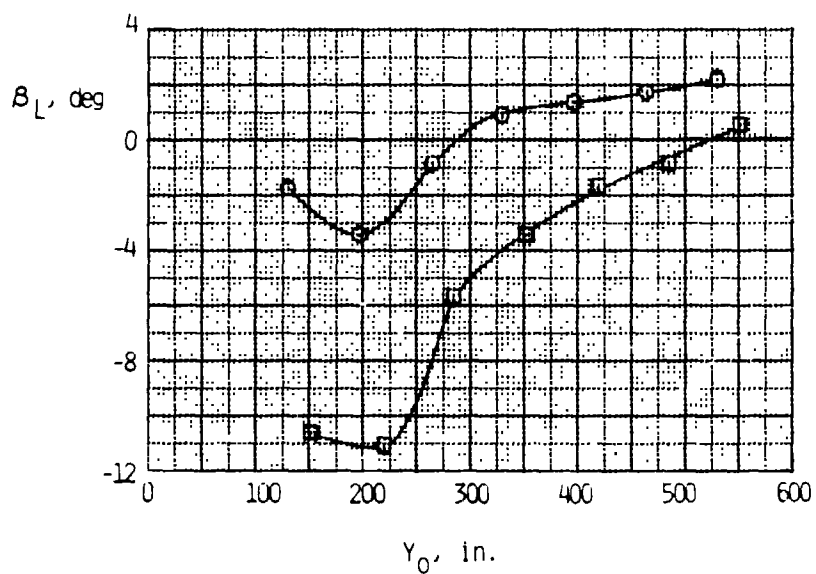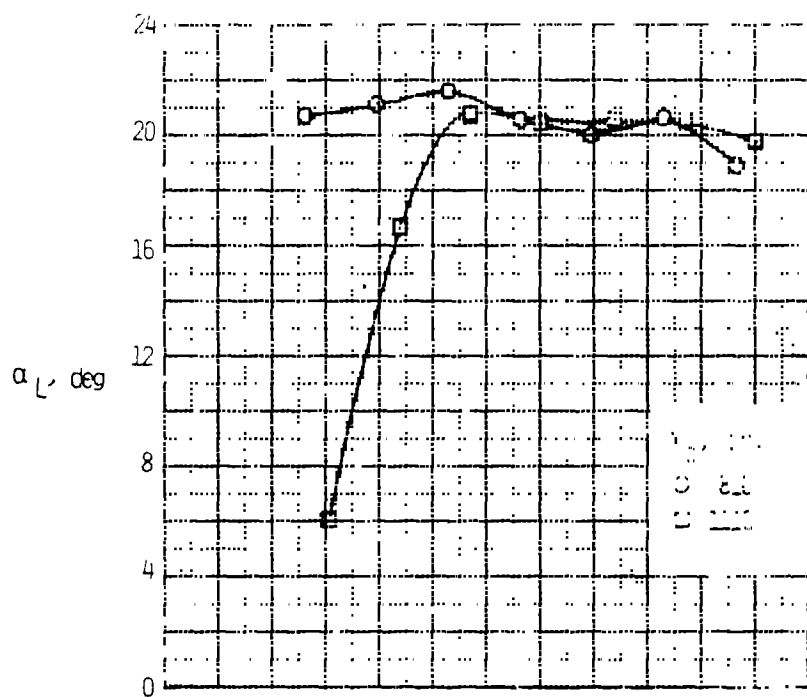
(b) Local angles of attack and sideslip, $V_\infty = 63.2$ ft/sec.

Figure 20. Continued.
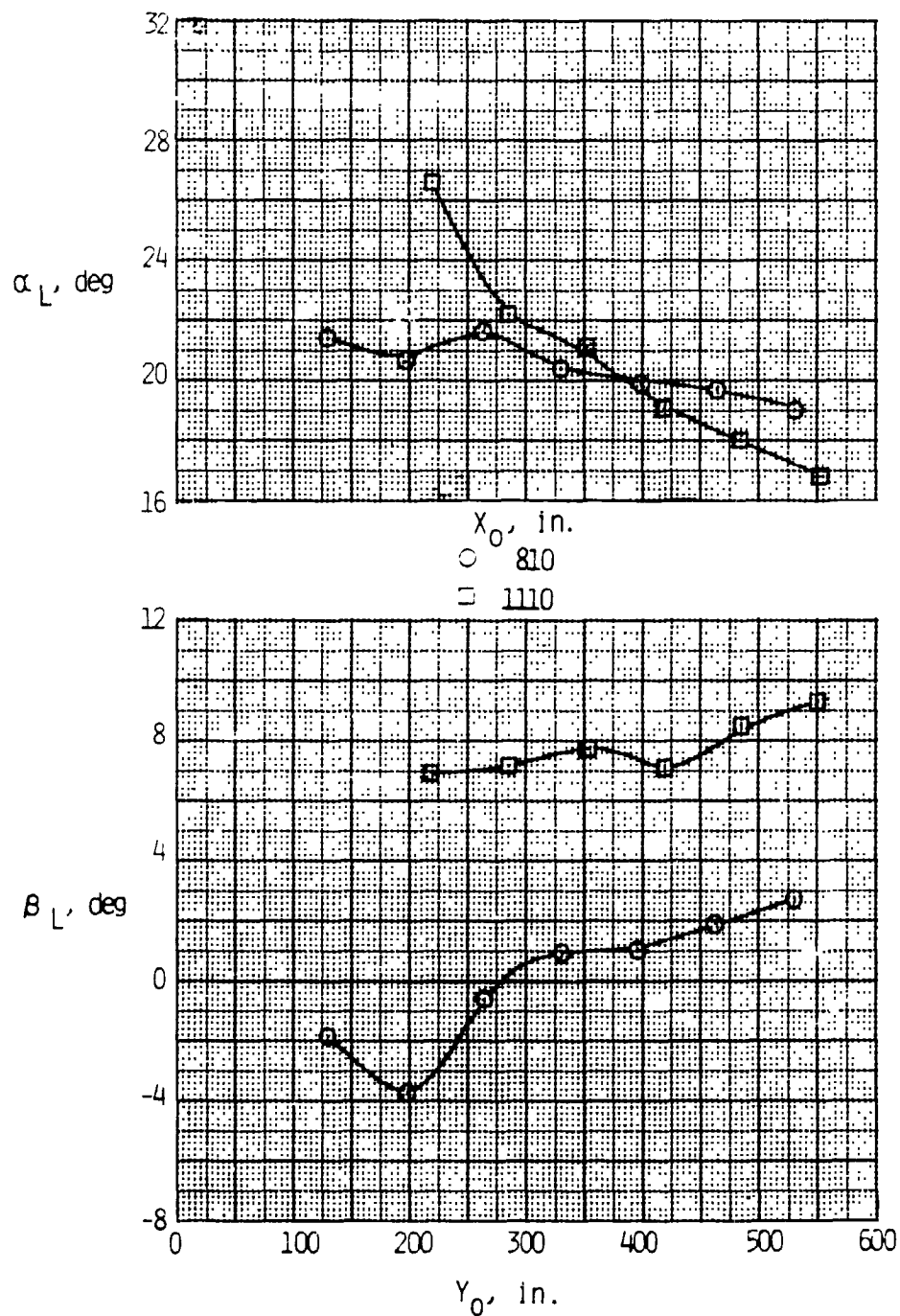
(c) Local angles of attack and sideslip, $V_\infty = 159.0$ ft/sec.
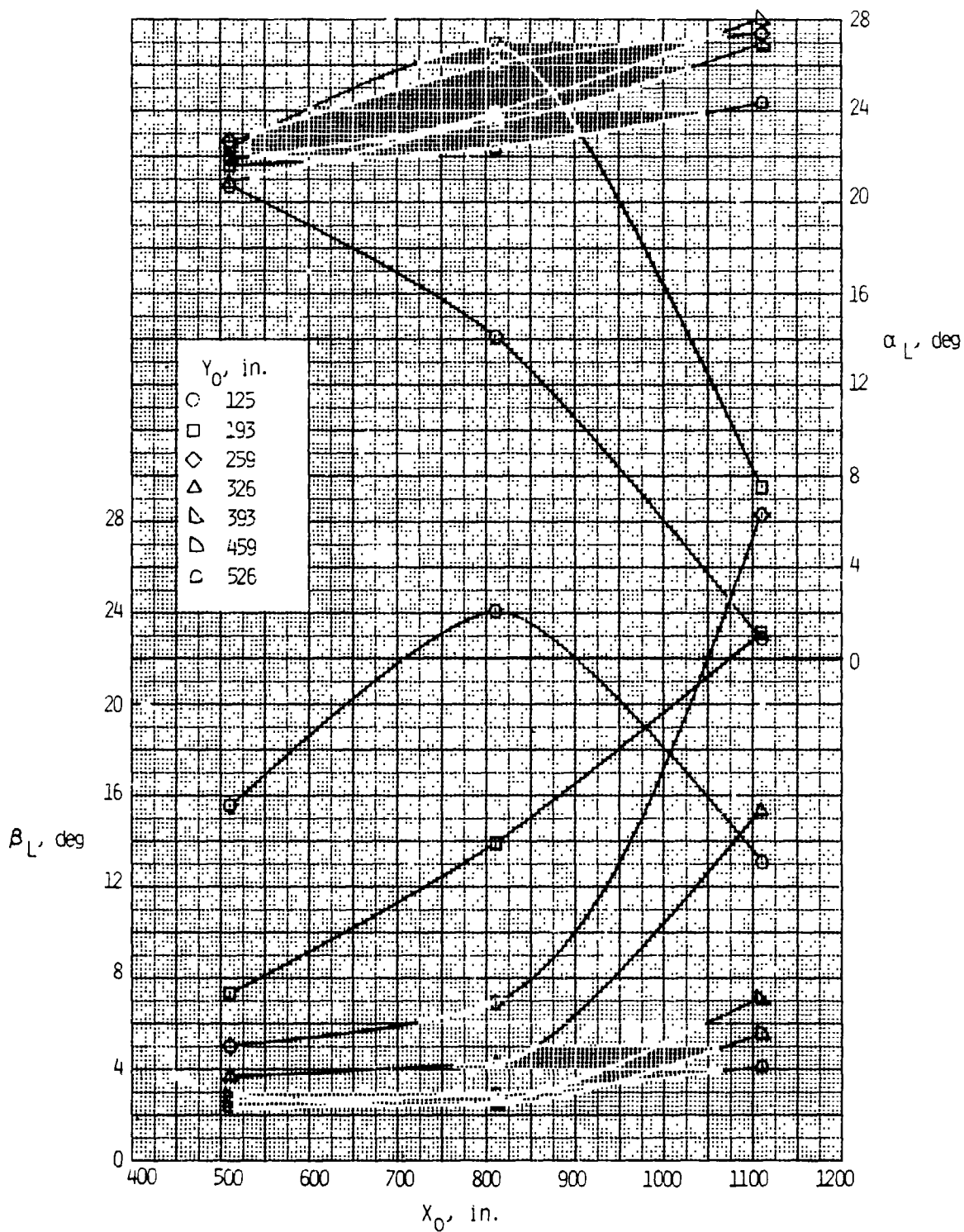
Figure 20. Concluded.

Velocity
Ratio, V_L/V_∞

$V_o - 63.2$ ft/sec

X_0, in.
○ 810
□ 1110

Velocity
Ratio, V_L/V_∞

$V_\infty = 159.0$ ft/sec

Y_0, in.
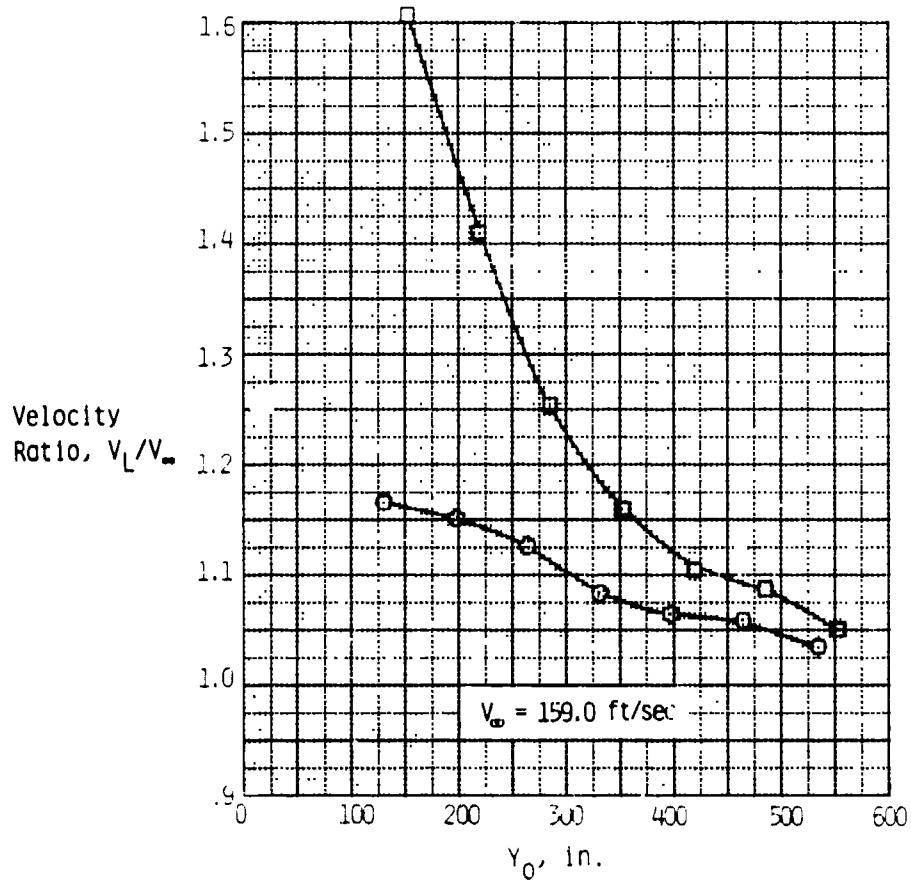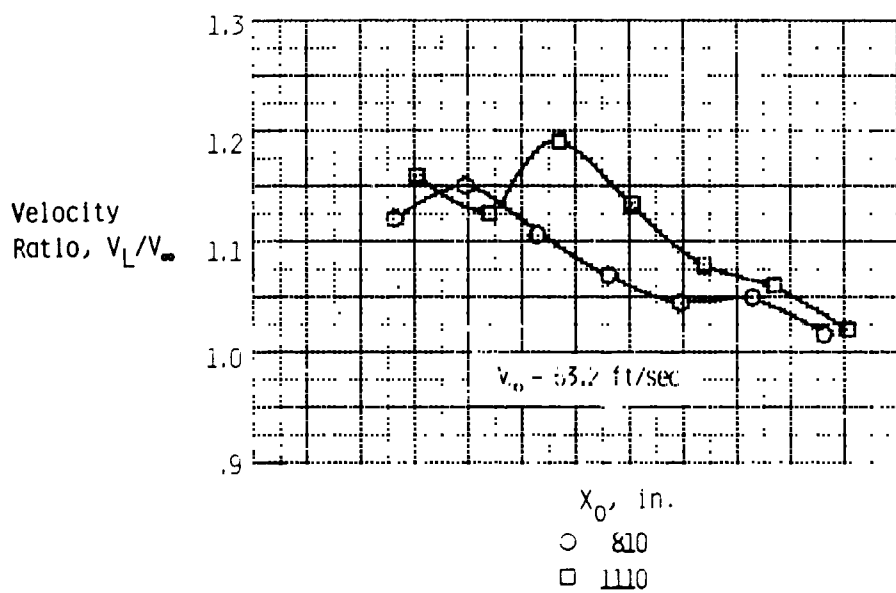
(a) Velocity ratio.

Figure 21. Spanwise variation of flow-field parameters at two longitudinal stations.
$Z_o = 433.0$ in.; $\alpha = 20°$; $\beta = 0°$.
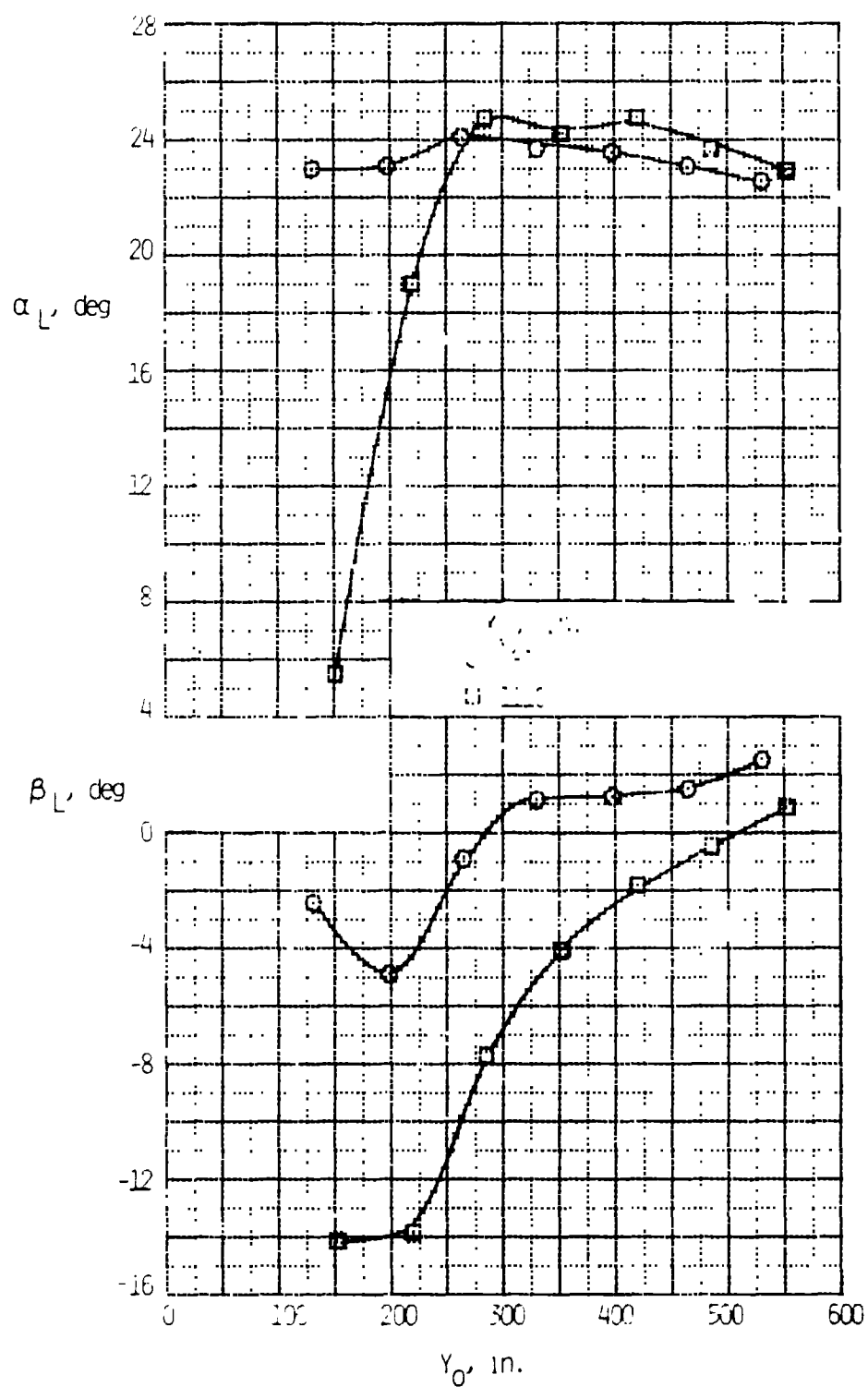
(b) Local angles of attack and sideslip, $V_\infty = 63.2$ ft/sec.
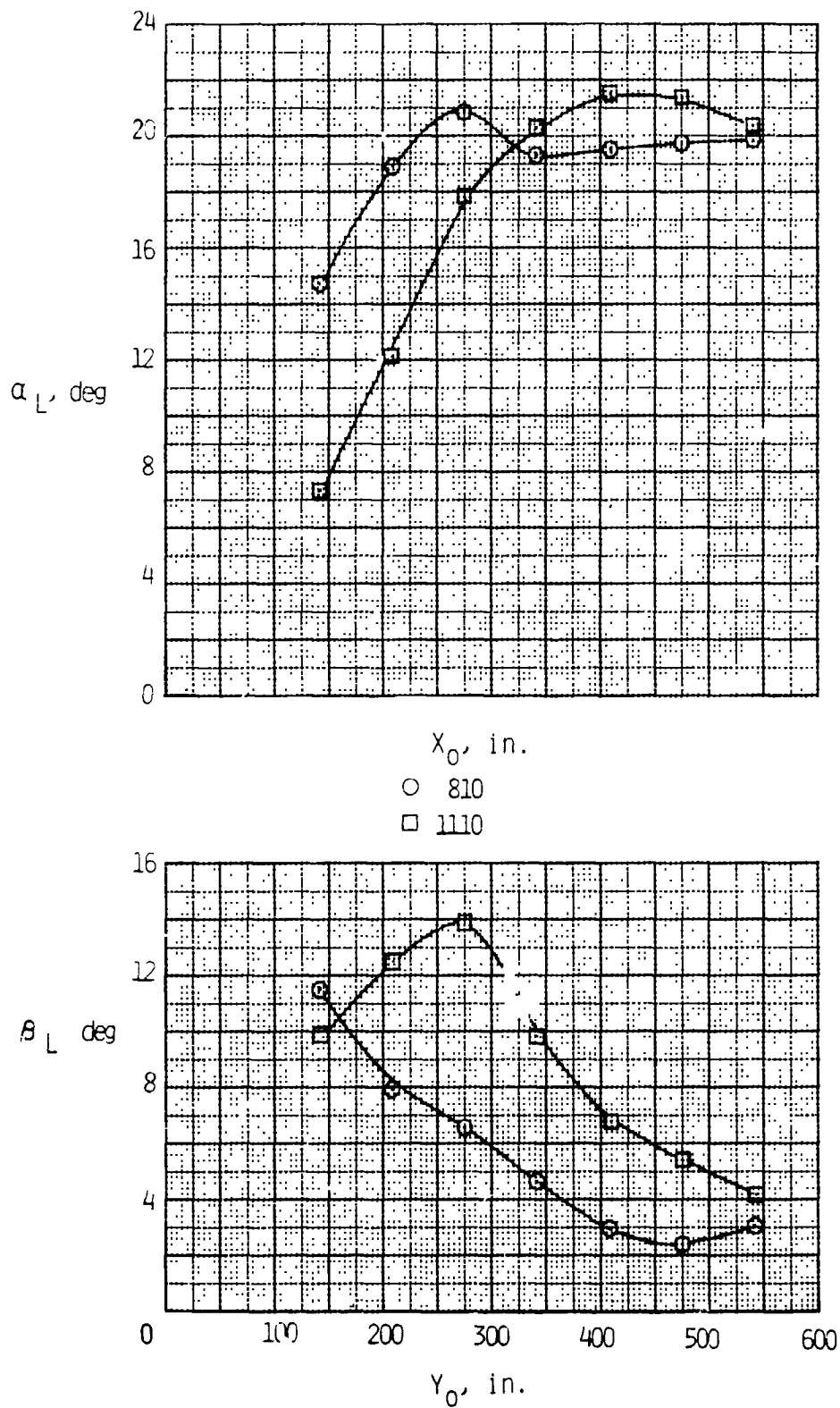
Figure 21. Continued.
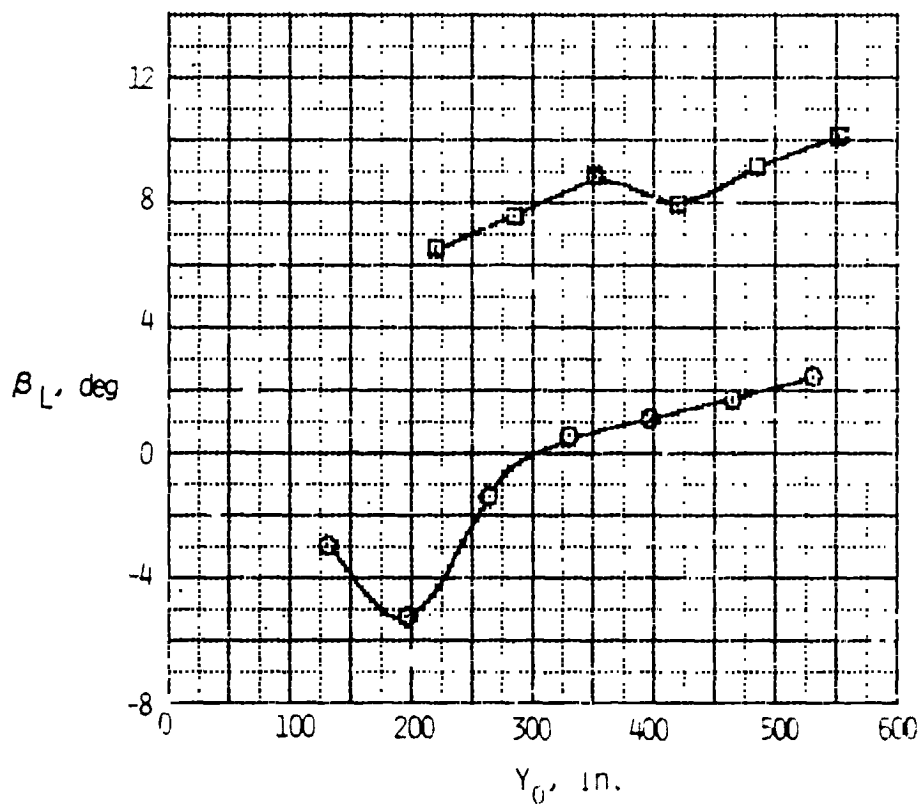
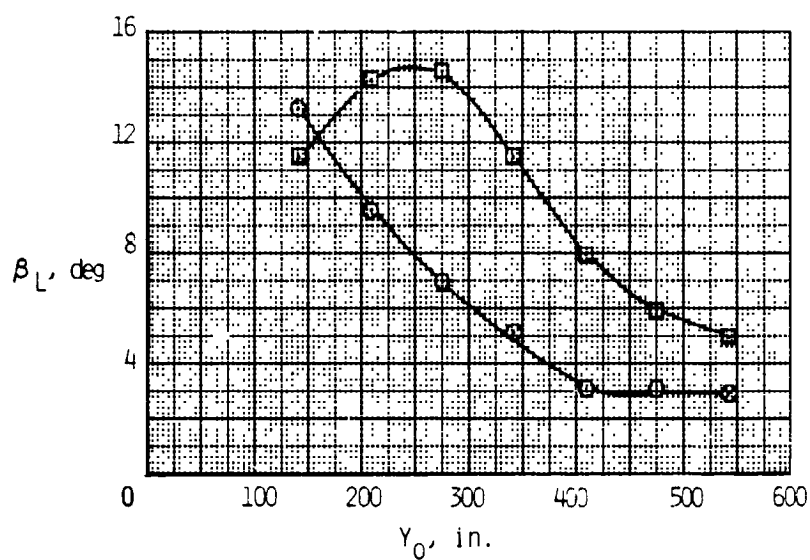(c) Local angles of attack and sideslip, $V_\infty = 159.0$ ft/sec.

Figure 21. Concluded.

(a) Velocity ratio.

Figure 22. Spanwise variation of flow-field parameters at two longitudinal stations. $Z_o = 433.0$ in.; $\alpha = 20°$; $\beta = 0°$.
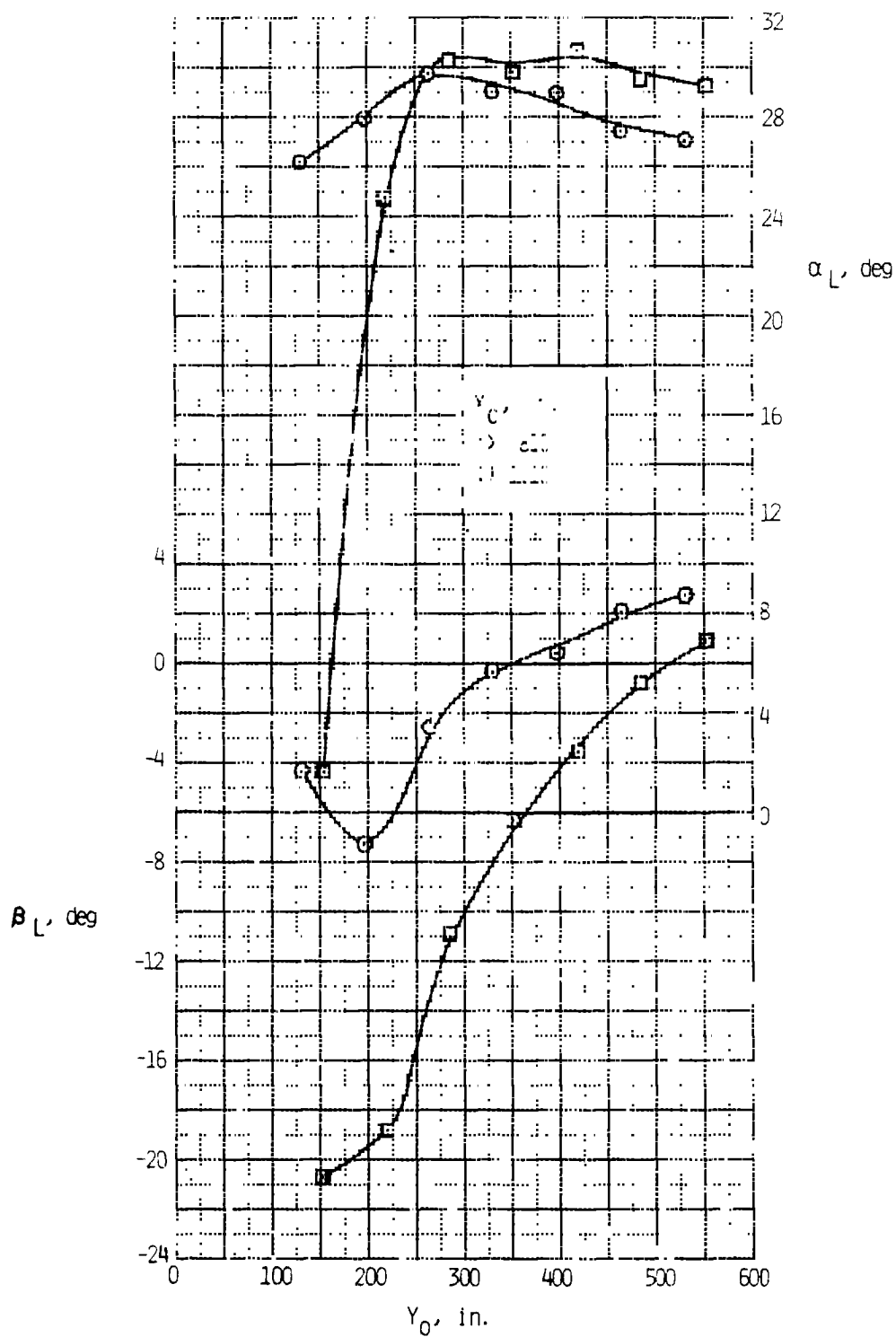
(b) Local angles of attack and sideslip, $V_\infty = 63.2$ ft/sec.

Figure 22. Continued.

(c) Local angles of attack and sideslip, $V_\infty = 159.0$ ft/sec.

Figure 22. Concluded.

(a) Velocity ratio.

Figure 23. Variation of flow-field parameters with longitudinal position at several spanwise stations. $Z_o = 247.0$ in.; $V_\infty = 62.4$ ft/s;c; $\beta = 0°$.

(b) Local angles of attack and sideslip, $\alpha = 17.5°$.

Figure 23. Continued.

(c) Local angles of attack and sideslip, $\alpha = 20°$.

Figure 23. Continued.
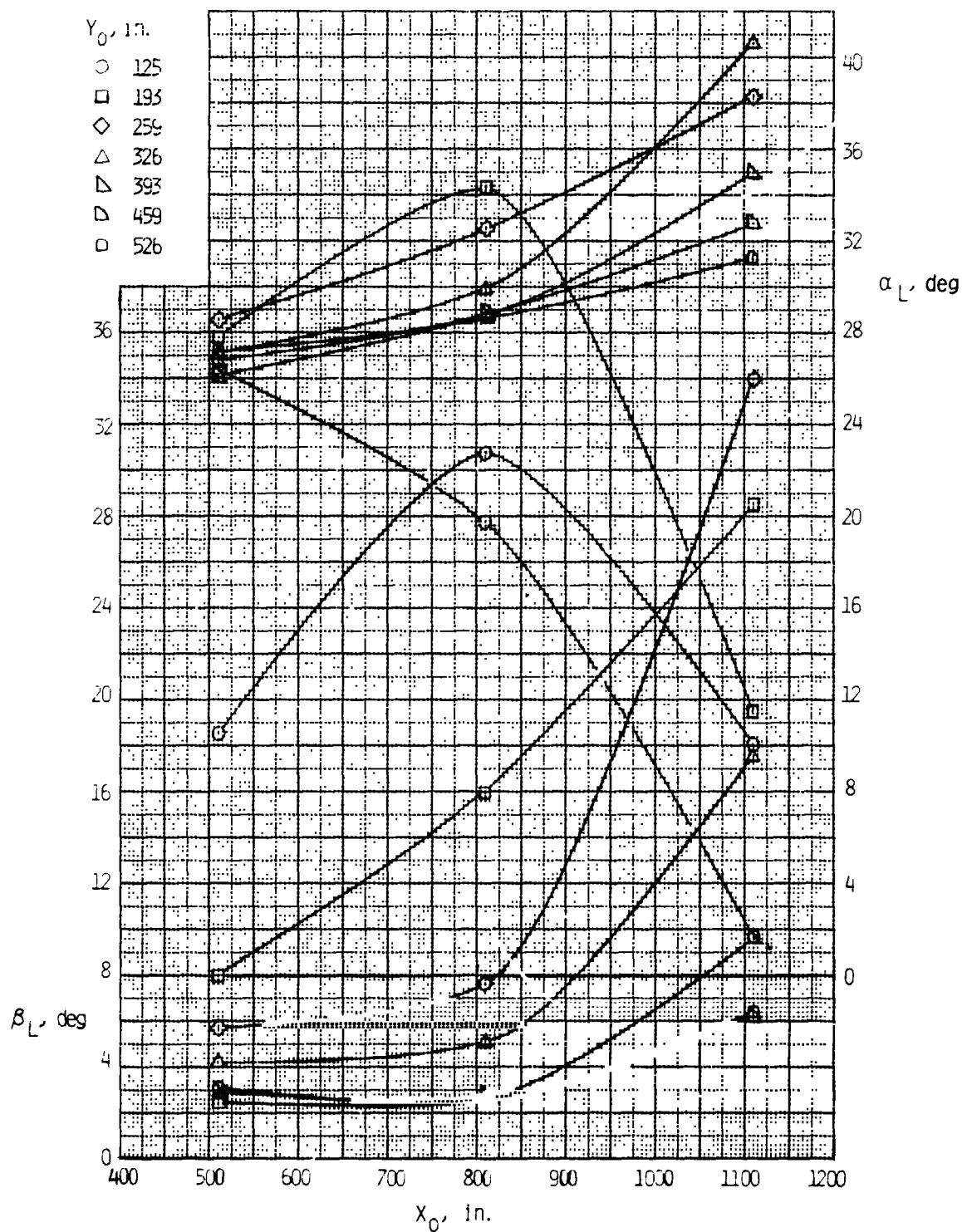
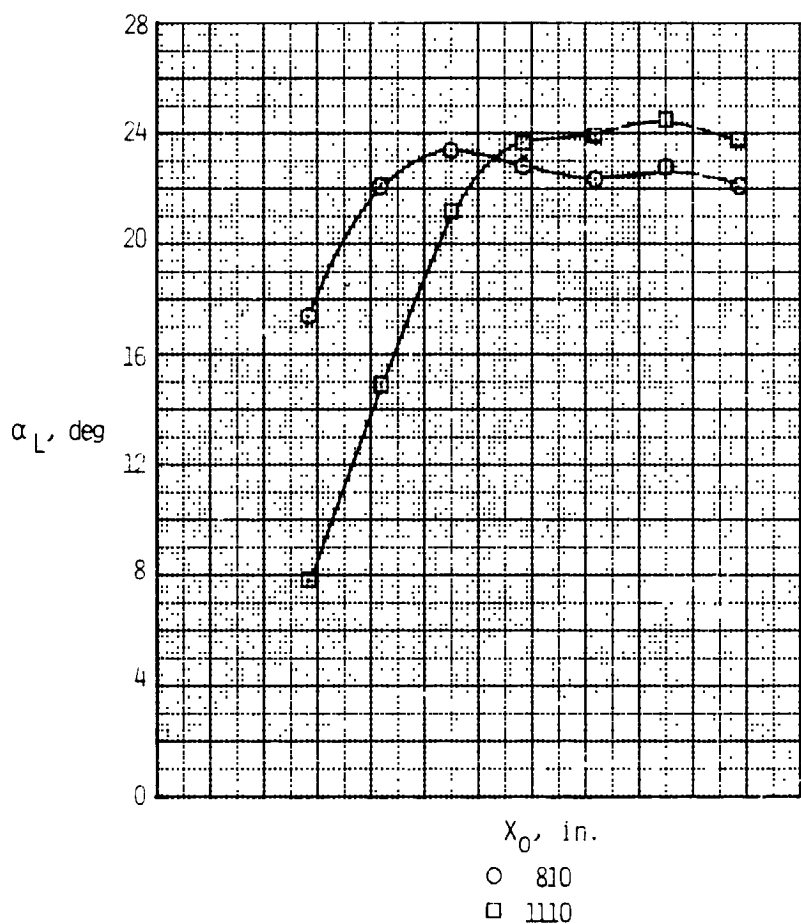(d) Local angles of attack and sideslip, $\alpha = 25°$.

Figure 23. Concluded.
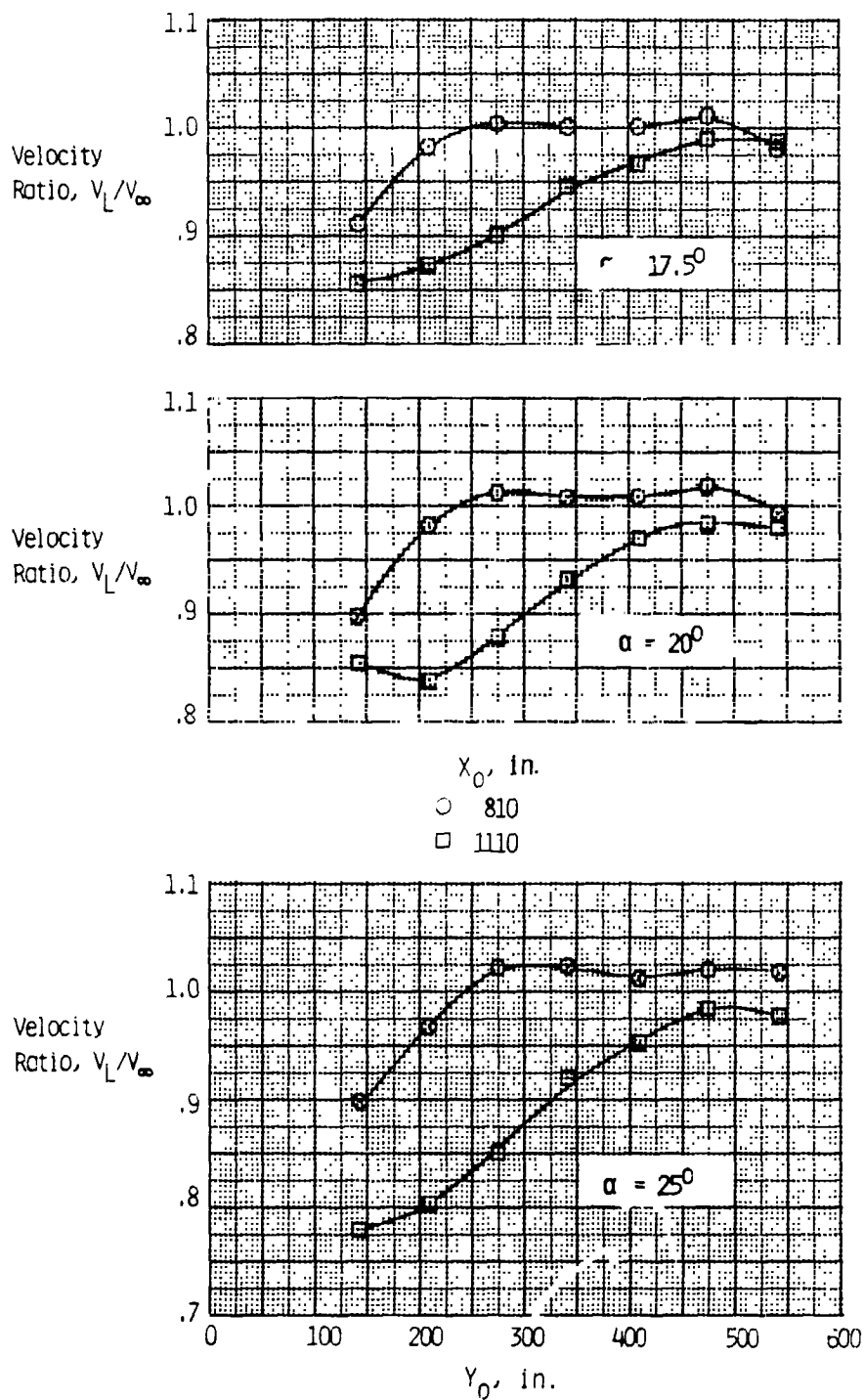
(a) Velocity ratio.

Figure 24. Spanwise variation of flow-field parameters at two longitudinal stations.
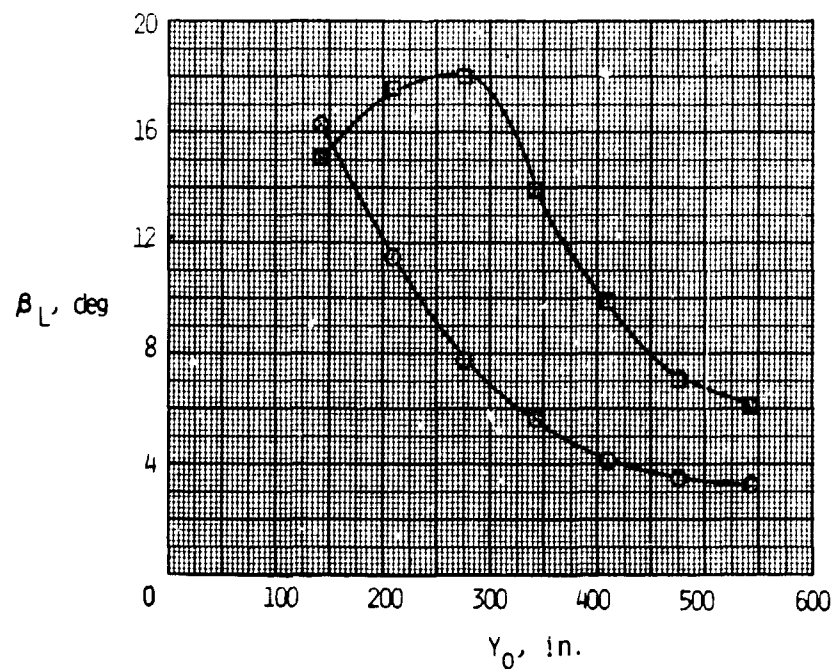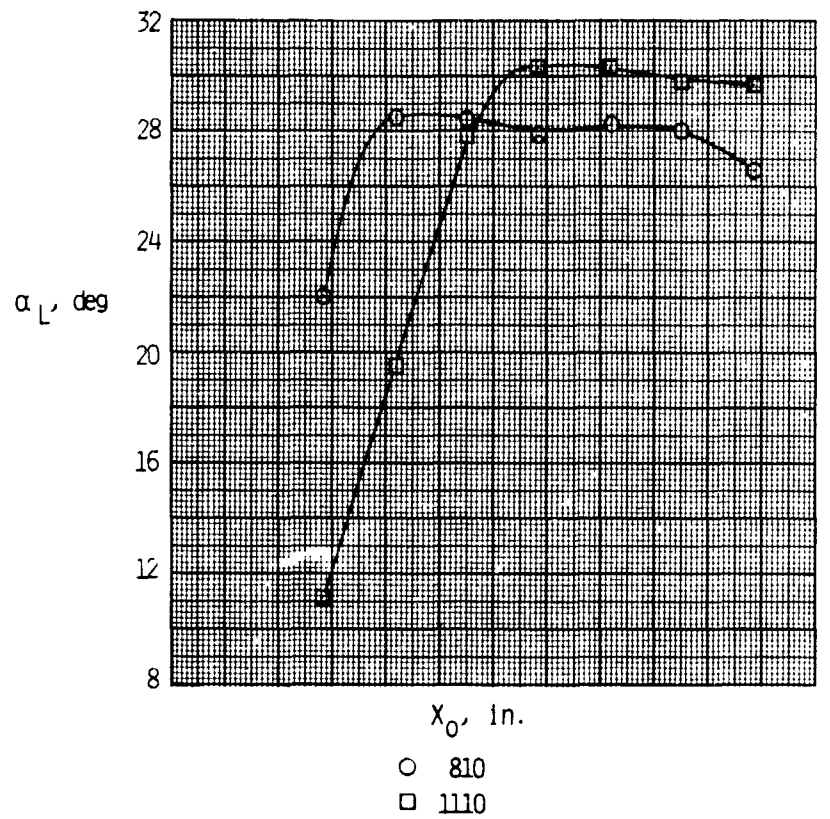$Z_o = 192.0$ in.; $V_\infty = 63.2$ ft/sec; $\beta = 0^\circ$.

(b) Local angles of attack and sideslip for $\alpha = 17.5°$.

Figure 24. Continued.

(c) Local angles of attack and sideslip for $\alpha = 20°$.

Figure 24. Continued.

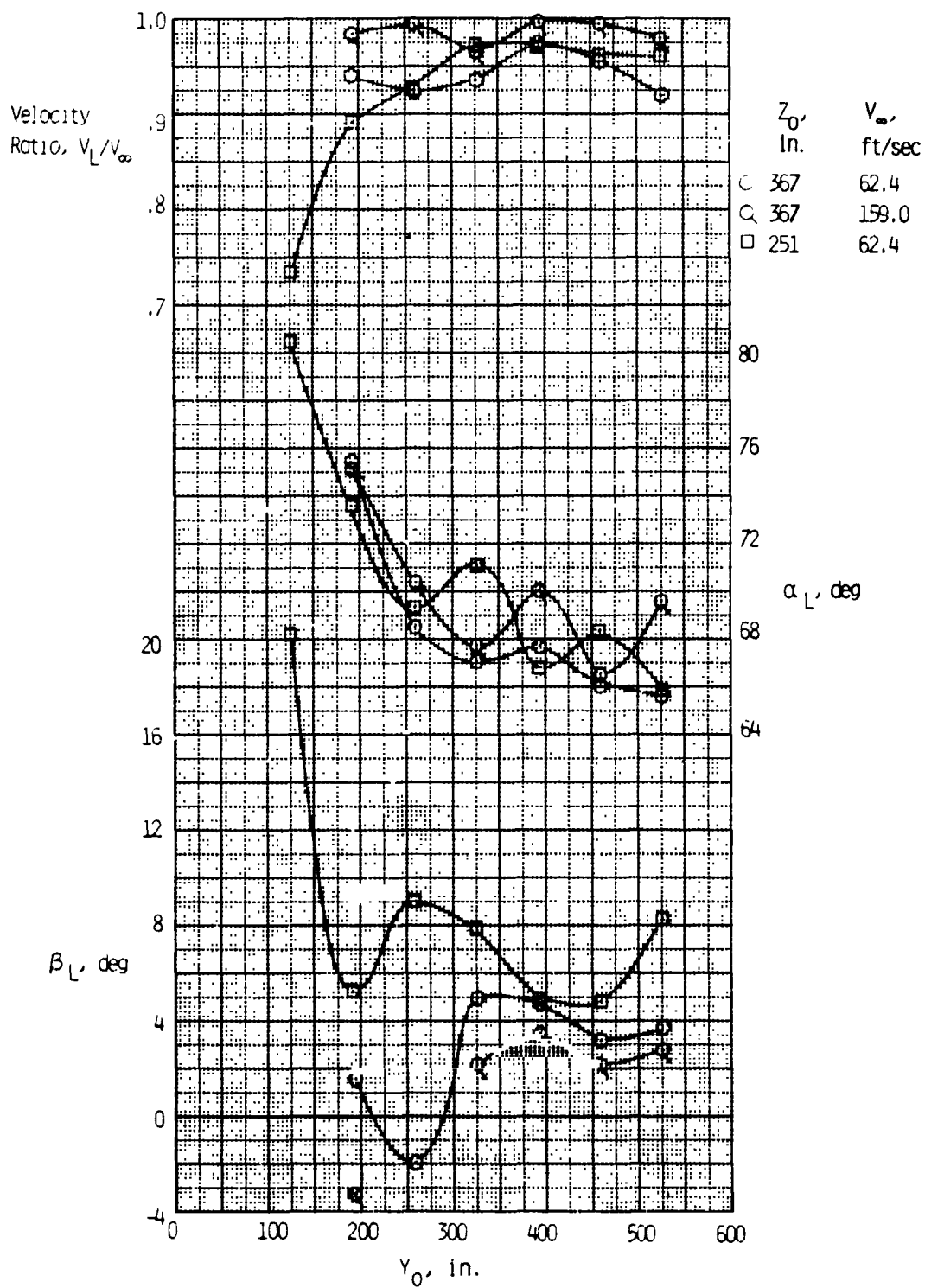(d) Local angles of attack and sideslip for $\alpha = 25°$.

Figure 24. Concluded.

Figure 25. Spanwise variation of flow-field parameters at two vertical stations. $X_o = 510.0$ in.; $\alpha = 65°$; $\beta = 0°$.